User Effects on Antennas in 5G Mobile Terminals

Syrytsin, Igor Aleksandrovich

Publication date:
2019

Document Version
Publisher's PDF, also known as Version of record

Link to publication from Aalborg University

Citation for published version (APA):
Syrytsin, I. A. (2019). *User Effects on Antennas in 5G Mobile Terminals*. Aalborg Universitetsforlag. Ph.d.-serien for Det Tekniske Fakultet for IT og Design, Aalborg Universitet

USER EFFECTS ON ANTENNAS IN 5G MOBILE TERMINALS

BY
IGOR SYRYTSIN

DISSERTATION SUBMITTED 2019

AALBORG UNIVERSITY
DENMARK

User Effects on Antennas in 5G Mobile Terminals

Ph.D. Dissertation

Igor Syrytsin

Dissertation submitted: August 29, 2019

Dissertation submitted: September 16, 2019

PhD supervisor: Prof. Gert Frølund Pedersen
Department of Electronic Systems
Aalborg University

Assistant PhD supervisor: Assoc. Prof. Shuai Zhang
Department of Electronic Systems
Aalborg University

PhD committee: Associate Professor Troels Bundgaard Sørensen (chair)
Aalborg University

Professor Raj Mittra
University of Central Florida

Professor Quan Xue
South China University of Technology

PhD Series: Technical Faculty of IT and Design, Aalborg University

Department: Department of Electronic Systems

ISSN (online): 2446-1628
ISBN (online): 978-87-7210-486-7

Published by:
Aalborg University Press
Langagervej 2
DK – 9220 Aalborg Ø
Phone: +45 99407140
aauf@forlag.aau.dk
forlag.aau.dk

Printed in Denmark by Rosendahls, 2019

Curriculum Vitae

Igor Aleksandrovich Syrytsin

Igor Syrytsin was born in Saratov, Russia, in 1988. He received B.S. degree in electronic engineering and information technology and M.S. degree in wireless communication systems from Aalborg University, Aalborg, Denmark, in 2014 and 2016, respectively, where he is currently pursuing the Ph.D. degree with the Department of Electronic systems. His current research interests include millimeter-wave mobile antenna design, array and beamforming network design and assessment of interactions between user and antennas in the mobile smartphones.

Curriculum Vitae

Abstract

The main focus of the thesis is to assess, characterize and model the user effects on the 5G mm-wave antennas in the mobile terminals. Furthermore, multiple novel 5G mm-wave antenna designs will be presented in this thesis as well. The proposed array designs are based on the totally novel, modified and commonly used antenna elements. However, the proposed antennas/array antennas, for the most part, have been designed for a specific investigation/measurement purpose. Thus, most of the antenna designs presented in this thesis are tailored towards the specific user effect assessment.

Multiple novel metrics have also been defined, which include shadowing antenna power ratio (SAPR), shadowing isotropic antenna power ratio (SIAPR), circularly polarized (CP) total scan pattern and CP coverage efficiency, shadowing CDF and 3D-SAPR. With the help of these novel metrics most of user effects on a 5G mm-wave mobile antenna/antenna array can be characterized.

A full-body homogeneous user phantom, based on the mean male human dimensions has been proposed, and has been used in the multiple investigation throughout the thesis. Based on the simulations with the phantom, the effects of the user on circular polarized phased antenna array are investigated. Furthermore, based on the different set of simulations with the phantom and multiple antennas, the best position for the phased 5G mm-wave antenna array on the mobile device is found. According to the guidelines given in this thesis a 5G mobile mm-wave antenna array system made from multiple sub-arrays distributed around the chassis can be made relatively immune to the user effects both in data and dual-hand modes.

Two big measurement campaigns including multiple users and multiple different antennas have been conducted in this thesis. The results from the measurement campaigns led to a stochastic spatial user shadowing model, which can be directly applied in the a link simulator as a 3D radiation pattern.

It has been also found that circularly polarized antennas are more robust to user effects than linearly polarized antennas and using a phased array is not always beneficial in order to obtain the best spatial coverage. Thus, a simple switch diversity array can be equally efficient in some cases.

Resumé

Denne Ph.D. afhandling har fokus på at vurdere, karakterisere og modellere brugereffekterne på 5G mm-bølge antenner i mobile terminaler. Endvidere, præsenteres der flere nye 5G mm-bølge antenne-designs i denne afhandling. De præsenterede array designs er baseret på nye, modificerede og ofte anvendte antenneelementer. Disse antenner er dog for det meste, blevet anvendt i de forskellige undersøgelser, der involverer personer. Ydermere er der også defineret flere nye udtryk og formler som kan bruges til at karakterisere effekter af brugeren. De forskellige nye udtryk er: skyggeantenneeffektforhold (SAPR), skygge isotropisk antenneeffektforhold (SIAPR), cirkulært polariseret (CP) totalt udstrålingsdiagram og CP-dækning effiktivitet, CDF i skyggen og 3D-SAPR. Med disse nye udtryk kan de fleste af brugereffekterne på 5G mm-bølge mobilantenner karakteriseres. Et homogent menneskefantom er foreslået, og er blevet brugt i de forskellige undersøgelser igennem afhandlingen. Baseret på simuleringerne med fantomet er brugerens effekt blevet undesøgt med et cirkulær polariseret antenne array. Baseret på flere antennesimuleringer med fantomet, den bedste position for 5G mm-bølge antenne array på den mobile enhed er presenteret. Baseret på forskningen givet i denne afhandling er det foreslået at et 5G mobilt mm-bølge antenne array system kan bestå af flere sub-arrays fordelt rundt om chassiset. På den måde er antenne arrayet mere immun over for brugereffekter både i data og dual-hand-tilstande. To store målekampagner med flere brugere og forskellige antenner er blevet gennemført i denne afhandling. Resultaterne af målekampagnerne førte til en stokastisk brugerskyggemodel, som kan anvendes direkte i en linksimulator. Der er også fundet, at cirkulært polariserede antenner er mere robuste over for brugereffekter end lineære polariserede antenner og et phased array ikke altid er det bedste valg for at opnå den bedste dækning. Således kan en simpel switch diversity array være lige så effektiv i nogle tilfælde.

Resumé

Contents

Thesis Details

Thesis Title:	User Effects on Antennas in 5G Mobile Terminals
PhD Candidate:	Igor Syrytsin
Supervisors:	Prof. Gert Frølund Pedersen - Aalborg University Assoc. Prof. Shuai Zhang - Aalborg University

This thesis is submitted as partial fulfillment of the requirements for the degree of Doctor of Philosophy (PhD) from Aalborg University, Denmark. The thesis is presented as a collection of papers resulting in the main part of the thesis being scientific papers published in, or submitted to, peer-reviewed journals. The work presented in the thesis is the result of three years of research, in the period August 2016 – August 2019, as a PhD fellow in the Antenna, propagation and mm-wave systems Section , Department of Electronic Systems, Aalborg University.

The PhD stipend has been funded as a part of the RANGE project for the first two and a half years of the Ph.d and the last half a year has been founded by the User shadowing project with HUAWEI Gothenberg. The Innovation Fund Denmark have together with Aalborg University and industry partners; WiSpry, Sony, and HUAWEI financed this project.

The main body of this thesis consist of the following papers:

- **A.** Igor Syrytsin, Shuai Zhang, Gert Frølund Pedersen, Kun Zhao, Thomas Bolin, and Zhinong Ying, " Statistical Investigation of the User Effects on Mobile Terminal Antennas for 5G Applications", *IEEE Transactions on Antennas and Propagation*, 2017
- **B.** Igor Syrytsin, Shuai Zhang, Gert Frølund Pedersen, Zhinong Ying, "User Effects on the Circular Polarization of 5G Mobile Terminal Antennas", *IEEE Transactions on Antennas and Propagation*, 2018
- **C.** Igor Syrytsin, Shuai Zhang, Gert Frølund Pedersen, "User Impact on Phased and Switch Diversity Arrays in 5G Mobile Terminals", *IEEE Access*, 2018

D. Igor Syrytsin, Shuai Zhang, Gert Frølund Pedersen, and and Art Morris, "Compact Quad-Mode Planar Phased Array with Wideband for 5G Mobile Terminals", *IEEE Transactions on Antennas and Propagation*, 2018

E. Igor Syrytsin, Shuai Zhang, Gert Frølund Pedersen, and and Art Morris, "User Shadowing Suppression for 5G mm-wave Mobile Terminal Antennas", *IEEE Transactions on Antennas and Propagation*, 2019

F. Peiye Liu, Igor Syrytsin, Shuai Zhang, Jesper Ødum Nielsen, and Gert Frølund Pedersen, "Characterization and Modeling of the User Blockage for 5G", *IEEE Transactions on Antennas and Propagation*, 2019,
SUBMITTED 2019

According to the Ministerial Order no. 1039 of August 27, 2013, regarding the PhD Degree § 12, article 4, statements from each co-author about the PhD students contribution to the above-listed papers have been provided to the PhD school for approval prior to the submission of this thesis. These co-author statements have also been presented to the PhD committee and included as a part of their assessment.

In addition to the listed papers as the main content of this thesis, the following papers were also either authored or co-authored during the PhD studies. As these papers are not a part of the main body of this thesis they have not been included in print. The reader is therefore kindly referred to their respective publishing channels as listed hereafter.

Journal Articles

1. Compact Beam-Steerable Antenna Array with Two Passive Parasitic Elements for 5G Mobile Terminals at 28 GHz; Zhang S., Syrytsin I. A. & Pedersen G. F., okt. 2018, IEEE Transactions on Antennas and Propagation. 66, 10, pp. 5193-5203.
2. A Planar Switchable 3-D-Coverage Phased Array Antenna and Its User Effects for 28-GHz Mobile Terminal Applications; Zhang, S., Chen, X., Syrytsin, I. A. & Pedersen, G. F., dec. 2017, IEEE Transactions on Antennas and Propagation. 65, 12, pp. 6413 - 6421.

Conference Articles

1. Antenna Integrated with a Microstrip Filter for 5G Mm-wave Applications; Syrytsin I., Shen, M. & Pedersen G. F., 1 nov. 2018, Proceedings of the 2018 20th International Conference on Electromagnetics in Advanced Applications, ICEAA 2018. IEEE, pp. 438-441.

2. Dual-polarized Dual-band Mobile 5G Antenna Array; Syrytsin I. A., Zhang S. & Pedersen G. F., 2018, Proceedings of the 15th International Joint Conference on e-Business and Telecommunications (ICETE 2018),Bind 2. pp. 309-315.
3. Effects of Phone Case and User Effects on Switched-Beam High Gain Antenna System for 5G Mobile Terminals; Syrytsin, I., Zhang, S. & Pedersen, G. F., 1 nov. 2018, Proceedings of the 2018 20th International Conference on Electromagnetics in Advanced Applications, ICEAA 2018, pp. 110-113.
4. Finger Ring Phased Antenna Array for 5G IoT and Sensor Networks at 28 GHz; Syrytsin, I. A., Zhang, S. & Pedersen, G. F., 10 dec. 2018, 12th European Conference on Antenna and Propagation (EuCAP).
5. Investigation of User Effects on Mobile Phased Antenna Array from 5 to 6 GHz; Di Paola, C., Syrytsin, I. A., Zhang, S. & Pedersen, G. F., 10 dec. 2018, 2018 IEEE 12th European Conference on Antenna and Propagation (EuCAP).
6. Measurements of UWB Pulse Propagation Along a Wind Turbine Blade at 1 to 20 GHz; Hejselbæk, J., Syrytsin, I. A. & Eggers, P. C. F., 2018, 12th European Conference on Antennas and Propagation (EuCAP).
7. Pattern-Reconfigurable Mobile Terminal Antenna System for MIMO and Link Stabilization in LTE; Syrytsin, I. A., Vestager, H. A., Nørgaard, S. B., Thomsen, L., Barrio, S. C. D. & Pedersen, G. F., 10 dec. 2018, 12th European Conference on Antennas and Propagation (EuCAP 2018).
8. Substrate-Insensitive Phased Array with Improved Circularly-Polarized Scan Angle for 5G Mobile Terminals; Zhang, S., Syrytsin, I. A. & Pedersen, G. F., 10 dec. 2018, 12th European Conference on Antenna and Propagation (EUCAP 2018).
9. Antenna Array Construction on a Mobile Terminal Chassis at 3.5 GHz for LTE Advanced; Syrytsin, I. A., Zhang, S. & Pedersen, G. F., 2017, 2017 11th European Conference on Antennas and Propagation (EUCAP). IEEE, s. 2695 - 2699 (European Conference on Antenna and Propagation (EUCAP)).
10. Circularly Polarized Planar Helix Phased Antenna Array for 5G Mobile Terminals; Syrytsin, I. A., Zhang, S. & Pedersen, G. F., 2017, 2017 International Conference on Electromagnetics in Advanced Applications (ICEAA). IEEE, pp. 1105-1108.
11. Extremely Low-Profile Circular Patch-Ring Antenna with A Shorting Via for Impedance Matching Improvement; Zhang, S., Syrytsin, I. A., Sørensen, M. & Pedersen, G. F., 2017, 2017 IEEE-APS Topical Conference on Antennas and Propagation in Wireless Communications (APWC). IEEE, pp. 221 - 224.

12. Switchable Phased Antenna Array with Passive Elements for 5G Mobile Terminals; Syrytsin, I. A., Zhang, S. & Pedersen, G. F., 2017, Proceedings of the 14th International Joint Conference on e-Business and Telecommunications (ICETE 2017). SCITEPRESS Digital Library, pp. 62-66.
13. Wideband Butler Matrix for 5G Mm-wave Antenna Application; Syrytsin, I. A., Zhang, S. & Pedersen, G. F., 2019, submitted to 2020 11th European Conference on Antennas and Propagation (EUCAP).

Patents

1. User Insensitive Phased Antenna Array Devices, Systems, And Methods.
2. Wideband Phased Mobile Antenna Array Devices, Systems, And Methods.
3. Compact Beam-Steerable Antenna Array Without Phase Shifter for Centimeter-wave and Millimeter-wave Mobile Terminals.

Preface

This thesis is submitted as a partial fulfillment of the requirements for the degree of Doctor of Philosophy at Aalborg University, Denmark. The main body of the thesis is a collection of papers published or submitted to the relevant peer reviewed journals in the field of antennas and propagation. This thesis is a result of three years of research in Antennas, Propagation and Millimetre-wave Systems (APMS) section, Department of electronic systems, Aalborg University, in period from August 2016 to August 2019.

This thesis has been prepared under the genral supervision of Prof. Gert Frølund who has proposed this project. The work in this thesis was mainly supported by Danish Innovation Foundation and Reconfigurable Arrays for Next Generation Efficiency (RANGE) research project.

The specific supervision of the Ph.D. student has been done by Assoc. Prof. Shuai Zhang, who I am very thankful for the navigation through the challenges of academia and publishing. With his guidance I have been grown from the student to the independent researcher with ability to detect the relevant problem in the specific scientific niche, then find the tools and the knowledge to solve that problem, and finally present a solution to that problem in the written form to others in the relevant academic field. Furthermore, i want to thank Art. Morris from WiSpry, Ying Zhinong and Thomas Bolin from Sony for the feedback on my research from the point of view of the industry. I would also like to thank Wei Hong from National Key Laboratory of MM-waves, Nanjing, China, for generous help and collaboration during my external stay in your group.

Igor Syrytsin
Aalborg University, August 15, 2019

Part I

Introductory Chapters

Introduction

Already in 2017, it has been predicted that the internet traffic will nearly quadruple in 2022 as seen in Fig. 1.1. This traffic is composed of the data produced by HD camera, IP videos, UHD cameras, UHD streaming, VR, UHD IP Video, 8K wall TV, HD VR, and UHD VR. It has been predicted that in the fiture UHD and VR services will take the most internet traffic load. However, nowadays modern smartphones already include some of the features which will be expanded upon in the upcoming years in order to get the higher throughput.

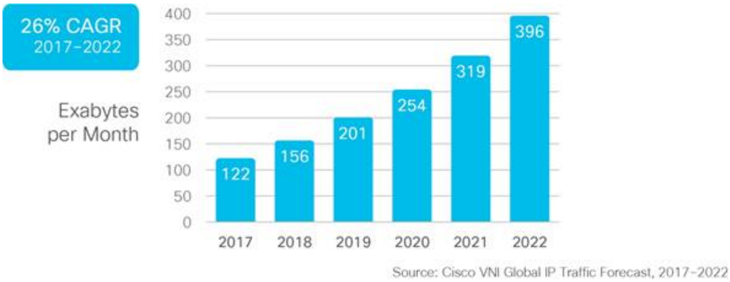

Fig. 1.1. Expected global traffic in Exabytes from 2017 to 2022.

Moreover, in order to accommodate more wireless internet traffic, in addition to the already existing WiFi and 4G LTE systems, radically different solutions are needed. As it is now, the data rate of the existing wireless systems is not high enough for the UHD streaming and VR services. To get better understanding of the problem we take a look on the channel capacity which describes the upper bound at which the information can be transmitted:

$$C = B \cdot \log_2 \left(1 + \frac{S}{N}\right) \tag{1.1}$$

where:

- B is a radio channel bandwidth.
- S is a signal power.
- N is a noise power.

From this formula it can clearly be seen that the increase in capacity can be affected by a few factors :

1. Increasing the base station transmit power. This will consume more energy and lead to the more expensive RF front-end. Furthermore, this will also create more interference to the co-channel cells and increase the overall SINR.
2. Increase the bandwidth of the channel “B”. This will also make multiple components of the system more complex and expensive as the overall efficiency will usually drop when hardware is needed to perform well along the wide frequency range.
3. Reduce the noise in the system, where the power of the noise will depend on the quality of the RF front-end and co-channel cell interference strength.

However, there is very little free/unlicensed spectrum below 6 GHz, which not already occupied by LTE, GSM, WIFI or Satellite services as seen in Fig. 1.2. This is why it has been chosen by 3GPP community to move to the frequencies higher than 20 GHz. This focus shift has also been heavily discussed in the scientific community [1]. Currently frequency bands around 28 and 38 GHz has already been allocated in the multiple countries [2].

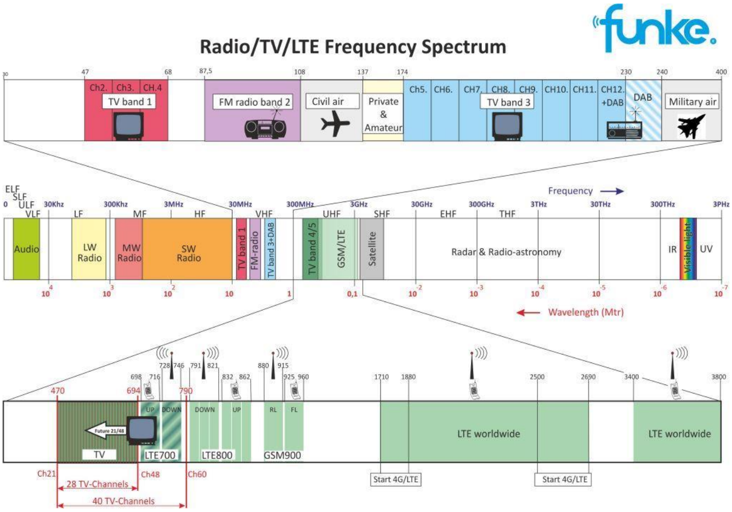

Fig. 1.2. Typical spectrum allocation.

A common misconception in the wireless communication community is that a free space path loss becomes larger as the frequency increases. However, this statement is only partially true. Let’s take a closer look on the Friis’ equation:

$$P_r = P_t \left(\frac{A_r A_t}{d^2 \lambda^2} \right) \tag{1.2}$$

where:

- P_r Rx power in [W].
- P_t Tx Power in [W].
- d is a distance between antennas in [m].
- λ is a wavelength in [m].
- $A_r = \frac{G_r \lambda^2}{4\pi}$ Aperture of the Rx antenna in [m], G_r is a gain of Rx antenna in dBi.
- $A_t = \frac{G_t \lambda^2}{4\pi}$ Aperture of the Tx antenna in [m], G_t is a gain of Tx antenna in dBi.

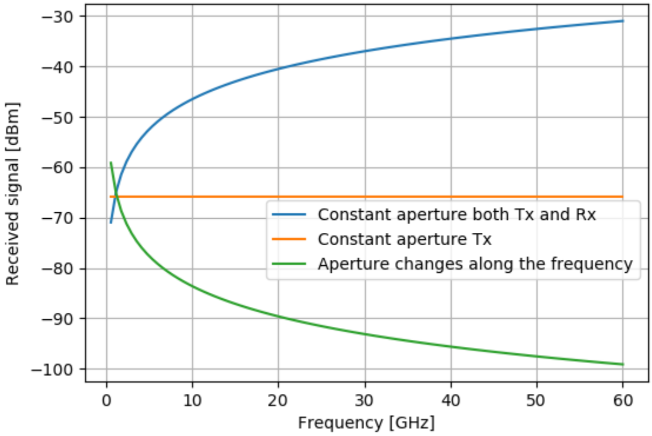

Fig. 1.3. Received signal power strength calculated based on the Friis equation for different frequencies.

If we look carefully in Fig. 1.3 then it can be noticed that usually according to a Friis equation, the received power is perceived as a decaying function of frequency (denoted by a green line). But this is only the case when the antenna aperture is also becoming smaller with the frequency. Typically, this can be explained by the fact that in order to conserve space the antenna structure is made for the specific application. This will usually lead too more narrow bandwidth and lower realized gain of the antenna. However, if the Rx or Tx antenna aperture is kept constant then the received power do not depends on the communication frequency in Fig. 1.3 and orange curve. Often, the antenna aperture can be kept constant if more antenna elements are placed on the same physical space when the frequency increase. Nonetheless, arraying of the antenna elements will reduce the aperture efficiency as some minimum distance between elements is always required for the optimum array operation. Finally, if both Tx and Rx antennas have a constant aperture along the frequency range then the received power will actually increase with the frequency because the antennas with bigger aperture will have a higher gain.

Antennas with big aperture and high gain typically have one or more narrow main beams, but in the highly dynamic mobile environments the antenna with the omni-directional aperture is usually desired for capturing most of the available multipath components. This omni-directional coverage challenge could be solved by changing the main beam direction dynamically according to user mobility patterns, mobile position and the location of the scatterers. The most simple way to achieve beemforming is to mechanically steer the beam, however this solution is not applicable for implementation in the compact mobile devices of the 21 century. Thus, multiple different beamforming antenna solutions [3] can be proposed for the 5G mm-wave mobile devices in Fig. 1.4. Each of the technologies have benefits and drawbacks and often, the antenna designer would deal with the trade-offs between simple design, size, main beam accuracy and system complexity.

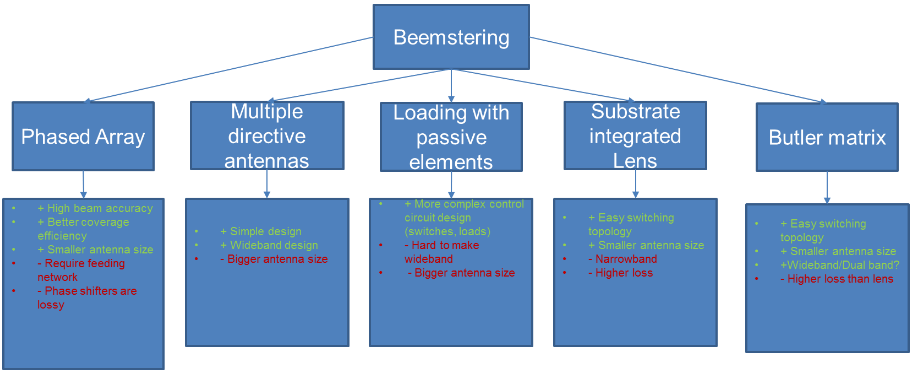

Fig. 1.4. Types of beemseering technologies applicable for 5G mobile devices.

As the base station have dual polarized antennas – the mobile terminal also need to have two polarizations with low beam correlation. Multi-polarized antenna array design for mm-Wave 5G mobile terminals is proposed in [4]. Because the clearance for the mobile antenna in the already crowded device is very small it is very important to make the antenna elements compact, as shown in [5] where a Vivaldi phased antenna array has been studied with the user. In [6] where a compact dipole-like quad mode element is applied, which is discussed in the detail in Paper D. A low-profile phased antenna array with a mesh-grid patch antenna element has been designed and analyzed in [7]. Furthermore in order to integrate the 5G mm-wave antenna with the low frequency LTE and GSM antenna a compact 4G MIMO antenna integrated with a 5G array has been designed in [8] as the 5G smartphones should be backwards compatible with the older mobile communication systems.

To increase the coverage of the phased mobile antenna array, two different methods have been introduced in [9] and [10]. In [9] the 3D coverage has been realized by switching between 3 sub-arrays mounted on a folded 3D structure. On the other hand, in [10] the 3D coverage has been achieved by using a surface wave in order to change radiation pattern main beam directions of the three planar sub-arrays. However, the bandwidth of the shown antennas is not so wide enough in order to achieve high data rates of 5G system. Furthermore, the exact operating frequency and bandwidth of the 5G communication system is still unknown but it is speculated that around 3 to 5 GHz is to be expected. The phased mobile antenna array with wide scan angle has been proposed in [11]. However, the antenna does not have wide enough bandwidth to accommodate both lower and higher 5G bands at the same time. The bow-tie phased antenna array in [12] has a wide bandwidth and wide scan angle. Yet, designs in [11] and [12] require at least 6 mm clearance and only simulation results have been presented. The feeding network and connectors have not been implemented in these designs. lately it has been shown that it is very very advantageous to put LTE antennas on the frame around the mobile device which can reduce the envelope correlation coefficient [13] and even user body/hand effects in [14] and [15]. However, the effects of the metal phone case and the frame on the shape of the radiation pattern are significant as it has been shown in [16] and [17]. But, by applying two tilted layers of coupled metal strips close to the frame the blockage can be significantly reduced in [18].

To verify the performance of such beamforming mobile antennas the arbitrary user equipment orientation should be considered. Thus a new metric of the coverage efficiency has been proposed in [19] and applied in [20] to the practical mobile terminal phased arrays. The coverage efficiency describe the actual spatial coverage of the beamforming antenna array for all possible beam perturbations and defined as [20]:

$$\eta_c = \frac{\text{Coverage Solid Angle}}{\text{Maximum Solid Angle}} \tag{1.3}$$

where maximum solid angle defined as 4π steradians (full sphere).

In the perfect world the beamforming antenna with high gain in all possible directions would be the best solution. However, in the real mobile device the space allocated for the 5G antenna is limited and the complexity of the 5G antenna is also directly proportional to the cost of the beamformer. Two cheap ways to increase the coverage of the 5G antenna array are proposed in [9] and [10]. In [9] the 3D coverage has been realized by switching between 3 folded sub-arrays mounted on the edge of the ground plane. Then, in [10] the 3D coverage is realized by using a surface wave as and advantage to change the main beam directions by applying a different offset between the edge and an array element.

The bandwidth of the shown antennas is not so big and the wider bandwidth (wideband or dual-band) is wanted in order to achieve higher data rates in multiple bands. Multiple phased array designs has been proposed in [11] and [12] and furthermore discussed in Paper D. However, in application the exactly similar beamforming performance along the frequency is difficult to achieve for the phased arrays. Furthermore, analog wideband phase shifters will be very expensive and will have mediocre performance for the extremely wide bandwidth (high insertion loss). However, RF switches are more reliable and can be made wideband, cheap, and with lower insertion loss then the phase shifters. To exploit this advantage, multiple alternatives to the phased array solution has been proposed. The simplest solution is to place multiple high gain antennas around the device and point them in the different directions [21]. However, drawback of this approach is that the antenna aperture will increase with the antenna gain and thus it is very difficult to make high gain antennas very compact. So maximum gain of 7 to 8 dBi is expected from this approach. Furthermore, by coupling the driven element to the passive elements, the radiation pattern of the antenna can be altered without consuming extra space on the PCB [10], but number of main beam directions will be limited by the number of passive elements and impedance loads. Finally a planar lens based on SIW technology can be applied as shown in [22] and when combined with the H-plane horn [23] can be made more compact as shown in Paper E.

The user effects are also a very important factor when designing an antenna for the mobile terminal [24]. The user can be concidured as a part of the antenna in some cases but in other cases the user can be called a part of the propagation channel. At the frequencies lower than 6 GHz the body loss, which comes from the absorption of the energy inside the human tissue is a very big factor and has been thoroughly studied in [25], [26], and [27]. Furthermore the missmatch loss of the antenna will be the second biggest part of the body loss at sub-6 GHz frequencies. As shown in [28] the antenna will be loaded by the tissue when close to the human body and a resonant frequency of the antenna will be moved down or up. Finally, a user will affect the radiation pattern by blocking part of the power. Even at sub-6 GHz this effect is significant and has been evaluated using mean effective gain (MEG) measure in [29] and [30] and a radiation pattern in [31] and [32]. Also the hands and the position of the fingers will affect the performance of the mobile device considerably as is has been shown in [33] and [34].

With the higher frequency the user effects will actually change and main loss will actually come from the user blockage as discussed in Paper A. Early studies shown extremely high blockage at 60 GHz in [35] but at 5G bands (under 40 GHz) the blockage is smaller but still significant. The currents around the antenna elements are highly localized and thus a resonant frequency is not significantly affected by the user's fingers and hand. 3GPP community has already proposed some simple models of the user blockage [36], where the user is represented as a square block with attenuation of -30 dB. To characterize the user blockage, multiple metrics such as coverage efficiency loss and shadowing power ratio (SAPR) [37] can be applied. Coverage efficiency losses at 15 GHz are already significant which have been assessed with a realistic phased array in [38]. The performance of switch diversity and phased arrays with the user has been investigated in Paper C, which shown that it is not always advantageous to use a phased array. User effects on the switch beam antennas with gain of $G_{max} \geq 7$ dBi are shown to be considerable in [39]. It has also been shown that some user effects can be mitigated by using antenna array diversity in in Paper D. Finally, in [40] the user blockage is measured with the phased array in the indoor environment, but in this case only power has been measured and no spatial distribution been shown.

Aims

This Ph.D thesis presents several 5G antenna design as well as user impact evaluation in different scenarios. It is well known that when designing an antenna for the mobile handheld devices then the user will be an integral part of the environment. In this thesis, multiple different 5G mm-wave antenna designs are presented and then simulated and measured with the user. Furthermore, multiple novel metrics are defined in order to quantify user effects on mobile terminal phased,switched and multi-beam antennas and arrays at 20 to 40 GHz frequency range. The aims of the thesis can be divided into following groups of study subjects:

Investigation of body and coverage efficiency losses and user blockage. When designing a communication systems the reliable link simulations are usually performed before the system implementation. User effects such as body loss, user blockage and coverage efficiency losses are very important parameters to include in the link simulations or ray-tracing programs. Furthermore, the spatial performance of the antennas is also an extremely important factor to take into account when designing a 5G mm-wave systems. User will induce a blockage in one part of the space and also numerous reflections in the other part of the space. This will result in the change in the coverage efficiency distribution. Moreover, beam-steering will also be an integral part of the 5G mm-wave system. Therefore it is important to test the antenna element or a switched or phased arrays performance with single or multiple users. Multiple user measurement is important in order to achieve mean values of the chosen metrics.

Design a circularly polarized 5G mm-wave antenna and assess the user effects on the axial ratio and coverage efficiency. A circularly polarized antenna has multiple advantages when the orientation of the either receiver or transmitter is unknown and an exact polarization matching is difficult to achieve. Base station usually can transmit in two orthogonal linear polarizations and by making the mobile antenna circularly polarized, a 3 dB loss will be induced in the worst case. However, if the mobile antenna is linearly polarized then a loss can exceed tenth of dBs if missmatched with the base station polarization. Furthermore, designing a compact circularly polarized antennas with a simple feeding structure is quite difficult which is one of the aims of this study. Another issue with the circularly polarized antenna arises when the circurlarly polarized element is operating in a phased array. A wide beam with low axial ratio is desired from a such antenna element. When scanning the beam, is is very difficult to guarantee a perfect circular polarization for every scan angle. Furthermore, multiple novel metrics are needed to characterize circurlarly polarized antennas performance in 5G mm-wave mobile terminals.

Design a wideband compact planar 5G mm-wave antenna. The 5G mm-wave system will operate on the different frequency bands depending on the region. Specially, if the mobile terminal is sold in multiple countries then an antenna should be able to operate at the large frequency spectrum from 24 to 40 GHz. However, usually the antenna bandwidth is closely related to the antenna electrical size. Also now-days the fullscreen mobile devices with greater then 85 % screen to body ratio and maximum ground plane clearance of less than 2 mm are widely spread. The aim of this subject is to design a wideband extremely low profile and compact antenna which can be used as an array element in 5G mm-wave mobile phased array.

Find the best possible array position on the phone chassis (with user) and prove that a divesity phased sub-array system is a very robust solution. It it known for a long time that the antenna position affects greatly the strength of the user effects. Furthermore, for the 5G mm-wave mobile antenna designer it is important to know which array positions on the ground plane is to choose when user is holding the phone. In this study, it has been attempted to find the best positions for the phased sub-arrays to achieve a similar performance as if all the edges of the device are filled with antennas. The least number of sub-arrays are wanted to achieve the optimal performance, as the physical space inside the device is scarce.

Find the most critical user gestures, make a measuremnet with multiple users based on these results and propose a model for spatial shadowing distribution. A user holding the mobile device by applying different gestures, but not all of the gestures affect the antennas in a similar way. Some of the gestures are more critical then others, which can be investigated by making multiple measurement for each gesture. For a company, it is extremely challenging to execute an over the air test for every possible gesture in order to get a 5G mm-wave mobile device certified. Furthermore, a number of most critical gestures can be used in design of a model for a user shadowing, which is currently extremely simplified in the 3GPP standards. The model can be based on the measurement with multiple users and critical gestures, which is the aim of this study. The proposed spatial user shadowing model would be a welcoming addition to the link simulations and network planning.

Discussion

In this Chapter the technical background knowledge needed for understanding of the thesis is presented.

General Theory

To make understanding the contents of this dissertation more approachable, some basic antenna theory will be presented in this section. In this theses, numerous measurements of the antenna radiation patterns with and without the influence of the user are presented. Concepts of the radiation pattern, gain and directivity are extremely important. Furthermore, polarization of the antenna and the axial ratio concept are also a very important parameters which used heavily in the paper B.

Radiation Parameters of Antennas

In this paragraph the concepts of radiation pattern, gain, half power beamwidth (HPBW) and other parameters corresponding to the radiation pattern will be presented.

An antenna radiation pattern or antenna pattern is defined as "a mathematical function or a graphical representation of the radiation properties of the antenna as a function of space coordinates". [41]

Usually a radiation pattern is defined in the farfield as multiple near field distributions can produce similar farfield radiation patterns. The farfield is characterized by the fact that the magnetic and electrical field components at that point are perpendicular to each other and the radio waves are planar. Farfield region is defined at the distance higher than $d = \frac{2D^2}{\lambda}$, where the D is the biggest dimension of the antenna and λ is a free space wavelength. The radiation pattern of the theoretical perfect isotropic radiator has a shape of a sphere, which means that the waves from the antenna radiate in all directions equally. In reality the radiation pattern can have different forms and shapes. For the directional antenna a radiation pattern is characterized by the main lobe, side lobe/lobes and back lobe/lobes in similar way as in Figure 3.1. However, if the geometry of the antenna is more complex then the radiation pattern can have multiple side, back and front lobes. The front to back ratio is a ratio describes the ratio between the main beam and the back lobe, and usually tells us how directive a particular antenna is. However, if the hands and head of the user is in the close proximity to the mobile device antenna then the radiation pattern would be heavily distorted and it will be hard to identify the side, back and front lobes. In this case the user will become a part of the antenna as a reflector.

Directivity of an antenna defined as “a ratio of the radiation intensity in a given direction from the antenna to the radiation intensity averaged over all directions”.[41]. The general formula for directivity is:

$$D(\theta,\phi) = \frac{U(\theta,\phi)}{U_0} = 4\pi\frac{U(\theta,\phi)}{P_{rad}} = 4\pi\frac{U(\theta,\phi)}{\int\limits_0^{2\pi}\int\limits_0^{\pi} U(\theta,\phi)\sin(\theta)d\theta d\phi} \tag{3.1}$$

where:

- “$U(\theta,\phi)$” is a radiation intensity in a given direction
- “U_0” is a radiation intensity averaged over all directions
- “P_{rad}” is a radiated power
- Element solid angle $d\Omega$ defined as $\sin(\theta)d\theta d\phi$

The maximum directivity is related to the width of the main beam and for some simple loss-less antennas can be predicted from the half power beamwidth (HPBW). However, if the radiation pattern is more complicated then the directivity will not directly correspond to the HPBW. Usually, width of the beam is defined between the points where the maximum radiated power is dropped by half as shown in Fig. 3.1. HPWB can be calculated from the radiation pattern for any of the chosen 2D planes, which can differ if the shape of the main beam is complicated. Antennas with the directive radiation pattern have a small HPBW, such as parabolic reflector or horn antennas. Thus, a good link stability between the two high gain antennas will highly depend on the main beam pointing accuracy.

The directivity of the antenna can only be used as a metric for the loss-less antenna, but in reality multiple losses from in the copper, and non-perfect matching will affect the radiation pattern. In practice the measure of antenna gain is often used instead:

$$G(\theta,\phi) = \eta_t D(\theta,\phi) \tag{3.2}$$

where:

- “$D(\theta,\phi)$” is a directivity in the θ,ϕ direction
- “η_t” is a total efficiency of the antenna/antenna system which include the missmatch, copper and dielectric losses.

The antenna gain can be measured by first measuring the reference antenna with a known gain, and then calibrating the measured radiation pattern of the DUT according to the reference antenna. In practice a horn antenna is usually used as a reference because of the known radiation pattern and high efficiency.

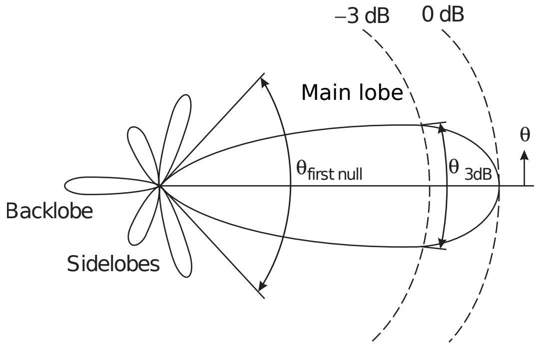

Fig. 3.1. 2D cut of a radiation pattern of the antenna in one plane [42].

Polarization

Polarization of the waves, which are radiated from the antenna indicates the time varying characteristics of the E-field at the particular point in space as shown in Fig. 3.2. Usually when looking on the polarization characteristics of the antenna, only the farfield region is considered at it simplifies the calculations. If two planar waves are propagating in x-direction, then z and y components of the electric field could be written as:

$$E_y = E_1 cos(\omega t)\hat{y} \tag{3.3}$$

$$E_z = E_2 cos(\omega t + \delta)\hat{z} \tag{3.4}$$

where:

- E_1 and E_2 are the amplitudes of the fields.
- ω is the angular frequency.
- $\hat{y}$ and $\hat{z}$ are the unit vectors.
- δ is an phase difference.

It can be clearly seen that in the farfield the different wave polarization will depend on the amplitudes of the E-field components and the angle between them.

If the phase difference is 0 than the antenna will be purely linearly polarized and the resultant E-field will be given as:

$$E = E_1 cos(\omega t)\hat{y} + E_2 cos(\omega t)\hat{z} \tag{3.5}$$

where magnitude and phase of the resultant E-field will can be written as:

$$|E| = \sqrt{E_1^2 + E_2^2} cos(\omega t) \tag{3.6}$$

$$\psi = tan^{-1}\frac{E_2}{E_1} \tag{3.7}$$

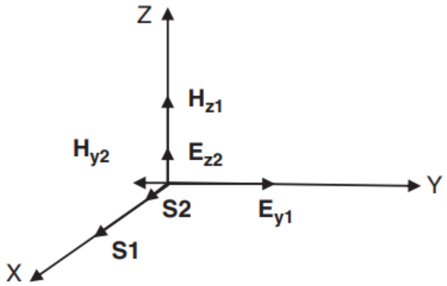

Fig. 3.2. Propagation of the waves in farfield in x-direction [43].

In physical sense, this means that the wave will always only propagate in one plane with time varying magnitude (maximum in $\pm\sqrt{E_1^2+E_2^2}$), and in other planes the magnitude of the E-field will be 0.

Circular polarization will be seen when $E_1 = E_2$ and $\delta = \pm\left(\frac{\pi}{2}+n\pi\right), n = 1,2,3...$ and the resultant field will be written as:

$$E = E_1 cos(\omega t)\hat{y} + E_2 cos\left(\omega t + \pm\left(\frac{\pi}{2}+n\pi\right)\right)\hat{z} \tag{3.8}$$

$$= E_m(\hat{y} \pm j\hat{z}) \tag{3.9}$$

where E_m is a magnitude of the resultant E-field.

The vectors will rotate in clockwise or anticlockwise depending on the sign and furthermore will depend on the direction of propagation. As shown in Fig. 3.3 depending on the sign inside the equation 3.9 the vector rotation direction be clockwise or anticlockwise. In this case the wave will change the plane of propagation depending on the phase difference δ.

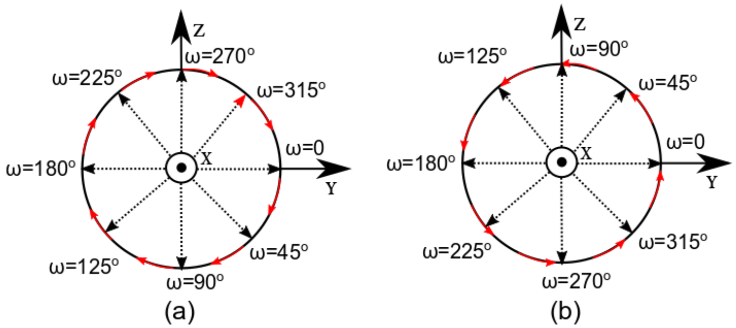

Fig. 3.3. E-field vector rotation direction for (a) left-handed and (b) right-handed circular polarization.[43]

However, in real life no antennas are exactly circularly or linearly polarized. For circular polarization it means that either angle between the two E-field vectors is not exactly 90 degrees or the magnitude of E_1 is not the same as the magnitude of E_2.

Usually the case is that for realistic circularly polarized antennas both criteria are not met exactly. It can be noticed that mathematically linear and circular polarizations are just a special cases of elliptical polarization which is a more general term for polarization characterization.

Thus, the resultant E-field for the elliptical polarization can be written as:

$$\begin{aligned} E &= E_1 cos(\omega t)\hat{y} + E_2 cos(\omega t + \delta)\hat{z} && (3.10)\\ &= E_1 cos(\omega t)\hat{y} + E_2 (cos(\omega t)cos(\delta) - sin(\omega t)sin(\delta))\hat{z} && (3.11)\\ &= \hat{y}E_1 + \hat{z}E_2 e^{j\delta} && (3.12)\end{aligned}$$

Then it can be shown that the trace of time-dependent vector is elliptical in nature by substituting $cos(\omega t) = Ey/E_1$

$$E_z = E_2 \left(\frac{E_y}{E_1} cos(\delta) - \sqrt{1 - \left(\frac{E_y}{E_1}\right)^2} sin(\delta) \right) \tag{3.13}$$

$$sin^2(\delta) = \left(\frac{E_z}{E_2}\right)^2 - 2\frac{E_y E_2}{E_1 E_2} cos(\delta) + \left(\frac{E_y}{E_1}\right)^2 \tag{3.14}$$

The equation 3.14 represents a polarization ellipse in Fig. 3.4. The axial ratio is given as a ratio between the major axes to the minor axes of the ellipse and can take a value between 1 and ∞.

$$AR = \frac{\text{major axes}}{\text{minor axes}} = \frac{OA}{OB} \tag{3.15}$$

where:

$$OA = \sqrt{\frac{1}{2}\left[E_1^2 + E_2^2 + \sqrt{E_1^4 + E_2^4 + 2E_1^2 E_2^2 cos(2\delta)}\right]} \tag{3.16}$$

$$OA = \sqrt{\frac{1}{2}\left[E_1^2 + E_2^2 - \sqrt{E_1^4 + E_2^4 + 2E_1^2 E_2^2 cos(2\delta)}\right]} \tag{3.17}$$

and the tilt angle of the ellipse can be written as:

$$\tau = \frac{1}{2}\arctan\left(\frac{2E_1 E_2}{E_1^2 - E_2^2}\cos(\delta)\right) \pm \frac{\pi}{2} \tag{3.18}$$

If axial ratio is 1 then the wave is circularly polarized and if the axial ratio is ∞ then the wave is purely linearly polarized. However, when talking about communication using two antennas the polarization miss-match will be an important factor because the polarizations of receiving and transmitter antennas usually are not the same. One of the most important quality metrics for a communication system is power gains and losses. Polarization miss-match between two antennas can be directly translated into the loss of EM power by using a metric called polarization loss factor (PLF). PLF is defined as:

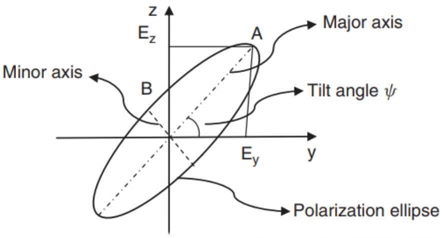

Fig. 3.4. Polarization ellipse.[43]

$$PLF = 10 \cdot log10(|\hat{\rho}_{Tx} \cdot \hat{\rho}_{Rx}|^2) \tag{3.19}$$

where $\hat{\rho}_{Tx}$ and $\hat{\rho}_{Rx}$ are the polarization vectors of receiving and transmitting antennas. If the PLF is 1(0 dB) then no polarization miss-match loss will be added to the system, but when PLF is equal to 0 ($-\infty$ dB) then two antennas have completely orthogonal polarization and no power will be transmitted from one antenna to another. It can be seen in Fig. 3.5 where the maximum and minimum polarization loss factor is calculated for the specific Tx and Rx antenna axial ratios. The figure can be red by making a straight line from the number found for one antenna on the first scale to the number found for the second antenna on the third scale and reading the middle scale for the RHC-RHC polarized antennas. It can be read that if one antenna is linearly polarized (usually the requirement for the linearly polarized antenna is AR of ≥ 40dB) and the purely circular polarized antenna with AR=0, then the constant loss of 3 dB is expected which is advantageous if one of the antennas can rotate in the unknown direction. However, in reality an of AR=3 dB is usually required throughout the whole antenna HPBW. This will mean that the polarization loss between the two circularly polarized antennas with AR=3 dB will be around 0.5 dB, which is enough in order to implement antenna tracking which is required for the antennas with narrow beam and dynamic orientation.

Surface Waves On a Typical Ground Plane

An electromagnetic surface wave created when a wave is guided along the planar interface made by two electromagnetically different materials. If those two materials are made identical then the surface wave will vanish. However, there is no guarantee that a chosen pair of materials will necessarily support the surface wave at a particular frequency. A fundamental property of a surface is that it must be guided along the direction which is parallel to the interface with the amplitude which decreases with distance away from the interfaces.

However, usually on the typical one layer PCB we will have three materials such as air, dielectric and a copper ground plane as shown in Fig. 3.6. Here both the TM and TE surface waves can be excited along a grounded dielectric sheet. The most of the field will be contained in, or near the dielectric material. At the higher frequencies the

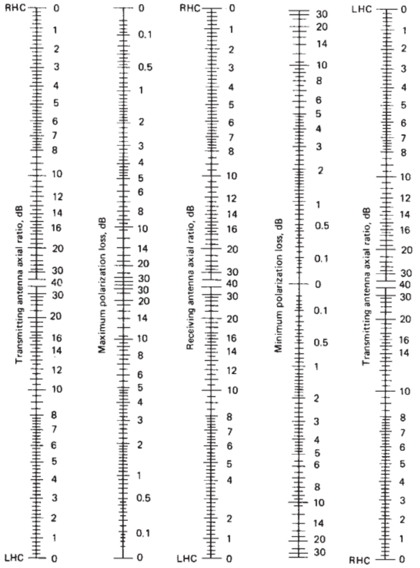

Fig. 3.5. Maximum and minimum polarization loss for the specific axial ratio.[44]

dielectric material will practically become a waveguide, however, the phase velocity of the wave in the dielectric will be lower than that in the free space. Furthermore, in some cases surface waves can also be excited on the planar transmission lines.

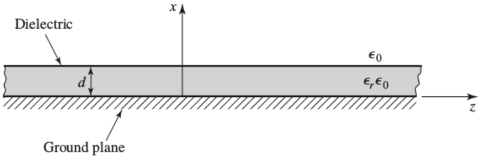

Fig. 3.6. Example of the grounded dielectric sheet [45].

For any sheet with thickness larger than 0 and a relative permittivity greater than 1, there exist at least one surface wave with a TM mode. This is the dominant mode of the dielectric slab waveguide, and it has a zero cutoff frequency. Lets take an example of a typical substrate used for making mm-wave antennas which has $d = 0.762\,\mathrm{mm}$ and $\varepsilon_r = 3.66$ for RogersRO4350B then the cutoff TE1 and TM1 modes of the surface wave could be computed as [45]:

$$TE_1 : f_c = \frac{n \cdot c}{4d\sqrt{\varepsilon_r - 1}} = \frac{3e8}{4 \cdot 0.762e-3 \cdot \sqrt{3.66-1}} = 60.35\,\mathrm{GHz} \tag{3.20}$$

$$TM_1 : f_c = \frac{(2 \cdot n - 1) \cdot c}{2d\sqrt{\varepsilon_r - 1}} = \frac{3e8}{2 \cdot 0.762e-3 \cdot \sqrt{3.66-1}} = 120.7\,\mathrm{GHz} \tag{3.21}$$

where “n” is a mode number, and TM_0 mode has a cut-off frequency of 0.

However, if the thickness of the substrate is increased to the most common 1.524 mm then the cutoff frequencies of $TE_1 : f_c = 30\,\mathrm{GHz}$ and $TM_1 : f_c = 60\,\mathrm{GHz}$ and it can be seen that TE_1 surface wave mode could affect the performance of the antenna which have a resonance frequency higher than 30 GHz. If the dielectric value is increased, which is typically done in order to and make the antenna smaller, then the cutoff frequencies of surface wave modes will move towards the lower frequencies. Thus, in theory if the surface wave is unwanted then the substrate should be thin with the low value of the dielectric constant.

Substrate Integrated Waveguide

Substrate integrated waveguide (SIW) can actually have similar performance as a commonly used metal rectangular waveguide, but is advantageous because of the planar structure. However, because the lossy substrate is used as a propagation medium for the SIW, the loss of this structure will be much higher than that of the rectangular metallic waveguide. SIW is easy to manufacture as the structure only consist of substrate with two copper planes and vias as shown in Fig. 3.7. The cutoff frequency of the SIW mostly depends on the width W_{SIW}, diameter of vias d and the distance between the vias p and can be described by the following equations by determining the width of the equivalent rectangular waveguide :

$$W_{EQ} = W_{SIW} - \frac{d^2}{0.95p} \tag{3.22}$$

$$p < \frac{\lambda_0}{2}\sqrt{\varepsilon_r} \tag{3.23}$$

$$p < 4d \tag{3.24}$$

In order to obtain the desired cut-off frequency of the fundamental SIW mode both inequalities in 3.24 should be satisfied. If the distance between the vias is too large than the waves will leak out of the SIW which will create additional losses. If designed correctly then the performance of the SIW should be very similar to the performance of the equivalent rectangular waveguide of the same width and height, filled with similar dielectric material.

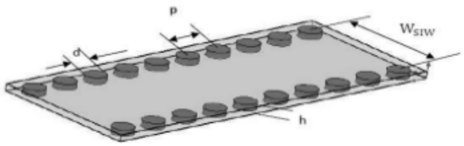

Fig. 3.7. Geometry of the generic substrate integrated waveguide.

Antenna Arrays

To understand how the antenna array works it is chosen to take a look at the simplest of arrays, which can be constructed from the elements with the isotropic radiation pattern. The electric field at a given spatial point for a simple isotropic radiator is given as:

$$E = C\frac{e^{i(k \cdot R+\phi)}}{R} \tag{3.25}$$

where:

- "C" is a real constant
- "k" is a wave number give by $\frac{2\pi}{\lambda}$
- "ϕ" is a phase of the wave
- "R" is a distance to the arbitrary point where the field is calculated

In Fig. 3.8 an array of two isotropic radiators is displayed and spaced with a distance "d" from each other. The locations of the isotropic radiators are denoted with the red circles. The field is calculated at the arbitrary point in farfield in the yz-plane. The distances from the observation point to the antenna elements 1 and 2 are denoted as R_1 and R_2 respectively. The distance from array center to the observation point is denoted as "R" and θ is an angle between the array and y-axes.

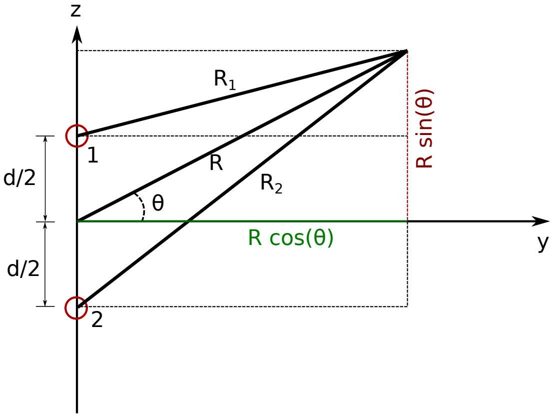

Fig. 3.8. Geometry of the two-element array.

A total field for the two isotropic radiators can be written as a sum of the fields radiated by each of them:

$$E = C_1\frac{e^{i(k \cdot R_1+\phi_1)}}{R_1} + C_2\frac{e^{i(k \cdot R_2+\phi_2)}}{R_2} \tag{3.26}$$

By using the Pythagoras formulas on the distances and angle in Figure 3.8, the distances from the array elements to the point in space can be calculated as:

$$R_1 = \sqrt{(R\cos(\theta))^2 + (R\sin(\theta) - d/2)^2} \tag{3.27}$$

$$R_2 = \sqrt{(R\cos(\theta))^2 + (R\sin(\theta) + d/2)^2} \tag{3.28}$$

By substituting the distances into Equation 3.26 the total field can be found as:

$$E = C_1 \frac{e^{i(k\cdot(\sqrt{(R\cos(\theta))^2+(R\sin(\theta)-d/2)^2})+\phi_1)}}{\sqrt{(R\cos(\theta))^2 + (R\sin(\theta) - d/2)^2}} + C_2 \frac{e^{i(k\cdot(\sqrt{(R\cos(\theta))^2+(R\sin(\theta)+d/2)^2})+\phi_2)}}{\sqrt{(R\cos(\theta))^2 + (R\sin(\theta) + d/2)^2}} \tag{3.29}$$

From Equation 3.29 it can be seen that the change in a field radiated by an antenna array at the chosen arbitrary point can only be affected by the distance between elements ($d/2$) or a particular element's phase (ϕ). If the distance between two elements increase then the width of the main lobe of the radiation pattern will become more narrow but the sidelobes will be bigger as well. The compromise between a width of the main lobe and the size of the side lobes is very important when designing an antenna array.

Uniform array An array of identical elements with the same magnitude at the element's feeding points referred to as a uniform array [41]. Different shapes of the uniform arrays can be obtained, such as, linear, planar, circular, l-shaped, etc. A radiation pattern of a uniform array for an arbitrary array element can be written as [46] :

$$D_{array}(\theta, \phi) = D_{element}(\theta, \phi) AF \tag{3.30}$$

where $D_{element}(\theta, \phi)$ is a radiation pattern of a one element and $AF(\theta, \phi)$ is an array factor that can be expressed as: [46]

$$AF = \sum_{i=1}^{N} w_i e^{-j\cdot k\cdot r_i} \tag{3.31}$$

where:

- "N" is a number of array elements
- "w_i" is a complex weight for each element branch
- "k" is a wave number
- "r_i" is a position of each array element in the (x,y,z) coordinate system

In Fig. 3.9 the basic antenna array concept is shown. In the case of the uniform array, each antenna element will have similar radiation pattern and can directly correspond to Equations 3.31 and 3.30.

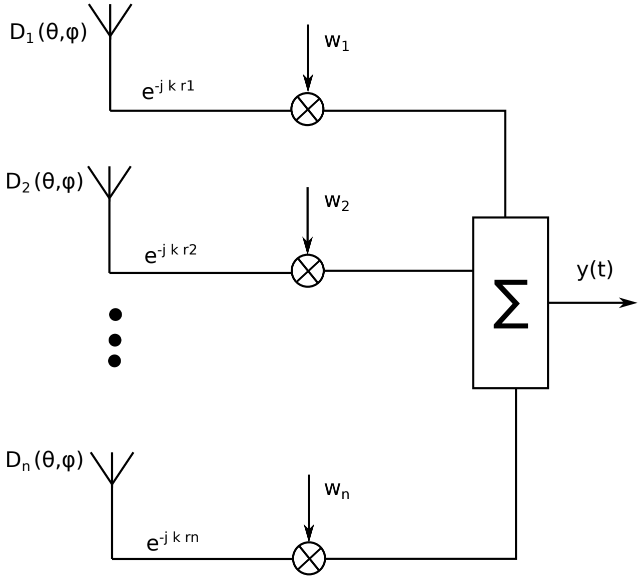

Fig. 3.9. Basic antenna array concept.

For the different applications a certain weights can be applied at the each element feeding point.

Most popular weighting methods are:

- Phased Arrays – complex phasors are used as weights so the radiation pattern of the main beam direction of the radiation pattern can be altered.
- Schelkunoff Polynomial Method (Null Placement) – weights are selected in such way so radiation pattern has nulls in chosen directions [46].
- Dolph-Tschebysheff Weights – Weights are chosen in such a way so the most dominant side lobes are reduced in expense of raising the less dominant side lobes. [46]
- MMSE Weights – Weights are chosen in such way so the Mean Square Error (MSE) between the desired output and actual output is minimized [46]
- Adaptive Antenna Arrays and The LMS Algorithm – The weights are based on the MMSE for a particular environment.[46]

By using the right combination of the magnitude and the phase of each weight, the one or more weighting methods can be applied for the specific array application.

Mutual Coupling When two or more antennas with the same frequency band are placed close to each other and transmit or receive at the same time, some of the energy from one antenna will transfer to other antennas. This effect is called mutual coupling and usually can be measured as a gain from one port in the network to the other (for example S_{21}). The antennas further away from the driven element will have less mutual coupling.

The energy transferred between the elements depends on the characteristics such as:

- Radiation pattern of each array element (if array is not uniform)
- Separation between array elements (If the array is not uniform)
- Relative orientation of each array element (if the radiation pattern of the elements is not unidirectional)

In many cases, mutual coupling will make the design and analysis of the antenna array more complicated [41]. So the mutual coupling can be reduced by placing antennas further away from each other, which will result in the higher sidelobes or orienting the element in such as way so less current is induced on the neighboring elements.

Mutual coupling in transmit and receive modes are shown on Fig. 3.10.

In the transmit mode the mutual coupling will follow 5 steps:

- ⓪ Energy generated towards the antenna n from the generator.
- ① Energy is radiated into space
- ② Some amount of energy will transfer to the antenna m
- ③ Some amount of energy will be scattered from antenna m into space
- ④ Remaining energy will travel back into transmission line of antenna m
- ⑤ A part of the energy, radiated into space from antenna m, will transfer to the antenna n

And in the receiving mode:

- ⓪ A wave front strikes antenna m and causes current flow
- ① A part of the incident plane wave is transmitted in the transmission line of antenna m
- ② A part of the incident plane wave is reflected back into the space
- ③ The other part of energy will transfer to the antenna n
- ④ Energy reflected back into space can be controlled by changing the matching of the antenna.

The mutual coupling can be used to modify the radiation pattern or/and matching of the antenna array. However, the mutual coupling can correlate signals between the antennas, which i very important when designing an array system for exploiting

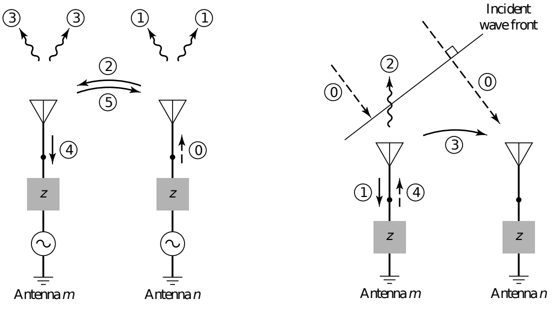

(a) Transmitting (b) Receiving

Fig. 3.10. Coupling between antennas in transmit and receive modes [41].

the spacial diversity. Furthermore, the efficiency of the array will drop if the mutual coupling is too high. For the antenna array of two elements the coupling loss will add up to the missmatch loss of the array element:

$$L = -10 \cdot log_{10}(1 - S11 - S_{21}) \tag{3.32}$$

Where the S_{21} is the antenna isolation, which can be measured by the vector network analyzer.

5G Mm-wave Mobile Antenna Types

As it have been discussed in the Introduction, a 5G mm-wave antenna need to have a high gain, but also able to change the mean beam direction dynamically. Typically the antenna elements, such as, dipoles, monopoles, IFAs, PIFAs, folded monopoles, etc. do not have a high gain. Such antennas as horn antenna can have much larger gain up to 24 dBi, but usually such antennas are bulky and not suitable for the implementation in compact devices. The lenses and passive elements can be implemented in order to increase the directivity of the 5G mm-wave antenna as well. It has been shown earlier that by increasing the aperture of the antenna, the directivity will become larger. Most convenient way of increasing the antenna aperture is to make an array of multiple elements. Arrays can be made up of the same element type or use different elements. Elements are often placed in the periodic way but some antenna arrays with the random placement of the elements could also be constructed.

Phased Antenna Arrays

The most common approach is to implement the beamforming is by means of the phased array antenna. The signal associated with the individual antenna elements is adjusted in phase and magnitude in order to make the waves radiated from the antenna to add up in phase in the desired direction. As discussed earlier, depending on the weights at the feeding ports of the antenna elements, the beam direction can be adjusted and sidelobe level could be suppressed. However, this approach have multiple limitations in respect to the other beamforming approaches.

Lets take an example of a linear array consisting of 6 isotropic elements operating at the frequency of 300 MHz. When the distance between elements is increased from $\lambda/4$ to $1\frac{\lambda}{2}$ as shown in Fig. 3.12 multiple interesting phenomena will occur. As it is known from the Friis equation, the directivity of the array will increase with the size of the aperture (in this case the size of the array). However, no sidelobes can be seen when the half wavelength distance between elements is chosen in Fig. (a). Furthermore, the number of the sidelobes grows from two in Fig. (b) to 12 in Fig. (d). Never the less, the size of the sidelobes is quite small if no specific weights are applied to the array.

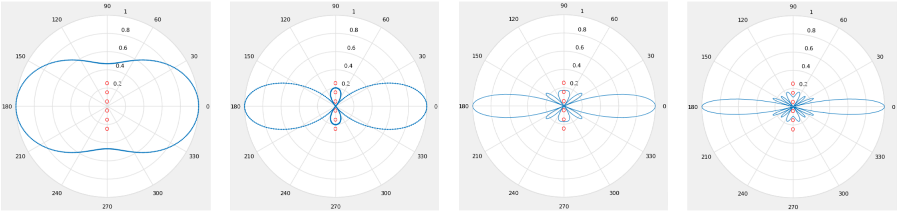

((a)) ((b)) ((c)) ((d))

Fig. 3.11. Normalized radiation pattern of the array of 6 isotropic antenna elements when distance between elements is (a) $\lambda/4$, (b) $\lambda/2$, (c) λ, and (d) $1\frac{\lambda}{2}$

However, the picture changes quite a lot when the beam is scanned from the broadside to the endfire (parallel to the linear array) direction in the four arrays with different inter-element distance. In the following four arrays the beam is scanned from 0 degree to 90 degree with a step of 30 degrees. As it is shown in Figs (a), (b), (c), (d) already when the beam is scanned up to 30 degrees then the gratin lobe will appear in the array with the inter-element distance of $\geq \lambda/4$. Furthermore, the gratin lobe in Fig. (d) is very large and this array will not be useful for the communication purposes, as the gratin lobe will pick up great amount of the interference in the direction of 270 degrees in the plot. Next, when the beam is scanned to 60° a gratin lobe in Fig. (e) is quite small, but the directivity of the array is very low as well and the main beam becomes extremely wide. The array configuration in Fig. (h) is totally unusable. Finally, when the beam is scanned all the way to the endfire direction (90 degree) the sidelobes will grow considerably even for an array with inter-element distance of $\lambda/2$. However, if there are no interferers in direction of 270 degree then the configuration with the distance between elements of λ can also be useful in Fig. (k).

From this investigation it can be noticed that in order to achieve the best sidelobe and gratin lobe suppression, the distance between elements of $\leq \lambda/2$ should be chosen. However, when the distance between elements becomes smaller than the directivity of the array will decrease considerably. Furthermore, mutual coupling between the elements will increase as well and thus the extra losses will be added. On the other hand, when the distance between elements is larger than $\lambda/2$ then the width of the main beam and directivity of the array will increase, but the gratin lobe and sidelobes will increase as well. When the distance between elements is $1\frac{\lambda}{2}$ the gratin lobes will be stronger than main lobe for some scan angles. This compromise is extremely important to have in mind when designing a wideband phased arrays. For example, if a wideband antenna is constructed ($f = 24 - 40\,\mathrm{GHz}$) for the 5G mobile device then the wavelength at the lowest frequency will be 12.5 mm and 7.5 mm at the highest frequency. So, if an array is designed after the lowest frequency then the distance between the elements will be 6.25 mm which will correspond to the $\lambda/1.2$. Thus, bigger gratin lobe and sidelobes will be expected at the highest frequency. So instead, the distance between element could be chosen from the center frequency $f_c = 32\,\mathrm{GHz}$. Thus, the distance between elements will be chosen to 4.68 mm, which is approximately $\lambda/2.7$ at the lowest frequency and $\lambda/1.6$ at the highest.

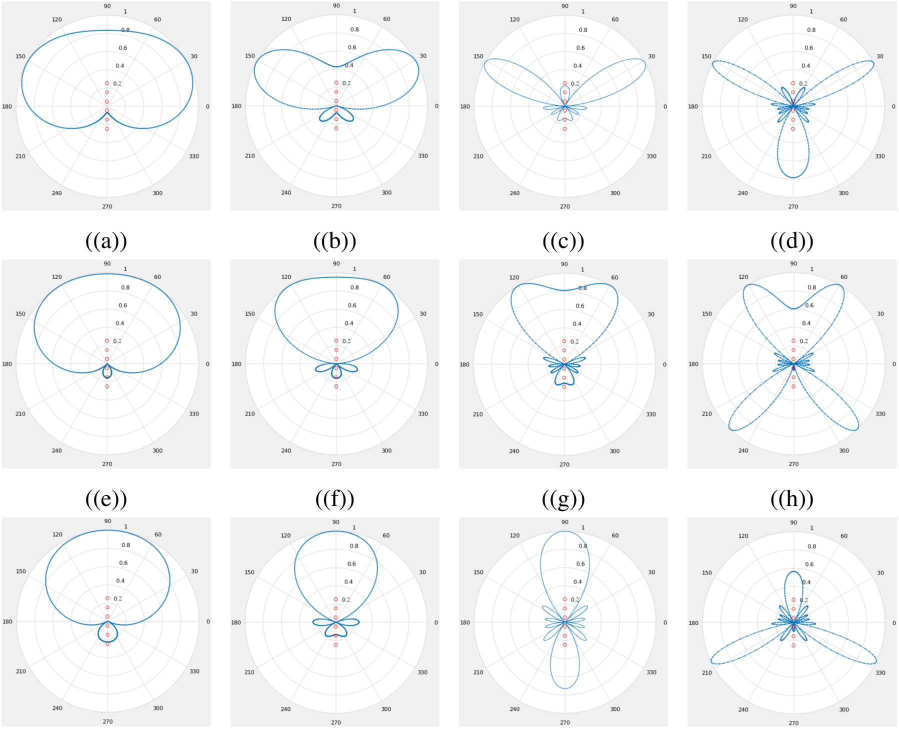

((a)) ((b)) ((c)) ((d))

((e)) ((f)) ((g)) ((h))

((i)) ((j)) ((k)) ((l))

Fig. 3.12. Normalized radiation pattern of the array of 6 isotropic antenna elements when distance between elements and scan angle is (a) 30 degree - $\lambda/4$, (b) 30 degree - $\lambda/2$, (c) 30 degree - λ, (d) 30 degree - $1\frac{\lambda}{2}$, (e) 60 degree - $\lambda/4$, (f) 60 degree - $\lambda/2$, (g) 60 degree - λ, (h) 60 degree - $1\frac{\lambda}{2}$, (i) 90 degree - $\lambda/4$, (j) 90 degree - $\lambda/2$, (k) 90 degree - λ, and (l) 90 degree - $1\frac{\lambda}{2}$.

For the uniform elements, a spherical coverage for all steering states of the phased array will be same as the element's pattern multiplied by the number of elements squared. However, when designing a phased array in a small mobile device form factor, the radiation pattern of array elements will highly depend on the location of the element. For example, different element will excite surface wave differently, depending on the position of excitation. Furthermore, edge reflections will also affect the two edge elements and disturb the radiation pattern.

There are multiple approaches in which a phased array can be constructed:

1. Analog beam forming - apply tunable analog circuits on each element to set the predefined amplitude and phase values.
2. Beam switching - array have multiple switched inputs to a beamforming network like lens or Butler matrix and output one beam in the desired direction.
3. Digital beam forming - signals are multiplied by the coefficients in the baseband which makes it more flexible but increase the cost and complexity of the network. The DACs and ADCs circuits used for the digital beamforming implementation are hard to make stable along the wide bandwidth with low power consummation.
4. Hybrid beam forming - use analog beamforming for the sub-group of elements, but connection between sub-groups done digitally, which reduce the number of DACs abd ADCs while keeping some of flexibility of the digital beamforming.

In the analog beamforming a simple weighting algorithm is applied by means of analog devices such as switches or phase shifters. Multiple phase shifters in the antenna array can introduce high insertion losses at mmWave frequency bands so additional PA/LNA gain is required in the front-end. A number of alternative antenna solutions have been proposed for 5G mobile terminals to reduce the number of the phase shifter or even avoid them entirely. A beam switch array with a passive beamforming circuit such as a lens antenna or a Butler matrix, is an approach that can generate beams in the predefined directions and can also be fully integrated with an antenna array. A parasitic reflector is also a possible replacement candidate for an adaptive array in the mobile terminals, particularly at higher frequency mmWave bands. By implementing multiple feedings with the reactive loaded passive elements at the different positions, it is possible to generate multiple predefined high gain beams.

There are multiple additional challenges and impairments associated with the circuits used in analog or hybrid systems. The magnitude/phase/delay differences between the signal paths for the elements must be accurate and stable considering the manufacturing variations and operational conditions. Ideally any differences in the device performance should be consistent in the array so a calibration for the beam formation would be greatly reduced or eliminated. Usually an RF front-end circuit is combined with an antenna element so the manufacturing of these front could be highly reproducible.

While the phased array provides to be the most flexible and best performing beamforming solution, it may not be the optimal approach for mobile terminal applications where antenna gain requirements are substantially lower than for base stations and where cost and size are at a premium. Alternative solutions include switching of fixed high-gain antennas. A switched array of high-gain antennas is the simplest system to implement. It benefits from the beam steering that is robust by design and is low cost and a single IC can provide the RF front-end switching. Drawbacks of this approach include the higher requirements for a power inside a power amplifier and a low-loss multi-throw switches. Reactive beam steering uses a tunable/reconfigurable reflectors and/or directors to steer the beam of a single active antenna element. It approach is also low cost implemented with the tunable reactive terminations. It is more complex than the switched array because the beam steering depends highly on the accurate settings of the reconfigurable reactive terminations. However, it does not require low loss multi-throw switches. The combined antenna system is much smaller than the multiple high-gain antennas or a phased array.

Pattern Reconfigurable Antennas

Parasitic tuning is a method of altering the antenna radiation pattern by adding a number of switchable parasitic elements, which can act as directors or reflectors. This method has advantages such as isolation of the driven element from the tuned elements. Parasitic tuning relies on the mutual coupling between the driven element and parasitic element/elements, however if the coupling is too high, then the efficiency of the driven element will decrease. But if the coupling is too low, the radiation pattern will not change significantly. Furthermore, the coupling of the passive elements will change the impedance matching of the driven element in most cases. The passive element tuning technique has also been utilized to change the radiation pattern direction in the [47], [48], and [49], where the planar antenna is printed as a copper strip on the PCB. The parasitic elements, designed in [48] and [49], can be grounded by the use of switches (diodes, RF-mems, or transistors). By changing the operating order of the switches the proposed passive elements can act as both directors or reflectors. On the other hand, in [47] the switches were used to change the electrical length of the parasitic elements.

The one of the most famous parasitically tuned antennas is the Yagi-Uda antenna. In the Yagi-Uda, the driven element is usually a half wave dipole. One or multiple reflectors are located behind and the directors are located in front of the driven element element. The reflectors are more inductive then the driven element (longer) and the directors are more capacitive (shorter).

Yagi-Uda antenna can get much higher directivity than an ordinary dipole. However, the size of the antenna is considerably larger. The antenna structure is made from a driven element and a number of parasitic elements which share the same polarization characteristics. Advantage of the Yagi antenna for the 5G mm-wave mobile application is that the driven element can be made wideband, which is quite challenging for the whole phased array.

The Yagi-Uda antenna configuration is shown in Fig. 3.13. The driven element is located in the origin of the coordinate system and the antenna radiate towards

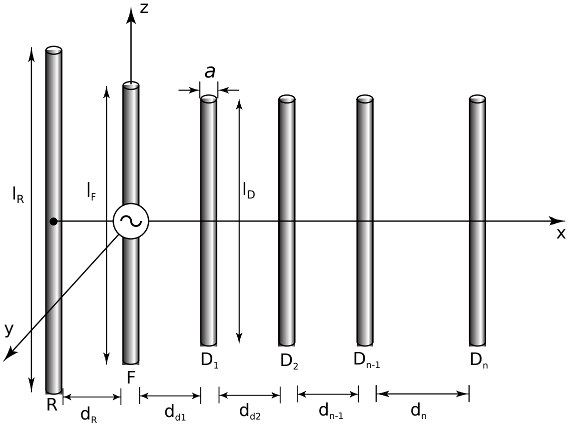

Fig. 3.13. Yagi-Uda antenna array [41]

+x direction. The driven element denoted as F with the passive elements directors D_1,D_2,D_{n-1},...,D_n and the reflector R. Ideally the parasitic elements will re-radiate the signal with a small phase change along the whole structure. The optimum distance between a driven element and a reflector is usually smaller than that between driven element and a director in Figure 3.13 d_R is smaller than d_{D1}. The reflector is usually about 5 % longer than the driven element and the reflector is 5 % shorter. In the application if the reconfigurability is required then a passive element can be made inductive by adding the extra length, but it is quire difficult to subtract the length from an element. However, a tunable capacitor could be implemented to made a passive element more capacitive and thus make it into a director. The impedance of a driven element will decrease with the number of directors. The spacing between the directors and the initial impedance of the driven element should be chosen to the impedance of the complete structure is $50\,\Omega$

The number will decide the directivity of the antenna array and the size of the rear and back lobes. The distance between the driven element and the neighboring passive elements will affect the side and back lobes as well. For example, if the spacing between the driven element and the first director is chosen to be 0.4λ, the spacing between the driven element and reflector is chosen to 0.3λ and the thickness of all elements are chosen to be 0.032ˇ.

Rotman Lens

Lens antennas are usually applied in the communication system when a very narrow beam and high gain are desired. Similar to the lens in optics, the EM lens will create the plane wavefront in the desired direction. A shape and a direction of the formed beam will depend on the the lens geometry and the position of the driven element. However, typically most lenses are quite bulky and made of rather expensive materials. If we want to implement a planar lens, then a new integrated in the PCB design is needed. This novel lens design has been proposed by W. Rotman [50] in 1963 and the geometry is shown in Fig. 3.14 with the lens embedded in between two parallel plates. Multiple horns illuminate the lens at the different angles and on the opposite end of the lens a linear array is located. The number of the radiators will directly correspond to the maximum gain of the structure. The idea is that a gain of the array will be much higher than that of a single horn antenna. When operational a wave will propagate through the lens and arrive at the different time for each RF probe, and thus, a signal's phase at each radiator will be different and the directive beam in the chosen direction will be formed in Fig. 3.14.

However, the design proposed by the Rotman is rather bulky and include RF coaxial cables, and horn antennas. If an SIW technology is used, then both horns and linear array of radiators can be integrated into the PCB, but in this case the loss of the structure will be higher because of the losses in the dielectric.

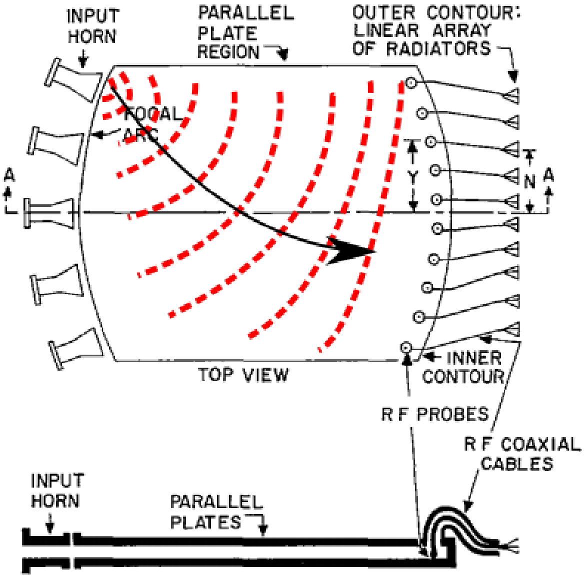

Fig. 3.14. Geometry of the Rotman lens and the driven elements [50].

Butler Matrix

In respect to the lens antenna approach, a Butler matrix utilizes multiple microwave components, such as hybrid couplers with a phase shift, crossovers and 45 degree junctions to achieve the beemseering. To understand a concept of a Butler matrix, a simple 4-by-4 structure can be considered as shown in Fig. (a). The resulting structure has 4 inputs which correspond to the four distinct beams. In order to synthesize the beams, it is necessary to implement the matrix with four 90° couplers, two crossovers and two 45° phase shifters. At the top end of the matrix, four antenna elements are located. The type of element can be chosen arbitrarily, and will depend on the desired radiation direction. It can already be seen that such a matrix becomes quite large when a number of the input ports and antennas elements increase. Furthermore, the length of the matrix will affect the insertion loss of the structure. The Butler matrix components can be implemented using different transmission line technologies, such as microstrip, stripline, SIW or others. It should be pointed out that matrices bigger than 4X4 will not be directly applicable to the 5G mobile terminals because of the physical size of the network and high insertion losses.

To understand how the Butler matrix works, it has been chosen to show the distribution of the signal phase when it propagates thought the structure, fed at the port 1 in Fig. (b) and port 2 in Fig. (c). The phase distribution for the ports 3 and 4 are not shown, as it will be the same as that for port 1 and 2 but mirrored because of the matrix symmetry.

User Effects

As an antenna inside a mobile terminal will always be close to the user tissue, the mobile antenna designer should always take user effects in the consideration. Main two parts of the user effects are the user blockage and the body loss. These two effects would always be present when the user is holding a smartpone in the hand. However, at the sub-6GHz frequencies the body loss will be more dominant then the shadowing loss, specially because the antenna radiation pattern at the GSM and LTE frequencies is omnidirectional. But at sub-mm and mm-wave frequencies the shadowing will make a huge impact on the communication link stability because of the highly directive beamforming antennas at both mobile and base stations. The distribution of the user effects will surely change if the future form factor of the mobile terminal is considerably different than the current but the user impact will always be present in some form or other.

Body Loss

Usually in the mobile communication system a user should always be considered when handheld device antenna is designed. At the lower LTE/GSM frequencies ($\leq$ 6 GHz) the impact of the user on the mobile phone antennas consists of the absorption and miss-match losses $L_{body} = L_{missmatch} + L_{absorption}$. The body loss can be computed by measuring the efficiency with and without the user:

$$L_{body} = e_{tot,free} - e_{tot,user} \tag{3.33}$$

The detuning and absorption happens when when the user's tissue is located inside the reactive nearfield of the antenna, which is the closest space surrounding the antenna. The approximate distance to the reactive nearfield boundary from the antenna surface

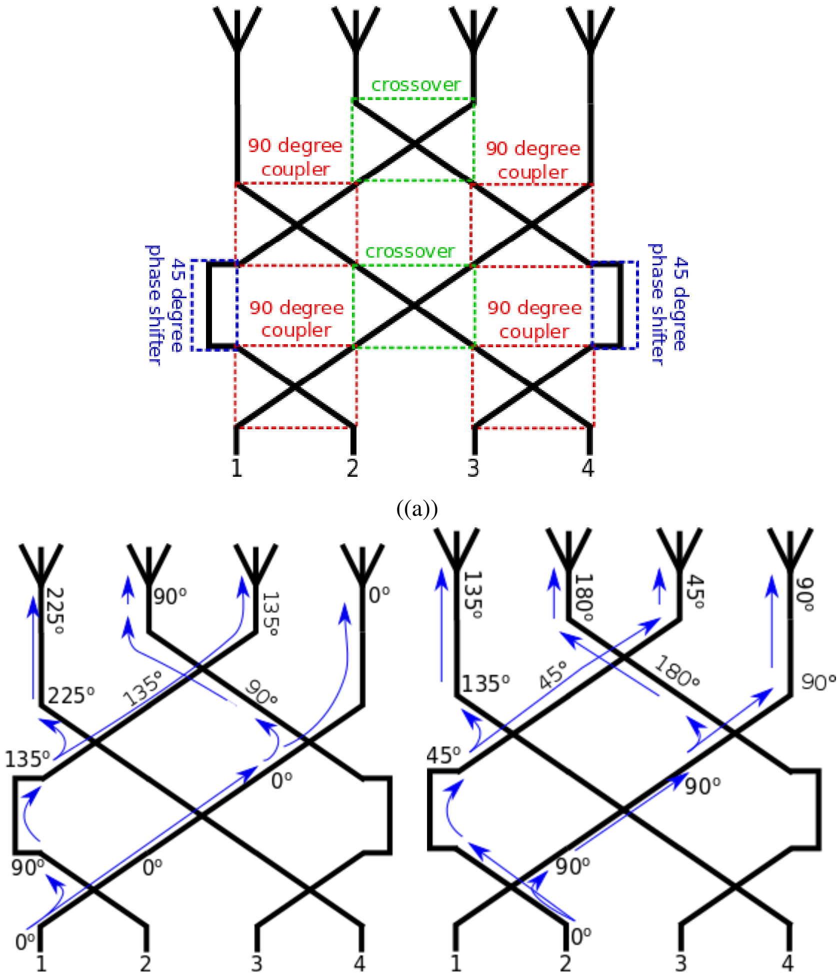

((a))

((b)) ((c))

Fig. 3.15. (a) geometry of the Butler matrix, and signal phase distribution when matrix is fed at the (b) port 1 and (c) port 2.

can be calculated as [41]:

$$R = 0.62\sqrt{\frac{D^3}{\lambda}} \tag{3.34}$$

where D is the largest dimension of the antenna. The distance can be computed for the LTE antenna radiating at the commonly frequency of 700 MHz, then for the half wave dipole with largest dimension of $D = \lambda/2 = 0.214\,\mathrm{m}$ and radius:

$$R_{700MHz} = 0.62\sqrt{\frac{0.214^3}{0.428}} = 9.3\,\mathrm{cm} \tag{3.35}$$

Which means that if the user's fingers or palm is at least 9.3 cm away from the antenna then the detuning will occur. This effect is quite difficult to avoid because the typical ground plane size of the modern mobile device is around 7x16 cm which means that if the low frequency antenna will fully typically occupy one of the short edges of the phone.

On the other hand, at the mm-wave frequencies the detuning and absorption losses are much lower as the reactive nearfield region is very small and can actually be compared to thickness of the mobile device case:

$$R_{28GHz} = 0.62\sqrt{\frac{0.0054^3}{0.0107}} = 2.3\,\mathrm{mm} \tag{3.36}$$

However, if an antenna element is put into an array then the nearfield region will be larger as the aperture of the radiating structure will be larger as well. Let's take an array of 8 dipole elements with a half wavelength spacing between elements. If the the largest dimension of the structure is $D = 7.5\lambda$ then the distance to the nearfield boundary from the antenna surface can be calculated to:

$$R_{28GHz,array} = 0.62\sqrt{\frac{(7.5\cdot 0.0054)^3}{7.5\cdot 0.0107}} = 1.8\,\mathrm{cm} \tag{3.37}$$

According to the theory, the body loss will occur when the living tissue of the user is at least in 1.8 cm proximity of the antenna structure. To test this theory, a simulation setup with a single dipole and an 8-element array is made from the same dipole elements as seen in Fig. 3.16. Dipole is made of a simple copper sheet with the length of 4.37 mm and a center frequency of 28 GHz. A chosen dipole has an omnidirectional radiation pattern in yz-plane, thus, it has been chosen to put a block of the dielectric human tissue in that plane to induce highest fields on the tissue block. The uniform tissue block is made of skin because as it has been discussed in paper B and E, that the skin tissue can approximate quite well the human tissue properties at 28 GHz. The length of the block is 37.5 mm and the width is 10 mm with a thickness of 3 mm. The distance between the antennas and the tissue block is swept from 1 to 20 mm while making a full FDTD simulation for every sweep. The lowest distance has been chosen 1 mm lower than the result of Equation 3.36 and the biggest distance is chosen is 2 mm higher than that in the Equation 3.37.

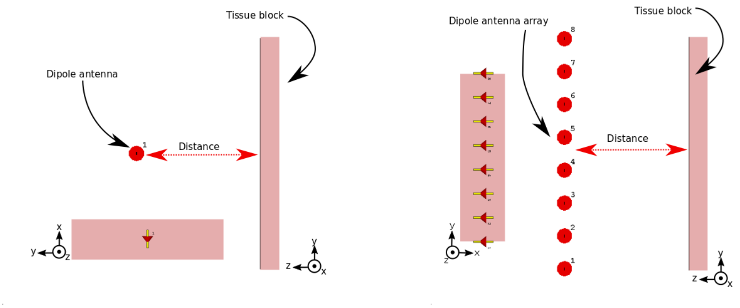

((a)) ((b))

Fig. 3.16. Test setups in xy and yz-planes for (a) one antenna and (b) antenna array.

The radiation patterns in yz-plane are shown for a single antenna in Fig. (b) and for an array in Fig. (b) for all of the distances. It can be noticed that the radiation in direction of $\theta = 180°$ is reduced when the tissue block is in close proximity. The reference radiation pattern in free space without the skin tissue block is plotted with a thick black line. Because of the tissue blockage, the radiation in the $\theta = 0°$ direction will be higher, because of the reflections from the block.

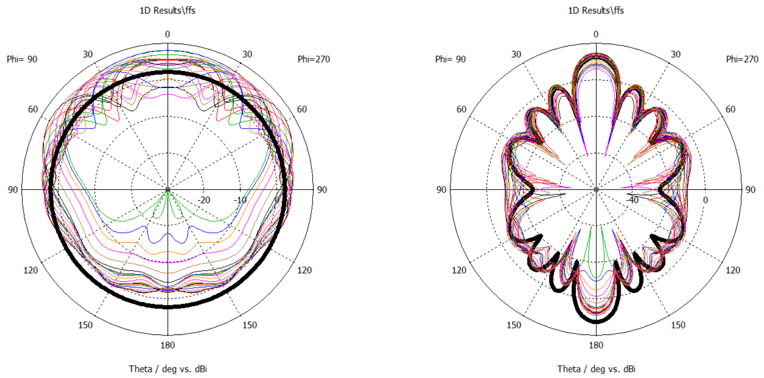

((a)) ((b))

Fig. 3.17. Radiation patterns in yz-plane for (a) one antenna and (b) antenna array when the distance sweep between the tissue block and antenna.

When looking on the radiation and total efficiency in Fig. 3.18, it can clearly be seen that following the theory discussed in this section, a single element have smaller nearfield region and thus the efficiency over 80 % can be seen for the distance higher than 3 mm. The missmatch loss (difference between radiation and the total efficiency) is also very low. However, from the simulation results with the dipole array it can be noticed that sometimes the missmatch loss of 1.5 dB can be observed, which indicate the resonant frequency shift away from 28 GHz. Furthermore, the efficiency curves follow a similar wavy tendency as for one element, but the wave is much stronger for the array. This means that sometimes the radiation efficiency for the array is as high as the one for a single element at the distances of 3, 9, 14 and 20 mm. The missmatch loss is always higher for the array, than that for a single element. From the results it can be seen that if the body loss is to be avoided than the case of the mobile device should be around 3 mm away from the antenna elements. This would mean that in real work scenario with the 5G mm-wave phased array mounted on the mobile device, the body loss measured in paper A would be higher.

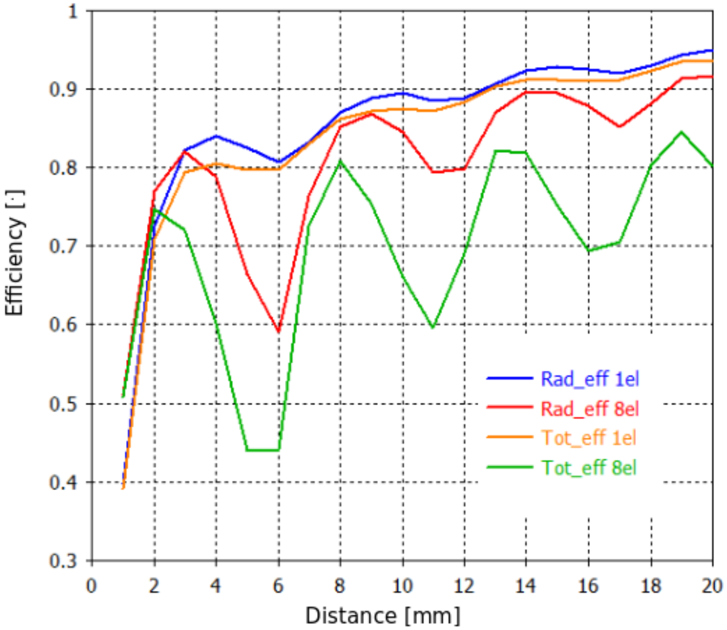

Fig. 3.18. Radiation and total efficiency comparison of the 1 antenna and 8 element array for the different distances between tissue block and antennas.

User Shadowing

The blockage from the user will appear at all the frequencies, however with the higher frequency the strength of the blockage will increase. It has been already shown in Paper A, that the body loss of a single mm-wave mobile antenna is not a high as that at the GSM and LTE frequencies. Furthermore, because the 5G system will include beamforming capabilities not only at the base but also at the mobile station, a shadowing from the user will impact that performance severally. Do describe the shadowing spatial distribution a metric of coverage efficiency can be used and then a total loss in coverage can be calculated from the free space to the case with the user. However, coverage efficiency did not tell us which part of the space is blocked by the user and how severe is the blockage. The position and size of the blocked area is specially important when the used is standing with his back to the base station, and in this case the beamforming will not always be a most preferable option. In respect to the sub-6GHz frequencies, at the 5G mm-wave 28 and 40GHz bands, the surface wave will be more efficiently excited on the user's hands, arms, or the face. Furthermore, the reflections from the user's clothing will be more secular because surface roughness will play a higher role at these frequencies. Here to describe the shadowing a metrics of SAPR and SIAPR have been introduced in paper A. Even though, the form factor of the mobile device could change in the future, the proposed metrics could be used as a general measure of the shadowing from the user. An wireless communication system engineer would be able to include different margins in the system:

- Spherical coverage margin. After measuring a phone with different user gestures determine the mean coverage efficiency expected from the chosen antenna.
- Mean blockage. Mean blockage could be described by SAPR or SIAPR which shows the worst possible blockage to be expected when the base station is located behind the user. To combat that blockage, more base stations would be required to provide good quality of service.
- Shadowing CDF, which will shown how much the shadowing can vary from user to user or from gesture to gesture. Based on the obtained shadowing CDF a simple random process could be made and included in the link simulator to check if the bit error rate is above the acceptable level.

Most of the results in this thesis are based on the either simulations or measurements with the user, which is not 100% accurate, but the main contributions of the thesis is multiple novel metrics and techniques which could be used for any given antenna-user setup. For example, in paper E it has been shown that part of the user blockage could be mitigated by antenna diversity which would hold true for any given antenna and user gesture, however if the form factor of the device is changed considerably, then the user gesture will change considerably as well. Thus, the proposed antenna array configuration would be mostly applicable for the present 5G smartphones. Depending on the form factor and antenna type the gain from the antenna diversity will vary, but as long the user holding the phone is one or two hands the corner positions will always be advantageous. It has also been found that the antenna location will highly influence the user effects, but in real world the manufacturer will surely place a 5G antenna array in the place which is available in the already crowded smartphone. Thus, while the guidelines provided in this thesis shows the best possible antenna location, it is not 100% sure that the antenna will be placed in exactly the same location. This will lead to the lower antenna performance, which could be mitigated by the increased number of base stations or by increasing the transmit power and receiver sensitivity, which will highly depend on the cost of the components of the wireless system.

Furthermore, in this paper is it assumed that the measured antenna with the user is in the farfield. However, this may not be the case as the farfield criteria will depend on the antenna aperture, which will include the user. As the surface wave is excited on the user, different parts or even the whole user would effectively become a part of the antenna and not the part of the environment. In paper B it has been displayed that the proposed human phantom has very similar external properties as the human. However, we should remember that in the simulation the user have a static gesture and do not have any clothing. Also the user will do small involuntarily movements, because the measurement time of around 20 minutes. In all of the measurements with the user it can be noticed that shadowing area appears bigger than the simulations, which could also indicate that the user under the test did not stand exactly still. A measurement with the phantom would confirm the accuracy of the proposed phantom better than the measurement with the live user.

Finally, in the statistical measurements the results are highly depend on the sample size. A user sample in the paper A is significantly different than that in the paper F. However, this would be acceptable as the work in paper A was a starting point in the investigation of user effect for the 5G mobile terminals. Where in paper F, the users with different heights and gender have been measured considering the most critical gestures to assure the highest variance between the users. The model made in the paper F is more reliable then the mean results in paper A, where the user sample have been chosen randomly from the students on the Master's program.

Contributions

This chapter presents the main contributions of this thesis together with brief summaries of the motivation, work and findings of the papers included in Part II.

The main contributions of this thesis can be listed as below where the corresponding paper(s) are indicated in parentheses.

1. Novel metrics for the user shadowing characterization (Papers A, B, F).
2. Novel wideband quad mode compact antenna structure design principles (Paper D).
3. Guidelines on the best 5G mm-wave mobile sub-array placement (Paper E).
4. Proposal of a homogeneous human phantom model for simulations with 5G mm-wave antennas (Paper B).
5. Proposal of a novel stochastic model for the characterization of the spatial human shadowing distribution (Paper F).

Paper A

Statistical Investigation of the User Effects on Mobile Terminal Antennas for 5G Applications
Igor Syrytsin, Shuai Zhang, Gert Frølund Pedersen, Kun Zhao, Thomas Bolin, and Zhinong Ying
Published in *IEEE Transactions on Antennas and Propagation*, Vol. 65, Issue 12, pp. 6596-6605, 2017.

Motivation

A lot of deep studies on user effect have already been conducted for the handset antennas at the sub-6GHz frequencies, but at the mm-wave frequencies only a few investigations to quantify the user blockage have been done so far. However, in the most of these studies the measurements have been conducted with a transmitter and a receiver in the indoor environment and with the users walking/standing between the two antennas. But no user effect assessment has been performed while the user is actually holding a mobile device in the hand. Because the APMS section has the necessary facilities to conduct such a measurement, it has been chosen, with a help from Sony Research Center Lund, to make a series of radiation pattern measurements with multiple users. This has been done in order to get statistical data for shadowing, coverage efficiency and body losses. Furthermore, at the moment of writing the paper, none of the specific metrics for the spatial body blockage characterization could be found in the literature.

Paper content

In this paper, the realistic mobile 5G phone mock-up from Sony has been provided for the measurement. A number of different antennas are located inside the mock-up. However, it has been chosen to measure a single notch antenna, as the antenna with an endfire radiation pattern would be most realistic candidate for usage in the modern phones with a high screen to body ratio. A sample of 12 users has been chosen from the master students and radiation pattern measurements have been performed in data and talk modes for two phone orientations. In the measurements, the users held the phone naturally but the distance between the mock-up and the user has been fixed. The radiation patterns and shadowing regions are also studied by using a novel metrics of shadowing antenna power ratio (SAPR) and shadowing isotropic antenna power ratio (SIAPR). It is found that a significant amount of power can propagate into the shadow of the user by creeping waves and diffractions. The result of the measurements campaign are processed and mean, variance, maximum and minimum values for the SAPR, body loss and coverage efficiency are presented.

Main results

First of all, it has been found that even without calibrating the results for the antenna miss-match losses the mean values of SAPR, body loss and coverage efficiency are vary insignificantly along the frequency range form 26.5 to 29.5 GHz. So in order to see more significant variations in user effects, a larger frequency span should be chosen for investigation in the future. In all measurements, a body loss is much lower than the body loss observed at the lower GSM/LTE frequencies (<6 GHz). A mean body loss of 3.2-4 dB is expected in talk mode, which is also similar to the data mode with the bottom antenna location. A body loss of 1 dB is expected in data mode with the top antenna location (pointing away from the user). The variation of the body loss between the users at 28 GHz is less than 2 dB, which is also much less than that of the conventional cellular bands below 3 GHz. The coverage efficiency is significantly reduced in talk mode, but only slightly affected in data mode because the user act as the efficient scatterer and numerous strong reflections are observed. A measure of shadowing power ratio has been proposed in this manuscript to characterize the shadowing region. The highest mean SAPR has been obtained from the measurements in the data mode with the antenna on the bottom of a device, which means that is will be the most critical position for the 5G phased antenna array. The measured values of coverage efficiency and body loss could be directly applied in the link simulations of 5G mm-wave system, however, one should notice that the results will only be valid for the antennas with endfire radiation patterns.

Paper B

User Effects on the Circular Polarization of 5G Mobile Terminal Antennas
Igor Syrytsin, Shuai Zhang, Gert Frølund Pedersen, Zhinong Ying
Published in *IEEE Transactions on Antennas and Propagation*, Vol. 66, Issue 9, pp. 4906-4911, 2018.

Motivation

Circular polarization have multiple advantages for making a communication link more reliable in highly mobile environments. Usually, the base station will have two linear orthogonal polarizations, but considerable polarization missmatch losses will occur when the orientation of the mobile device is unknown and pointing angles are not precise. Furthermore, it has been found that sometimes a specific environment or a user effect will change the polarization of the wave, so circular polarization would also be advantageous in this case. If the mobile device has a circular polarized antenna, then a constant polarization missmatch loss of 3 dB should be added to the link budget. Very few compact 5G mm-wave mobile antennas with circular polarization have been presented at the time of writing of the manuscript. Thus, it has been chosen to take some of the existing design guidelines from the low frequency antennas and apply them in the design of a circurlarly polarized5G mm-wave phased array. It is also much more challenging to make a planar circularly polarized antenna element with endfire radiation, but it is much needed for implementation in the common smartphones with the metal back and full case screen. Finally, the coverage efficiency is very general metric so there is a need for a more specific metric considering the polarization of the antenna.

Paper content

In this paper, a planar circular polarized antenna element with endfire radiation pattern and a single feeding point is proposed. A circurlarly polarized endfire radiation pattern is produced by the electric and magnetic dipoles, with electric fields normal to each other. The proposed antenna element is put in an array and multiple free space radiation properties (radiation pattern, maximum gain and Axial Ratio (AR)) are obtained from an FDTD simulation. Then, a novel metrics of circular polarized (CP) coverage efficiency and CP total scan pattern are proposed to characterize a spatial circular polarization performance of the antenna. A full-body human phantom made of skin tissue with average human dimensions is proposed and verified by radiation pattern measurements. The user effects on the CP performance of a mobile phased array were studied with the two defined parameters. The CP phased array is studied in the talk mode (according to CTIA standards) and in the data mode (with the CTIA hand and a homogeneous full-body phantom). The antenna array is placed at the bottom and the top locations on the mobile device. Top and bottom array locations are simulated and it has been found that both axial ratio bandwidth and beamwidth depend highly on the array location. Furthermore, results have been processed and presented in form of regular and CP coverage efficiency.

Main results

First, in this paper an antenna element with AR bandwidth of 4 GHz and AR beamwidth of around 50° is proposed. Which would mean that a phased array constructed from the proposed elements would have a maximum scan angle of 50° with a circular polarization at the main beam. Scanning the array to the larger angles will lead to deterioration in circular polarization performance. Next, user effects on a circular polarized phased array were studied for 5G mobile terminal applications. Two figures of merit have been introduced: the CP total scan pattern and CP coverage efficiency. Circular polarization is relatively more robust to user impact than linear polarization in some cases. For an optimal CP performance with user effects in the talk mode, a CP phased array should be placed at the bottom short edge ground plane location, while in the data mode, the top short edge location should be used. Thus, the two phased antenna arrays should be placed on the top and bottom edge of the mobile device for optimal CP antenna performance. This information would help significantly the 5G mm-wave mobile antenna designer, if the CP array is required for the specific mobile terminal application.

Paper C

User Impact on Phased and Switch Diversity Arrays in 5G Mobile Terminals
Authors Igor Syrytsin, Shuai Zhang, Gert Frølund Pedersen Published in the *IEEE Access*, Vol. 6, pp. 1616-1623, 2018.

Motivation

It is known that a phased array gives the best performance when operated in free space, but when user's hand and body is in the close proximity to the antenna elements then the array will not operate optimally. If one or multiple user's fingers block the antenna elements, then a phased antenna array will operate as an antenna array with nonuniform distance between elements, because the blocked elements would be totally inefficient. This will lead to the bigger gratin lobe and sidelobe level. Furthermore, it has been found both in paper A and B that when an antenna is pointing towards the user then most of the radiation will be blocked anyway. Thus, in theory a phased array will not increase the overall spatial performance of the system in respect to a single antenna when applied in the mobile device held by the user.

Paper content

In this paper, a linear mobile terminal phased array at 28 GHz with multiple scan angles is compared to a switch diversity antenna array at 28 GHz. In both cases the case of antenna beams are pointing at the user's body. In the simulation, each element of a simple monopole array can be driven independently, or all of the elements can be excited simultaneously with a specific signal phase at each element's input. During the investigation, four different scan angles (28, 58, 90, and 128 degree) of the phased array are considered. Both coverage efficiency and SAPR values are calculated from the simulations and measurements in free space and with a standing user in the data mode, which includes both body blockage and user hand effects. Finally the free space results are compared to the results to the user measurements with a phased array and different scan angles and a switch diversity array, where each element operating independently.

Main results

In this paper, it is found that the array scan angle higher than 90° is not necessary when the main beam is pointing directly towards the user, because the user body will contribute to the total radiation at larger angles by creeping waves and diffractions. For the linear phased antenna arrays on the edge of the mobile device ground plane it can be concluded that in order to achieve the highest coverage efficiency and lowest user shadowing it is mostly beneficial to use a phased array instead of a switch diversity array. However, if the losses of the phase shifters and the feeding network in the real phased array are higher than 5 dB, then a switch diversity array would be more effective, which will also decrease the complexity of a system.

Paper D

Compact Quad-Mode Planar Phased Array with Wideband for 5G Mobile Terminals

Igor Syrytsin, Shuai Zhang, Gert Frølund Pedersen, and and Art Morris
Published in the *IEEE Transactions on Antennas and Propagation*, Vol. 66, Issue 9, pp. 4648-4657, 2018.

Motivation

A wide range of frequencies will be used for the 5G mm-wave communication. However, most important 5G mm-wave mobile bands are 24.25 to 27.5 GHz and 37 – 43.5 GHz. Thus, for a mobile device it is important to cover both of these bands while still maintaining small form factor. Furthermore, new mobile devices will have extremely large screen-to-body ratios, while the selfie camera could be hidden, when not in use, so the ground plane clearance requirements will become more and more strict with time. Moreover, most of the mobile devices are built of aluminum with the design and mechanical stability considerations in mind. Thus, it is important to have an antenna element with endfire radiation characteristics which is less affected by a big screen and a metal case. It can clearly be seen that there is a need for a novel planar small wideband or dual band antenna element which could be used in 5G mm-wave mobile devices.

Paper content

The manuscript presents the design of the proposed quad mode element and explains how such element can sustain a similar embedded radiation pattern in all four modes when in array of more than 3 elements. Furthermore, an example of a feeding structure for such element is presented. The feeding is based on the coupled stripline to coaxial cable transition in order to provide differential feeding for the antenna. Finally the antenna array is measured in the anechoic chamber in free space and the performance along the operation frequency range of the antenna in assessed. The coverage efficiency curves are presented for each frequency and statistics are computed based on the measurements and simulations.

Main results

In this paper a quad-mode endfire planar phased antenna array with wide scan angle and 1.2 mm clearance is proposed for 5G mobile terminals with big screen-to-body ratio. The proposed antenna have over 8 GHz of impedance bandwidth. Is is suggested to combine a multi-mode array element with different radiation patterns for each mode into a phased antenna array. In the array, similar and wide embedded radiation patterns are obtained for the all four modes by suppressing the surface current at the edges of the element. Furthermore, a compact coaxial cable to differential stripline transition which utilizes only MMPX connector and vias is designed in this work. The total scan pattern and coverage efficiency of the measured and simulated phased array antenna are calculated in the range from 25 to 33 GHz, and a good agreement between measured and simulated results is observed. The mean coverage efficiency along the frequency range is very similar, but minor difference in variance of coverage efficiency is observed in the measurements. The coverage efficiency of around 50 % for the threshold gain of 5 dBi is achieved in the chosen frequency range. The guidelines on how the proposed element can be constructed are presented in this work. This will help a 5G antenna engineer to adjust the resonant frequency of the different modes to meet a specific bandwidth requirement.

Paper E

User Shadowing Suppression for 5G mm-wave Mobile Terminal Antennas
Igor Syrytsin, Shuai Zhang, Gert Frølund Pedersen, and and Art Morris
Published in the *IEEE Transactions on Antennas and Propagation*, Vol. 67, Issue 6,

pp. 4162-4172, 2019.

Motivation

In papers A, B, C and others it has been already shown that user effects do indeed affect the spatial performance of the antenna. Furthermore, not only the maximum gain but also the spatial radiation intensity distribution is affected by the user blockage. But, it has also been noticed that a user will not totally block the radiation, and in some cases the waves will propagate behind the user's back by means of creeping waves and diffractions. User effect mostly depends on the antenna location on the ground plane and main beam direction. In order to make a 5G mm-wave phased mobile array design robust to used effects the guidelines on the best antenna position would be crucial.

Paper content

First, the assessment of the phased sub-array position is conducted. This is done by making multiple FDTD simulations with user in talk mode (according to the CTIA standards) and data and dual-hand modes with a full body phantom (presented in paper B). A structure, consisting of 40 Vivaldi and 32 slot antennas, distributed around the four edges of the ground plane is simulated in CST Microwave studio with the full-body phantom in talk and data modes. Coverage efficiency is used is used as a metric for the determining the best position for a 4-element sub-array. After the best positions for a sub-array is found, it has been chosen to make four sub-arrays and place them in the proposed places to investigate the performance by means measurement with the real human. An SIW planar lens switched beam array is proposed and measured with the user in similar way as the simulated vivaldi-slot structure. It has been shown that four sub-arrays positioned according to the guidelines, give a performance comparable to a performance of multiple sub-arrays located all around all edges of the ground plane. Finally, two configurations of sub-arrays placed diagonally on the opposite corners of the mobile device were investigated and compared to each other and to the setup with the four sub-arrays.

Main results

In this paper, it has been proven that a corner positions on the handset chassis yield the best performance for the 5G mm-wave array system in terms of spatial coverage when user effects are considered. To prove that claim, a prototype of a 5G mm-wave antenna system was constructed. An SIW lens with MMPX connectors and was compared to the more general case. It has been shown that the method proposed in this paper can be used as general guideline for the 5G phased array construction. Furthermore, two diagonally placed sub-arrays yields similar performance as four sub-arrays if only left or right-handed gestures are considered. The information in this paper gives the guidelines on the 5G mobile sub-array position for the 5G antenna engineers. These guidelines together with the information from paper C can be used to optimize the system which is robust towards the user influence.

Paper F

Characterization and Modeling of the User Blockage for 5G
Peiye Liu, Igor Syrytsin, Shuai Zhang, Jesper Ødum Nielsen, and Gert Frølund Pedersen
Has been submitted to *IEEE Transactions on Antennas and Propagation*, 2019.

Motivation

From the earlier papers it can clearly be seen that user effects will vary depending on the user's gesture, antenna location and main beam direction. However, determining those critical user gestures is a crucial step towards designing a realistic model of the user shadowing. The right and accurate spatial model for the user shadowing will be very helpful to the 5G communication system designers and ray tracing simulations. However, the proposed model should both be flexible and describe the average user impact.

Paper content

First, the most critical user gestures are determined in this paper. This has been done by choosing data and talk mode gestures as a starting point and then moving the mobile device in the chosen direction. It has been decided to see how the mobile device height, distance from the user's body, angle, displacement, etc. affect the user blockage. This has been done by means of radiation pattern measurements in the anechoic chamber with the live user. The SAPR and shadowing CDF have been computed and compared for different gestures. Furthermore, the de-embedding of the user shadowing pattern has been done for three different antennas using the free space radiation patterns. Next, the measurement of the population sample of 18 male and female subjects has been conducted. Mean radiation patterns have been computed and presented. Finally, the model of user shadowing pattern which is based on the measurement campaign with the 18 users is presented.

Main results

In this work, it has been found that the most critical user gestures considering the user shadowing are the distance between the antenna and the user and the antenna height. Furthermore, it has been found that user shadowing intensity can be successfully de-embedded from the total radiation pattern and do not depend on the antenna type with a given polarization. New metrics of shadowing CDF and USIR are also defined in this manuscript, which gives the antenna community more options for user effects description. A stochastic 3D user shadowing model is presented which can be used in the frequency range 28 GHz ± 6 GHz. The user shadowing model is based on measurements with 18 subjects of different heights and gender and modeled as a stochastic process which follows the Gaussian distribution in each of the three defined spatial regions of the model. However, the presented model is not 100% perfect and only as good as the population sample, which is significantly better than that in paper A.

Conclusion

The main focus of the thesis is to assess, characterize and model all the different user effects on the 5G mm-wave antennas in the mobile terminals. However, in the each of the separate user effect studies a specific novel antenna structure has been designed. Multiple novel metrics have been presented in this thesis, which include shadowing antenna power ratio (SAPR), shadowing isotropic antenna power ratio (SIAPR), circularly polarized (CP) total scan pattern and CP coverage efficiency, shadowing CDF and USIR. With these novel metrics the user shadowing can be efficiently characterized. Multiple 5G antennas have been presented in this thesis, such as CP compact endfire array, quad mode wideband array with extremely small clearance, compact lens antenna array with H-plane horns as radiators, and others. Two big measurement campaigns including multiple users and different antennas have been conducted. One of those campaigns resulted in a conclusion that the body loss at 5G mm-wave bands is much smaller than that at the sub-6 GHz frequencies. Another measurement campaign gave a basis for the proposed stochastic spatial user shadowing model, which could be directly used as a radiation pattern in a 5G mm-wave link simulator. It has been also found that in some cases a circularly polarized antenna are more robust to user effects than linearly polarized antenna. Furthermore, using a phased array is not always beneficial in order to obtain the best spatial coverage and a simple switch diversity array can be equally efficient in some cases. A full-body homogeneous user phantom has been proposed in this thesis, too. The dimensions of the phantom are based on the mean male human dimensions and the accuracy of the phantom has been verified by the measurement and found to be acceptable. However the effects of clothing, sweat, hair, and other have not been investigated yet. It has been shown that the new mobile phones with a high screen-to-body ratios can still accommodate a 5G mm-wave phased array if the element with very small clearance is used. Moreover, based on the guidelines given in this thesis a 5G mobile mm-wave antenna array could be placed in the most efficient locations of the chassis and thus, always guarantee the weakest user effects. For even better efficiency, multiple phased sub-arrays could be placed around the mobile device to take into account left and right-handed users.

References

[1] T. S. Rappaport, S. Sun, R. Mayzus, H. Zhao, Y. Azar, K. Wang, G. N. Wong, J. K. Schulz, M. Samimi, and F. Gutierrez, “Millimeter wave mobile communications for 5G cellular: It will work!,” *IEEE Access*, vol. 1, pp. 335–349, 2013.

[2] J. Lee, E. Tejedor, K. Ranta-aho, H. Wang, K. T. Lee, E. Semaan, E. Mohyeldin, J. Song, C. Bergljung, and S. Jung, “Spectrum for 5G: Global status, challenges, and enabling technologies,” *IEEE Comm. Mag.*, vol. 56, pp. 12–18, Mar. 2018.

[3] W. Roh, J. Y. Seol, J. Park, B. Lee, J. Lee, Y. Kim, J. Cho, K. Cheun, and F. Aryanfar, “Millimeter-wave beamforming as an enabling technology for 5G cellular communications: theoretical feasibility and prototype results,” *IEEE Commun. Mag.*, vol. 52, pp. 106–113, February 2014.

[4] W. Hong, S. T. Ko, Y. Lee, and K. H. Baek, “Multi-polarized antenna array configuration for mmwave 5G mobile terminals,” *2015 International Workshop on Antenna Technology (iWAT)*, pp. 60–61, Mar. 2015.

[5] N. Ojaroudiparchin, M. Shen, and G. F. Pedersen, “Design of vivaldi antenna array with end-fire beam steering function for 5G mobile terminals,” *2015 23rd Telecommunications Forum Telfor (TELFOR)*, pp. 587–590, 2015.

[6] I. Syrytsin, S. Zhang, G. F. Pedersen, and A. Morris, “Compact quad-mode planar phased array with wideband for 5G mobile terminals,” *IEEE Trans. Antennas Propag.*, 2018,(in press).

[7] W. Hong, K. Baek, Y. Lee, and Y. G. Kim, “Design and analysis of a low-profile 28 GHz beam steering antenna solution for future 5G cellular applications,” *Microwave Symposium (IMS), 2014 IEEE MTT-S International*, pp. 1–4, Jun. 2014.

[8] R. Hussain, A. T. Alreshaid, S. K. Podilchak, and M. S. Sharawi, “Compact 4G MIMO antenna integrated with a 5G array for current and future mobile handsets,” *IET Microwaves, Antennas & Propagation*, vol. 11, no. 2, pp. 271–279, 2017.

[9] N. Ojaroudiparchin, M. Shen, S. Zhang, and G. F. Pedersen, “A switchable 3-D-coverage-phased array antenna package for 5G mobile terminals,” *IEEE Antennas Wireless Propag. Lett.*, vol. 15, pp. 1747–1750, 2016.

[10] S. Zhang, X. Chen, I. Syrytsin, and G. F. Pedersen, “A Planar Switchable 3D-Coverage Phased Array Antenna and Its User Effects for 28 GHz Mobile Terminal Applications,” *IEEE Trans. Antennas Propag.*, vol. 65, pp. 6413–6421, Dec. 2017.

[11] N. Ojaroudiparchin, M. Shen, and G. F. Pedersen, “Wide-scan phased array antenna fed by coax-to-microstriplines for 5G cell phones,” *2016 21st International Conference on Microwave, Radar and Wireless Communications (MIKON)*, pp. 1–4, 2016.

[12] N. O. Parchin, M. Shen, and G. F. Pedersen, “End-fire phased array 5G antenna design using leaf-shaped bow-tie elements for 28/38 GHz MIMO applications,” *2016 IEEE International Conference on Ubiquitous Wireless Broadband (ICUWB)*, pp. 1–4, 2016.

[13] S. Zhang, A. A. Glazunov, Z. Ying, and S. He, “Reduction of the envelope correlation coefficient with improved total efficiency for mobile lte mimo antenna arrays: Mutual scattering mode,” *IEEE Transactions on Antennas and Propagation*, vol. 61, pp. 3280–3291, June 2013.

[14] S. Zhang, K. Zhao, Z. Ying, and S. He, “Adaptive quad-element multi-wideband antenna array for user-effective lte mimo mobile terminals,” *IEEE Transactions on Antennas and Propagation*, vol. 61, pp. 4275–4283, Aug 2013.

[15] K. Zhao, S. Zhang, K. Ishimiya, Z. Ying, and S. He, “Body-insensitive multimode mimo terminal antenna of double-ring structure,” *IEEE Transactions on Antennas and Propagation*, vol. 63, pp. 1925–1936, May 2015.

[16] M. M. Samadi Taheri, A. Abdipour, S. Zhang, and G. F. Pedersen, “Integrated millimeter-wave wideband end-fire 5g beam steerable array and low-frequency 4g lte antenna in mobile terminals,” *IEEE Transactions on Vehicular Technology*, vol. 68, pp. 4042–4046, April 2019.

[17] B. Yu, K. Yang, C. Y. D. Sim, and G. Yang, “A novel 28 GHz beam steering array for 5G mobile device with metallic casing application,” *IEEE Trans. Antennas Propag.*, vol. 66, pp. 462–466, Jan. 2018.

[18] R. Rodriguez-Cano, S. Zhang, K. Zhao, and G. F. Pedersen, “Reduction of main beam-blockage in an integrated 5g array with a metal-frame antenna,” *IEEE Transactions on Antennas and Propagation*, vol. 67, pp. 3161–3170, May 2019.

[19] M. U. Rehman, X. Chen, C. G. Parini, and Z. Ying, “Evaluation of a statistical model for the characterization of multipath affecting mobile terminal GPS antennas in sub-urban areas,” *IEEE Trans. Antennas Propag.*, vol. 60, pp. 1084–1094, Feb. 2012.

[20] J. Helander, K. Zhao, Z. Ying, and D. Sjöberg, “Performance analysis of millimeter-wave phased array antennas in cellular handsets,” *IEEE Antenna Wireless Propag. Lett.*, vol. 15, pp. 504–507, 2016.

[21] C. Di Paola, K. Zhao, S. Zhang, and G. F. Pedersen, “Siw multibeam antenna array at 30 ghz for 5g mobile devices,” *IEEE Access*, vol. 7, pp. 73157–73164, 2019.

[22] Y. J. Cheng and Y. Fan, “Millimeter-wave miniaturized substrate integrated multibeam antenna,” *IEEE Trans. Antennas Propag.*, vol. 59, pp. 4840–4844, Dec 2011.

[23] L. Wang, M. Garcia-Vigueras, M. Alvarez-Folgueiras, and J. R. Mosig, “Wideband H-plane dielectric horn antenna,” *IET Microwaves, Antennas Propagation*, vol. 11, no. 12, pp. 1695–1701, 2017.

[24] W. Hong, K. H. Baek, Y. Lee, Y. Kim, and S. T. Ko, “Study and prototyping of practically large-scale mmwave antenna systems for 5g cellular devices,” *IEEE Communications Magazine*, vol. 52, pp. 63–69, September 2014.

[25] O. P. Gandhi and A. Riazi, “Absorption of millimeter waves by human beings and its biological implications,” *IEEE Transactions on Microwave Theory and Techniques*, vol. 34, pp. 228–235, Feb 1986.

[26] J. B. Andersen, J. O. Nielsen, and G. F. Pedersen, “Absorption related to handheld devices in data mode,” *IEEE Transactions on Electromagnetic Compatibility*, vol. 58, pp. 47–53, Feb 2016.

[27] M. Pelosi, O. Franek, M. B. Knudsen, G. F. Pedersen, and J. B. Andersen, “Antenna proximity effects for talk and data modes in mobile phones,” *IEEE Antennas and Propagation Magazine*, vol. 52, pp. 15–27, June 2010.

[28] J. Toftgard, S. N. Hornsleth, and J. B. Andersen, “Effects on portable antennas of the presence of a person,” *IEEE Transactions on Antennas and Propagation*, vol. 41, pp. 739–746, Jun 1993.

[29] J. O. Nielsen and G. F. Pedersen, “Mobile handset performance evaluation using radiation pattern measurements,” *IEEE Transactions on Antennas and Propagation*, vol. 54, pp. 2154–2165, July 2006.

[30] J. O. Nielsen, B. Yanakiev, I. B. Bonev, M. Christensen, G. F. Pedersen, C. Luxey, A. Dialled, and I. Dicmm, “User influence on the mean effective gain

for data mode operation of mobile handsets," in *2012 6th European Conference on Antennas and Propagation (EUCAP)*, pp. 2759–2763, March 2012.

[31] J. Krogerus, J. Toivanen, C. Icheln, and P. Vainikainen, "Effect of the human body on total radiated power and the 3-d radiation pattern of mobile handsets," *IEEE Transactions on Instrumentation and Measurement*, vol. 56, pp. 2375–2385, Dec 2007.

[32] K. R. Boyle, "The performance of gsm 900 antennas in the presence of people and phantoms," in *Antennas and Propagation, 2003. (ICAP 2003). Twelfth International Conference on (Conf. Publ. No. 491)*, vol. 1, pp. 35–38 vol.1, March 2003.

[33] J. Ilvonen, O. Kivekas, J. Holopainen, R. Valkonen, K. Rasilainen, and P. Vainikainen, "Mobile terminal antenna performance with the user's hand: Effect of antenna dimensioning and location," *IEEE Antennas and Wireless Propagation Letters*, vol. 10, pp. 772–775, 2011.

[34] J. Holopainen, O. Kivekas, J. Ilvonen, R. Valkonen, C. Icheln, and P. Vainikainen, "Effect of the user's hands on the operation of lower uhf-band mobile terminal antennas: Focus on digital television receiver," *IEEE Transactions on Electromagnetic Compatibility*, vol. 53, pp. 831–841, Aug 2011.

[35] T. Wu, T. S. Rappaport, and C. M. Collins, "The human body and millimeter-wave wireless communication systems: Interactions and implications," in *2015 IEEE International Conference on Communications (ICC)*, pp. 2423–2429, June 2015.

[36] 3GPP, "Technical specification group radio access network; study on channel model for frequencies from 0.5 to 100 ghz," *document TR 38.901*, Jul. 2017.

[37] I. Syrytsin, S. Zhang, G. F. Pedersen, K. Zhao, T. Bolin, and Z. Ying, "Statistical investigation of the user effects on mobile terminal antennas for 5G applications," *IEEE Trans. Antennas Propag.*, vol. 65, pp. 6596–6605, Dec 2017.

[38] K. Zhao, J. Helander, D. Sjöberg, S. He, T. Bolin, and Z. Ying, "User body effect on phased array in user equipment for the 5G mmwave communication system," *IEEE Antenna Wireless Propag. Lett.*, vol. 16, pp. 1847–1850, 2017.

[39] R. Rodríguez-Cano, S. Zhang, K. Zhao, and G. F. Pedersen, "User body interaction of 5g switchable antenna system for mobile terminals at 28 ghz," in *2019 13th European Conference on Antennas and Propagation (EuCAP)*, pp. 1–4, March 2019.

[40] V. Raghavan, L. Akhoondzadeh-Asl, V. Podshivalov, J. Hulten, M. A. Tassoudji, O. H. Koymen, A. Sampath, and J. Li, "Statistical blockage modeling and robustness of beamforming in millimeter-wave systems," *IEEE Transactions on Microwave Theory and Techniques*, pp. 1–15, 2019.

[41] C. A. Balanis, *ANTENNA THEORY ANALYSIS AND DESIGN*. John Wiley & Sons, 2005.

[42] J. L. Volakis, *Antenna Engineering Handbook*. McGraw-Hill, 2007.

[43] N. K. Nikolova, "Lecture notes on polarization and related antenna parameters," July 2003.

[44] T. A. Milligan, *Modern antenna design*. John Wiley & Sons, 2005.

[45] D. Pozar, *Microwave Engineering, 4th Edition*. Wiley Global Education, 2011.

[46] P. J. Bevelacqua, "Antenna-theory." `http://www.antenna-theory.com`.

[47] S. Zhang, G. H. Huff, J. Feng, and J. T. Bernhard, "A pattern reconfigurable microstrip parasitic array," *IEEE TRANSACTIONS ON ANTENNAS AND PROPAGATION, VOL. 52, NO. 10*, OCTOBER 2004.

[48] M. Jusoh, T. Aboufoul, T. Sabapathy, A. Alomainy, and M. R. Kamarudin, "Pattern-reconfigurable microstrip patch antenna with multidirectional beam for wimax application," *IEEE ANTENNAS AND WIRELESS PROPAGATION LETTERS, VOL. 13*, 2014.

[49] I. B. Trad, J. M. Floc'h, H. Rmili, M. Drissi, and F. Choubani, "Design of reconfigurable radiation pattern dipole antenna with director and reflector elements for telecommunication systems," *Loughborough Antennas & Propagation Conference*, November 2013.

[50] W. Rotman and R. Turner, "Wide-angle microwave lens for line source applications," *IEEE Transactions on Antennas and Propagation*, vol. 11, pp. 623–632, November 1963.

Part II

Papers

Paper A

Statistical Investigation of the User Effects on Mobile Terminal Antennas for 5G Applications

Igor Syrytsin, Shuai Zhang, Gert Frølund Pedersen, Kun Zhao,
Thomas Bolin, and Zhinong Ying

The paper has been published in:
IEEE Transactions on Antennas and Propagation, Vol. 65, Issue 12, pp. 6596-6605, 2017.

Abstract

In this paper the user effects on mobile terminal antennas at 28 GHz are statistically investigated with the parameters of body loss, coverage efficiency and power in the shadow. The data are obtained from the measurements of 12 users in data and talk modes, with the antenna placed on the top and bottom of the chassis. In the measurements, the users hold the phone naturally. The radiation patterns and shadowing regions are also studied. It is found that a significant amount of power can propagate into the shadow of the user by creeping waves and diffractions. A new metric is defined to characterize this phenomenon. A mean body loss of 3.2-4 dB is expected in talk mode, which is also similar to the data mode with the bottom antenna. A body loss of 1 dB is expected in data mode with the top antenna location. The variation of the body loss between the users at 28 GHz is less than 2 dB, which is much smaller than that of the conventional cellular bands below 3 GHz. The coverage efficiency is significantly reduced in talk mode, but only slightly affected in data mode.

DOI:

https://ieeexplore.ieee.org/document/7876785

Statistical Investigation of the User Effects on Mobile Terminal Antennas for 5G Applications

Igor Syrytsin, Shuai Zhang, Gert Frølund Pedersen, *Senior Member, IEEE*, Kun Zhao, Thomas Bolin, Zhinong Ying, *Senior Member, IEEE*

***Abstract*—In this paper the user effects on mobile terminal antennas at 28 GHz are statistically investigated with the parameters of body loss, coverage efficiency and power in the shadow. The data are obtained from the measurements of 12 users in data and talk modes, with the antenna placed on the top and bottom of the chassis. In the measurements, the users hold the phone naturally. The radiation patterns and shadowing regions are also studied. It is found that a significant amount of power can propagate into the shadow of the user by creeping waves and diffractions. A new metric is defined to characterize this phenomenon. A mean body loss of 3.2-4 dB is expected in talk mode, which is also similar to the data mode with the bottom antenna. A body loss of 1 dB is expected in data mode with the top antenna location. The variation of the body loss between the users at 28 GHz is less than 2 dB, which is much smaller than that of the conventional cellular bands below 3 GHz. The coverage efficiency is significantly reduced in talk mode, but only slightly affected in data mode.**

***Index Terms*—User effects, antennas, mobile handset, radiation patterns, body loss, coverage efficiency, 5G applications.**

I. INTRODUCTION

RECENTLY communications at the millimeter wave frequencies have become more relevant, because of the design considerations for the upcoming 5G communication systems [1]. It has been considered to use beamforming at both the base and mobile stations to overcome the path loss at the high frequencies, as described in [2]. The 28 GHz band is one of the candidate bands for the upcoming 5G communication systems.

Different phased antenna array systems have already been designed to operate at this frequency in [3], [4]. An antenna for the next generation should be able to achieve high EIRP and at the same time high antenna coverage with low power consumption [5]. Furthermore, the user effects should not be neglected when designing an antenna for the mobile terminal [5]. Interactions between the human body and millimeter-wave devices at 60 GHz have been studied in [6]. In the [7] absorption of the millimeter waves by humans has been studied. However, for the 5G communication systems, it is interesting to study interactions between a mobile terminal antenna and a human head and hand. Early investigations in [8] suggested that a resonance frequency of the antenna tunes down when used by a person. Big amount of power will be lost in the human hand and head and a significant change in the shape of a radiation pattern will occur. At the frequencies from 0.5 to 3 GHz, the absorption due to the user presence has been studied in [9]. The performance of the mobile handsets has been evaluated using mean effective gain (MEG) in [10] and [11]. Absorption and missmatch losses of the four antennas at 900 and 1800 MHz has been investigated in [12]. In [13] the total and missmatch efficiency and MEG of the GSM 900 antennas have been investigated. In [14] it has been concluded that 8 to 13 persons are required to obtain a reasonable estimate of the body loss mean and variation. The effects of the human body on the total radiated power (TRP) and the radiation pattern has been studied in [15] by using phantoms and humans. The impact of the user's hand/hands on the mobile antenna performance has been studied in [16] and [17], where it has been concluded that the position and height of the antenna and position of the fingers on the mobile terminal play a major role in the mobile antenna performance. The effect of the user on the coverage and the radiation pattern of a phased antenna array has been studied in [18]. However the statistical investigation of the user impact or coverage efficiency of the mobile antenna at 28 GHz has not been done yet.

This paper will focus on the investigation of the user effects on the performance of the mobile antenna at 28 GHz by measuring the mobile device prototype. The prototype includes a battery and a screen. Body loss, coverage efficiency, and shadowing effects will be studied by measuring the antenna prototype in the anechoic chamber with a user in data and talk modes. The chosen parameters will be presented in terms of the variation and mean values of the measurements on the 12 users. A new parameter will be introduced to characterize the shadowing area, which can be used to investigate how much energy can propagate around the user by creeping waves and diffractions. The coverage efficiency of the antenna is also evaluated.

II. METHODS

A. Measurement Setup

In this paper, it has been chosen to use a prototype, provided by Sony Mobile, for all of the measurements. The front and the back views of the Sony prototype are shown in Fig. 1. The prototype has 10 antennas built in it. The 10 antennas are combined into two groups of the 5 antennas. Groups are

---

This work was supported by the InnovationsFonden project of RANGE.(Corresponding author: Shuai Zhang).

Igor Syrytsin, Shuai Zhang, and Gert Frølund Pedersen are with the Antennas, Propagation and Radio Networking section at the Department of Electronic Systems, Aalborg University, Denmark (email: {igs,sz,gfp}@es.aau.dk).

Kun Zhao is with KTH-Royal Institute of Technology, Stockholm, Sweden.

Thomas Bolin and Zhinong Ying are with the Corporate Technology Office, Sony Mobile Communication AB, Lund, Sweden.

located on the left and the right side of the phone prototype and mirrored in respect to the center of the prototype. All of the antennas have a center frequency at 28 GHz and a −10 dB bandwidth of at least 2 GHz. A screen and a battery are included in the prototype to further investigate how the antenna will perform in the real mobile device. In this paper, only one antenna will be used throughout all of the measurements. The chosen antenna is located on the right side of the prototype, as shown in Fig. 1(a). The antenna used in the measurements consists of the multiple slots located along an edge of the ground plane with a dielectric layer as shown in Fig. 2. The antenna is configured to resonate at a chosen frequency by excitation of one of the slots by the stripline on the dielectric layer. The chosen antenna geometry and applications are described in the detail in [19].

The prototype measured in the free space is shown in Fig. 3(a). The chosen notch antenna has a broad endfire radiation pattern in the direction of z-axis, as shown in Fig. 3(b). In Fig. 3(c) the polar plot of the radiation pattern in yz-plane at the frequency of 28 GHz is shown. Furthermore, there is also a little more radiation in the –y axis direction (screen direction) than in the +y axis direction, where the screen can support surface waves at the chosen frequency range.

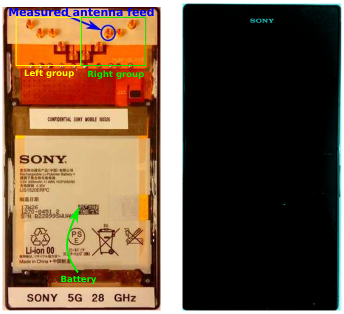

(a) (b)

Fig. 1. Sony prototype overview: (a) back and (b) front.

For the measurements with the user a safety is added to the measurement setup, thus chosen measurement system is unable to measure 14° on the top of the coordinate system. The elevation cut of the measurement system is shown in Fig. 4. The 40° on the bottom can not be reached because of the rotating podium size limitations. The 14° on the top in θ is chosen as a starting point to be able to fix persons under test to the crane on the top with a safety rope. The "holes" in the measurement system are shown in red color and the parts where the system is able to measure are shown in green color. The "holes" will induce errors on the TRP calculation accuracy. However, those errors are acceptable, because the total area in the "holes" is much smaller than the area where the system is able to measure. From the solid angle view, the number of steradians in the holes equals to 1.6566 sr in comparison to the rest of the measurement system: $4\pi - 1.6566 = 10.9097$ sr. The solid angle in the holes is 13.13 % of the whole sphere. The solid angle of the top hole is only 0.1866 sr, which corresponds to 1.48 % of the whole sphere. Furthermore, the antenna is oriented in such way so the strongest part of the radiation pattern is located outside of the "holes". By doing so it has been ensured that the power missed in the holes is very small in comparison to the rest of the measured power. The rotary positioner with the chair is placed at $\theta = 180°$, which will limit the amount of the energy propagating towards the bottom of the measurement setup.

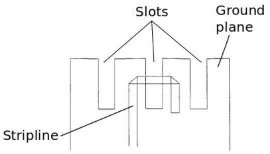

Fig. 2. Geometry of the measured antenna [19].

It has been chosen to measure the mobile prototype with the influence of a user in the four positions:

- Mobile in talk mode – antenna located on the top, as shown in Fig. 5(a).
- Mobile in talk mode – antenna located on the bottom, as shown in Fig. 5(b).
- Mobile in data mode – antenna located on the top, as shown in Fig. 5(c).
- Mobile in data mode – antenna located on the bottom, as shown in Fig. 5(d).

In all of the measurements, a user has been told to held the phone naturally. However, in the data mode, the requirement was to hold the phone horizontally and the distance between the user and the phone has been adjusted to be around 30 cm. This means that the chosen experimental setup represents the worst case scenario because the grip of the user has not been controlled. It has also been known for a long time, that a user is usually holding a phone by utilizing one of the two most common grips: firm and soft grips [12], which for the higher frequencies will introduce variation in the shadowing from the user's hand.

B. Measures

Measures of the body loss and coverage efficiency are used in this paper to evaluate the results obtained by the measurement campaign. Furthermore, this paper will focus on investigation of the shadowing caused by the person presence in the measurement setup. The new metric of shadowing power ratio will be introduced later in the paper to describe the amount of power that has propagated around the user.

To find the body loss it is important to calculate the total radiated power of the antenna. The equation for the approximate total radiated power can be written as [9]:

$$P_{rad} = \Delta\phi\Delta\theta \sum_{\theta_{min}}^{\theta_{max}} \sum_{\phi_{min}}^{\phi_{max}} (P_V(\theta,\phi) + P_H(\theta,\phi)) \cdot sin(\theta) \qquad (1)$$

where:

- $\Delta\phi$ is a sampling step in ϕ, in the chosen setup the step equals to the 2°
- $\Delta\theta$ is a sampling step in θ, in the chosen setup the step equals to the 14°

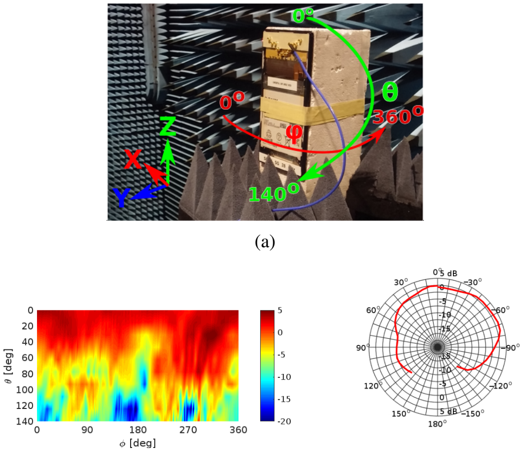

(a)

(b) (c)

Fig. 3. (a) the picture of the prototype in free space, (b) and (c) are the radiation pattern of the chosen antenna.

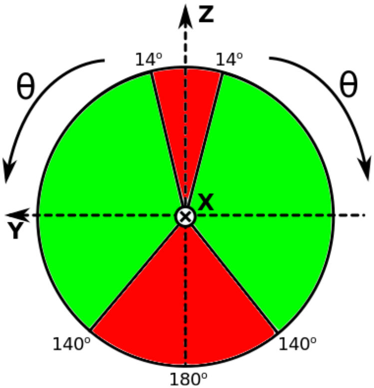

Fig. 4. The elevation cut of the measurement system.

- ϕ_{min} and ϕ_{max} are minimum and maximum angles, which are respectively defined to the 0° and 360°
- θ_{min} and θ_{max} are minimum and maximum angles, which are respectively defined to the 14° and 140°
- P_V and P_H are the power components received by the probe antenna in vertical and horizontal polarizations.

The body loss is defined in this paper as:

$$L_{body} = \frac{\eta_{free}}{\eta_{user}} \tag{2}$$

where η_{free} and η_{user} are the antenna total efficiency with and without the user.

The antenna impedance mismatch due to the user effects has been checked carefully before the measurement campaign. The reflection coefficient is always lower than -10 dB in the frequency range from 27 to 29 GHz in all the user cases. Therefore, the return loss of the cm-wave antenna is much less sensitive to the user effects than that of the low frequency antennas ($<$ 6 GHz). The body loss at the cm-wave frequencies mainly comes from the shadowing and absorption losses instead of antenna detuning. The mismatching losses of the antenna are neglected in this investigation.

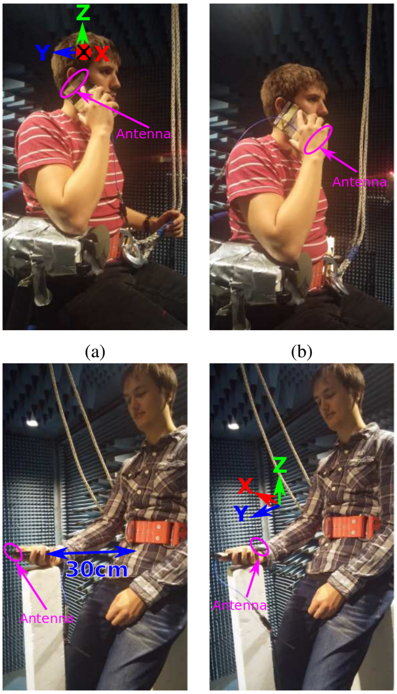

(a) (b)

(c) (d)

Fig. 5. The overview of the measurement setup with the user in (a) talk mode – antenna on top, (b) talk mode – antenna on bottom, (c) data mode – antenna on top, (d) data mode – antenna on bottom.

The coverage efficiency can be defined as: [20]

$$\eta_c = \frac{\text{Coverage solid angle}}{\text{Maximum solid angle}} \tag{3}$$

where the maximum solid angle is chosen to the 4π steradians (whole space).

C. Measurement Sample

In this measurement campaign, 12 users have been measured. However, only 11 measurements has been used for the characterization of the data mode with the antenna on top of the device as the one of measurements has provided incorrect results. All of the persons in this study are males and has been chosen from the university students under 30 years old. It has been chosen to measure 12 users because, as described in [14], this number of users is enough to provide the reliable statistical data about the variation and the mean of the body loss. The histograms over the heights and weights of the users are shown in Fig. 6(a) and Fig. 6(b), respectively. It can be noticed that the relative variation in the user weight is higher than the variation the user height. A big group of the people used in the measurements is over 180 cm high.

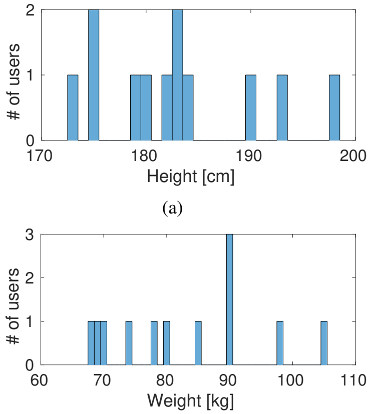

(a)

(b)

Fig. 6. The histogram of the (a) users' heights and (b) users' weights.

The photos of all the measured users in the data mode are shown in Fig. 7. The pictures give more insight on the shape of the users and gestures used.

III. Experimental Results

In this section the results of the measurement campaign will be presented.

A. Radiation Pattern

The 3D radiation patterns of the antenna in all the four measurement setups are plotted in Fig. 8. It can be seen that the radiation patterns have similarities to the measured patterns in [18], but the position of the antenna makes a big difference on the radiation pattern shape. In the talk mode, the radiation pattern is mainly distorted by the user's head. In the data mode, the shadowing from the user's body is significant, particularly when the main beam of the antenna is pointed towards the user.

In Fig. 8(a) the radiation pattern of the antenna with the user in talk mode and the antenna located on the top is shown. The shadowing area spans 126° in θ and 150° in ϕ. The head is very close to the antenna, and thus the shadowing area is big. However, by exciting surface waves on the user's skin, the antenna can still radiate in the region from $\phi = 100°$ to $190°$.

In Fig. 8(b) the radiation pattern of the phone in the talk mode with the antenna on the bottom is shown. In comparison to the radiation pattern in Fig. 8(a) the pattern does not look smooth because of the waves propagating through the finger openings of the hand. The head has less impact on the antenna radiation pattern due to the larger antenna-head distance than placing the antenna on the top. Furthermore, in this position, the user‘s palm covers directly over the antenna. It means that there is only a small window where the antenna can radiate ($\phi = 20°$ to $120°$), because the user blocks the radiation pattern either by the palm or by the head. The radiation pattern is mainly supported by the scattering from the user's hand, fingers, and head.

Fig. 7. All of the measured users in the data mode.

In Fig. 8(c) the radiation pattern of the antenna on the top in data mode is shown. The main beam of the radiation pattern at 90° ϕ is pointing away from the user, and thus it is nearly not distorted by the user presence because nothing is blocking the radiation pattern in the direction of the main beam. The shadow of the standing person is very clear at $\phi = 270°$.

In the last case, in Fig. 8(d), the radiation patterns of a user in the data mode with the antenna on the bottom of the prototype are shown. The radiation pattern is uneven and looks similar to the radiation pattern in Fig. 8(b) . However, the person's shadow looks different from that in Fig. 8(c). It can be noticed that there is a big amount of the energy passing around the user and radiating from the back. The power radiated from the back of a person is 20 dB higher than the power in the case with antenna on the top in Fig. 8(c). The amount of the energy that is able to propagate around the user depends on the user width, height, grip type and the phone – user distance. More energy will be propagating around the user to the back if the distance is larger and the user is thinner. Here the user's body acting as a scatterer of the main beam.

In order to understand how much power has propagated around and behind the user (by creeping wave and diffraction) a new metric has been defined. The amount of the power in the shadow in comparison to the total power in whole space will be called a shadowing antenna power ratio(SAPR) in this paper.

The SAPR is defined as:

$$SAPR(\delta\theta,\delta\phi) \triangleq \frac{P_{shadow\ in\ the\ window}}{P_{total}} \tag{4}$$

$$= \frac{\Delta\phi\Delta\theta \sum\limits_{\theta_{min}}^{\theta_{max}} \sum\limits_{\phi_{min}}^{\phi_{max}} (P_{ant,V}(\theta,\phi)+P_{ant,H}(\theta,\phi))\cdot sin(\theta)}{\Delta\phi\Delta\theta \sum\limits_{14°}^{140°} \sum\limits_{0°}^{360°} (P_{ant,V}(\theta,\phi)+P_{ant,H}(\theta,\phi))\cdot sin(\theta)} \tag{5}$$

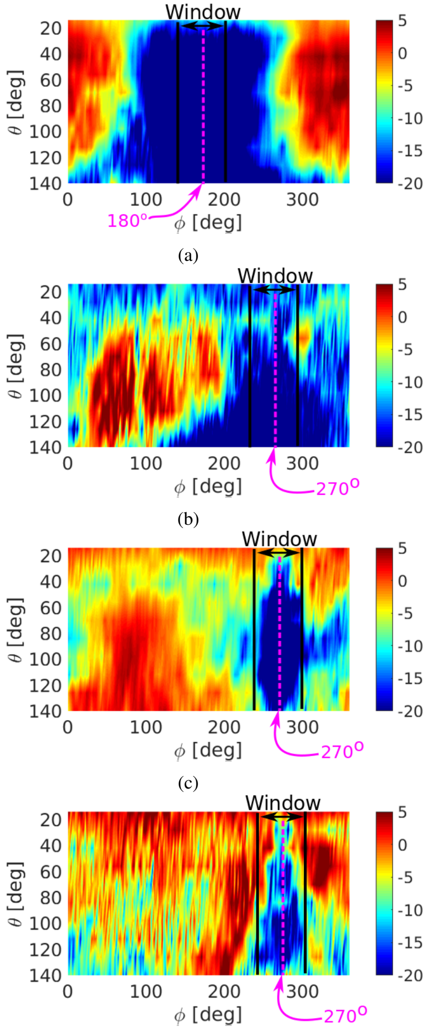

(a)

(b)

(c)

(d)

Fig. 8. The radiation pattern of the antenna with the user in (a) talk mode – antenna on top, (b) talk mode – antenna on bottom, (c) data mode – antenna on top, and (d) data mode – antenna on bottom.

where:

- $\delta\theta = \theta_{max} - \theta_{min}$ is chosen to be constant at maximum of 126°, because of the system constraints.
- $\delta\phi = \phi_{max} - \phi_{min}$ varies from 1° to 60°.
- P_{shadow} is the power in the shadow (in the chosen area of a radiation pattern).
- P_{total} is the total radiated power with the user.

The physical meaning of the formula is: how many dB in the shadow is lower than the total radiated power (TRP).

If SAPR is low then the shadowing is strong, on the other hand, if the SAPR is high then the shadowing is weak. The windows where SAPR has been calculated are displayed in Fig. 8. The location of the window depends on the location of the shadowing region of interest. If more power is transmitted towards the shadow the SAPR would show the amount power propagated behind the shadow by creeping waves and diffraction. The shadowing region location in this paper depends on the user and a mobile phone orientation. In Fig. 8(a) the shadow region is located at $\phi = 180°$. In the rest of the sub-figures in Fig 8 the shadowing region is located at $\phi = 270°$. The window length is fixed in elevation plane as $\theta = 0°$ to 140°. The SAPR is calculated for the different azimuth window lengths for all of the users at 28 GHz.

An error-bar SAPR plot is displayed for the different ϕ window lengths in Fig. 9. In Fig. 9(a) the SAPR is shown for the talk mode and top antenna location. As expected, the SAPR is very low because of the big shadowing from the head. The variation in SAPR does not exceed 10 dB. The variation

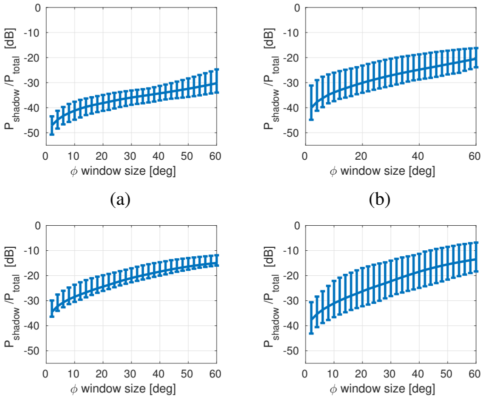

(a)

(b)

(c)

(d)

Fig. 9. SAPR of the antenna with the user in (a) talk mode – antenna on top, (b) talk mode – antenna on bottom, (c) data mode – antenna on top, and (d) data mode – antenna on bottom.

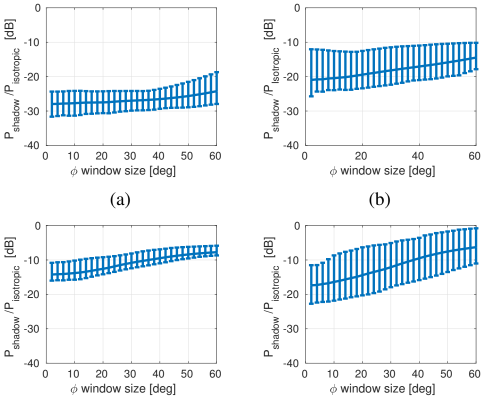

(a)

(b)

(c)

(d)

Fig. 10. SIAPR of the antenna with the user in (a) talk mode – antenna on top, (b) talk mode – antenna on bottom, (c) data mode – antenna on top, and (d) data mode – antenna on bottom.

is smaller for the low SAPR values. In Fig. 9(b) the SAPR for the talk mode and antenna bottom location is shown. The SAPR error-bar plot has bigger variation, especially for the small window sizes than SAPR in Fig. 9(a). Furthermore the mean SAPR curve is steeper. In Fig. 9(c) the SAPR for the data mode and antenna top location is plotted. The mean SAPR is higher than in the talk mode. The variation is on average 5-10 dB smaller than the SAPR for the talk mode.Finally, in Fig. 9(d) the SAPR for the data mode and antenna on the bottom is shown. Up to 20 dB of variation between the users can be observed.

The curves of the mean SAPR for all four setups are shown in Fig. 11. For the small window sizes, the difference in SAPR between the curves tends to decrease. The mean SAPR curve for the talk mode and top antenna location is on average 10 dB lower than the curve for the talk mode and bottom antenna location. The curves for the data mode are on average 5 dB higher than the curve for the talk mode and antenna on the bottom. It is important to address that on average the SAPR for the bottom and top antenna locations in data mode is very similar. However, the variance in SAPR for the bottom antenna location is higher. From the physical point of view, it can be explained that for the bottom antenna location sometimes a big amount of energy can propagate around the user, but on average the power in shadowing region is the same as in the case with antenna top location in data mode.

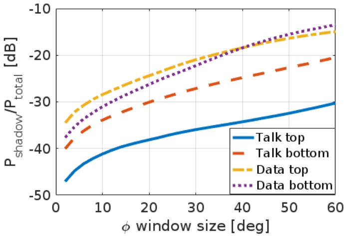

Fig. 11. Mean SAPR for all four measurement setups.

Next, the another parameter of shadow isotropic antenna power ratio (SIAPR), which is not related to antenna TRP. The SIAPR uses a dual polarized isotropic antenna as a reference (gain = 0 dB) instead of the antenna under the test itself. Where the SAPR involves the antenna radiation characteristics the SIAPR only focus on shadowing power characteristics. The SIAPR is defined as:

$$SIAPR(\delta\theta,\delta\phi) \triangleq \frac{P_{shadow\ in\ the\ window}}{P_{isotropic\ antenna\ in\ the\ window}} \tag{6}$$

$$= \frac{\Delta\phi\Delta\theta \sum_{\theta_{min}}^{\theta_{max}} \sum_{\phi_{min}}^{\phi_{max}} (P_{aut,V}(\theta,\phi) + P_{aut,H}(\theta,\phi)) \cdot sin(\theta)}{\Delta\phi\Delta\theta \sum_{\theta_{min}}^{\theta_{max}} \sum_{\phi_{min}}^{\phi_{max}} (P_{iso,V}(\theta,\phi) + P_{iso,H}(\theta,\phi)) \cdot sin(\theta)} \tag{7}$$

where:

- $\delta\theta = \theta_{max} - \theta_{min}$ is chosen to be constant at maximum of 126°, because of the system constraints.
- $\delta\phi = \phi_{max} - \phi_{min}$ varies from 1° to 60°.
- P_{shadow} is the power in the shadow (in the chosen area of a radiation pattern).
- $P_{isotropic\ antenna}$ is the power calculated for the same area in space for the isotropic antenna.
- $P_{aut,V}$ *and* $P_{aut,H}$ are vertical and horizontal power components of the antenna under the test.
- $P_{iso,V}$ *and* $P_{iso,H}$ are vertical and horizontal power components of the isotropic antenna.

The SIAPR for the all four test setups has been plotted in Fig.10. It can be noticed that all of the curves are flatter in respect to the curves in Fig.9, and variation between the users is more constant across the window widths. The SIAPR can be used when comparing the power in the shadowing of antennas with the different radiation patterns. In the talk mode, the different types of antennas (e.g., patch, slot, endfire-radiated notch, dipole and so on) mainly change the power distribution outside the shadow. The SIAPR is similar if different types of antennas are placed at the same location of the chassis under the same user gesture. In data mode, we choose the two cases of antenna (endfire) beam pointing at a user and pointing against a user. If the pattern is broadside, the SIAPR should be between the values of these two cases. Therefore, even though in this paper only the antenna with endfire radiation patterns are studied, the SIAPR obtained in this paper can still provide some guidance for the antenna with other radiation patterns (e.g. broadside radiation pattern).

B. Body Loss

In this section, the measured body loss will be presented. The early investigations in [8] have shown that more than 45 % of the power is lost in the head and hand at the GMS and DECT frequencies. In [13] has been found that around 10.9 dB of body loss is expected for the GSM frequencies. In [15] it has been found that the variation in the body loss between persons is higher when the user selected grip is used. Furthermore, a 3 dB in a standard deviation of a body loss has been observed. In [11] a body loss at the 776 MHz and 2300 MHz has been measured. The measured mean body loss has a range of 0-15 dB, of which most of the values were located under 6 dB.

The body loss has been illustrated in Fig. 12 by an error bar graph. The body loss for the measurement setup in the talk mode and the antenna located on the top of the phone is shown in Fig. 12(a). It can be observed that on average around 4 dB of the body loss is expected. However, the variations in the body loss between the users are much lower in comparison to the studies done for the lower frequency in [9] and [21] when a user selected grip is used.

In Fig. 12(b) the body loss for the antenna on the bottom of the phone in the talk mode is displayed. From the plot, it can be noticed that the mean body loss is 0.2 to 0.3 dB lower than in Fig. 12(a), which means that there is only a small difference in the body loss when antenna located on the top or the bottom of the mobile device in the talk mode. The variation of the body loss in Fig. 12(b) is around 1 dB smaller than in Fig. 12(a).

In data mode, in Fig. 12(c) and 12(d), the variation of the body loss between the users is higher. It can be speculated that the loss is affected by the multiple variables, such as user's height, weight and grip type. If the distance between a user and a phone is not controlled then the variation between users is expected to increase dramatically because of the difference in shadowing area.

The mean body loss in the data mode and the antenna top location is very low. In Fig. 12(c) around 0.7 to 1.5 dB of the body loss is expected for this particular setup.

On the other hand, in the setup with the antenna located on the bottom of the mobile device in data mode the mean body loss, shown in Fig. 12(d), is comparable to the losses in the talk mode. The expected mean body loss ranges from 3.5 to 4 dB. The variance of the body loss, calculated from the statistical data, is shown in Fig. 13. A variance of the body loss in the talk mode and antenna on top varies from 0.4 to 0.7 dB in the measured band. The body loss in talk mode and antenna on the bottom has less variation in the band. Those two curves have same variance value at 28.7 GHz. The variance in the data mode and bottom antenna location is 0.2 to 0.5 dB lower than the variance of the body loss in the talk mode. The variance of the body loss for the setup in the data mode and antenna top location is the lowest of all four, which is under 0.1 dB.

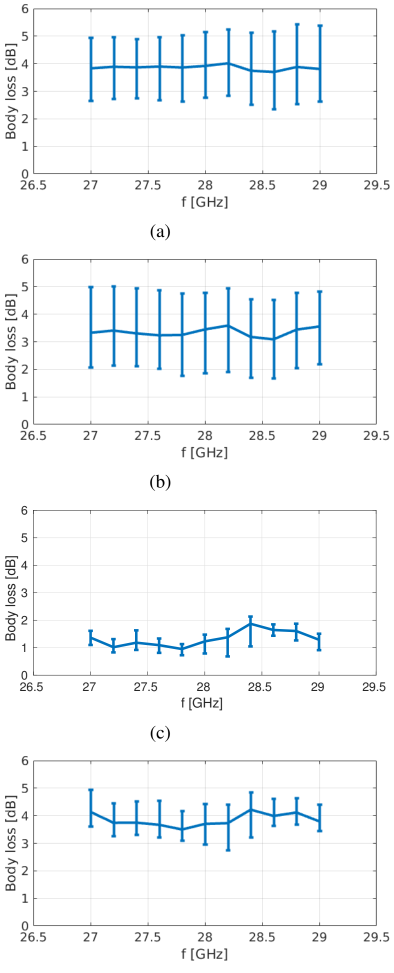

(a)

(b)

(c)

(d)

Fig. 12. The minimum, maximum and mean body loss in frequency band from 27 to 29 GHz for the users in (a) talk mode – antenna on top, (b) talk mode – antenna on bottom, (c) data mode – antenna on top, and (d) data mode – antenna on bottom.

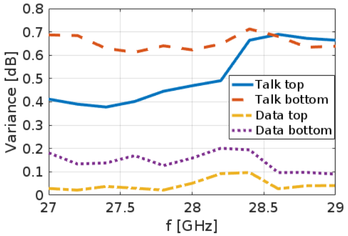

Fig. 13. Variance of the body loss for the all four setups.

C. *Coverage efficiency*

In this subsection the impact of the user on the antenna coverage at 28 GHz will be studied. Usually, coverage efficiency metric is used to calculate the coverage of the phased array. However, in this paper, the coverage efficiency of only one antenna element is calculated. If the element is placed into an array the antenna gain should be multiplied by the array factor. For example, for an array of 8 elements an increase of 9 dB is expected. The behavior of the antenna array can be predicted to some extent by looking on the coverage of the one element. The coverage efficiency of the antenna in all four of the case studies is plotted in Fig. 14, where the red curve represents the coverage efficiency of the antenna in the free space.

Both curves for the talk mode in Fig. 14(a) and 14(b) look very similar. The variation in the coverage for different users increases with the bottom antenna. Both curves follow the red curve only for the high and very low antenna gains.

The coverage efficiency error bar plots for the data mode are shown in Fig. 14(c) and 14(d). Both mean coverage efficiency curves have a shape very similar to the curve of the antenna coverage in the free space. However, the variance between the users is higher for the antenna located on the bottom of the mobile device in Fig. 14(d). It can be observed in both pictures that the user effects actually very close to the free space curve.

IV. COMPARISON OF THE RESULTS

The variation of the SAPR is different for each of the four measurement setups. The SAPR mean, variance, minimum and maximum measured values are shown in Tab. I for the window of 30°. This shadowing window width is encountered in all four setups.

The mean body loss of at least 3.2 dB is expected in the talk mode. In data mode when the antenna is located on the bottom

Table I. Measured parameters at 28 GHz

Setup	SAPR @ 30° [dB]				Body loss [dB]				Coverage efficiency @ 0 dBi			
	Mean	Var	Max	Min	Mean	Var	Max	Min	Mean	Var	Max	Min
Talk – top	-35.95	4.07	-33.13	-38.85	3.86	0.45	5.1	2.8	0.14	4.14E−4	0.18	0.1
Talk – bottom	-27.15	9.77	-20.44	-31.32	3.25	0.64	4.8	1.9	0.12	9.74E−4	0.19	0.08
Data – top	-20.98	2.60	-17.07	-22.67	1.45	0.02	1.5	0.8	0.20	0.0027	0.36	0.17
Data – bottom	-22.25	12.84	-14.03	-28.17	3.45	0.13	4.5	3	0.11	0.0025	0.26	0.07

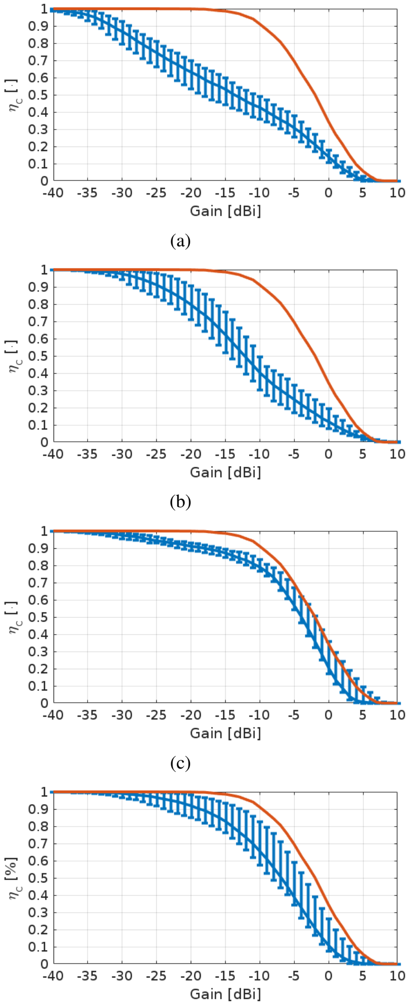

(a)

(b)

(c)

(d)

Fig. 14. The coverage efficiency of the (a) antenna on top in talk mode, (b) antenna on bottom in talk mode, (c) antenna on top in data mode, and (d) antenna on bottom in data mode. The red curve represent the coverage efficiency in the free space.

of the mobile device, a loss of 3.5-4 dB is expected. In the data mode and antenna top location, only 1 dB of the body loss is expected. The variation in the loss between the users does not exceed 2 dB. Higher body losses in data mode are expected when the distance between a user and a mobile device is smaller than the chosen 30 cm. The mean, variance, maximum and minimum values for the antenna center frequency of 28 GHz are shown in Tab. I.

The coverage efficiency of the antenna at the 0 dBi is at least 30 % lower for the antenna used in talk mode in comparison to the free space. The coverage of the antenna in the data mode is very similar to the coverage of the antenna in free space. The more detailed overview of the mean, variance, maximum and minimum values of the coverage efficiency at 0 dBi is shown in Tab. I. The realized gain of 0 dBi is chosen to show how much coverage the antenna has compared to the ideal isotropic antenna. When antennas are combined into array, a gain increase of 9 dBi over a single element is expected for the 8-element array. Thus, the coverage efficiency value at 0 dB will tell approximately how much coverage an array composed of such antenna elements would have at 9 dBi gain.

V. CONCLUSION

In this paper, a study of the body loss, shadowing area and coverage efficiency of the mobile terminal antenna at 28 GHz has been presented. The results are based on the measurement campaign involving 12 persons.

From all the studies of the multiple radiation patterns, it can be concluded that in data mode, when the beam is pointing towards the user, it is still possible to decrease the power in the shadowing region by the creeping waves and diffractions. Furthermore, when antenna located on the bottom of the mobile device the palm and the fingers of the user will affect the radiation pattern. A significant amount of power is still able to propagate through the hand. A measure of shadowing power ratio has been proposed to characterize the shadowing region. The highest mean SAPR has been obtained from the measurements in the data mode with the antenna on the bottom of a device.

The measure of SAPR has been proposed and calculated statistically from the radiation patterns in talk and data modes. For the small window sizes the biggest shadowing in expected for the talk mode with the antenna on top. The smallest variation of SAPR can be observed for the setups where the antenna was positioned on the top of the mobile device.

The mean body loss of less than 4 dB for all of the measurement setups has been observed. The body loss is much lower than the body loss observed for the low frequencies (<6 GHz). Furthermore, the variation in the body loss between the users is less than 4 dB, and even less than 1 dB in some cases.

The coverage efficiency for the antenna at 0 dB gain is between 10 and 20 %. The variation in the coverage efficiency of 19 % in the worst case and 11 % in the best case has been observed.

To make the presented study more general the measurement with the children, woman and people older than 30 could be carried out in the future. From the study, it can clearly be seen that to obtain the optimal antenna performance at least two antennas on the top and bottom should be integrated into the design of a mobile device.

ACKNOWLEDGMENT

The authors would like to thank Kristian Bank for helping with the setup of the measurement equipment. Furthermore authors would like to thank 7th and 9th semester Wireless Communication System students at the Aalborg University for the participation in the measurement campaign.

REFERENCES

[1] T. S. Rappaport, S. Sun, R. Mayzus, H. Zhao, Y. Azar, K. Wang, G. N. Wong, J. K. Schulz, M. Samimi, and F. Gutierrez, “Millimeter wave mobile communications for 5g cellular: It will work!,” *IEEE Access*, vol. 1, pp. 335–349, 2013.

[2] W. Roh, J. Y. Seol, J. Park, B. Lee, J. Lee, Y. Kim, J. Cho, K. Cheun, and F. Aryanfar, “Millimeter-wave beamforming as an enabling technology for 5g cellular communications: theoretical feasibility and prototype results,” *IEEE Communications Magazine*, vol. 52, pp. 106–113, February 2014.

[3] N. Ojaroudiparchin, M. Shen, and G. Pedersen, “Multi-layer 5g mobile phone antenna for multi-user mimo communications,” *Telecommunications Forum Telfor (TELFOR), 2015 23rd*, pp. 559–562, Nov 2015.

[4] W. Hong, K. Baek, Y. Lee, and Y. G. Kim, “Design and analysis of a low-profile 28 ghz beam steering antenna solution for future 5g cellular applications,” *Microwave Symposium (IMS), 2014 IEEE MTT-S International*, pp. 1–4, June 2014.

[5] W. Hong, K. H. Baek, Y. Lee, Y. Kim, and S. T. Ko, “Study and prototyping of practically large-scale mmwave antenna systems for 5g cellular devices,” *IEEE Communications Magazine*, vol. 52, pp. 63–69, September 2014.

[6] T. Wu, T. S. Rappaport, and C. M. Collins, “The human body and millimeter-wave wireless communication systems: Interactions and implications,” in *2015 IEEE International Conference on Communications (ICC)*, pp. 2423–2429, June 2015.

[7] O. P. Gandhi and A. Riazi, “Absorption of millimeter waves by human beings and its biological implications,” *IEEE Transactions on Microwave Theory and Techniques*, vol. 34, pp. 228–235, Feb 1986.

[8] J. Toftgard, S. N. Hornsleth, and J. B. Andersen, “Effects on portable antennas of the presence of a person,” *IEEE Transactions on Antennas and Propagation*, vol. 41, pp. 739–746, Jun 1993.

[9] J. B. Andersen, J. O. Nielsen, and G. F. Pedersen, “Absorption related to hand-held devices in data mode,” *IEEE Transactions on Electromagnetic Compatibility*, vol. 58, pp. 47–53, Feb 2016.

[10] J. O. Nielsen and G. F. Pedersen, “Mobile handset performance evaluation using radiation pattern measurements,” *IEEE Transactions on Antennas and Propagation*, vol. 54, pp. 2154–2165, July 2006.

[11] J. O. Nielsen, B. Yanakiev, I. B. Bonev, M. Christensen, G. F. Pedersen, C. Luxey, A. Dialled, and I. Dicmm, “User influence on the mean effective gain for data mode operation of mobile handsets,” in *2012 6th European Conference on Antennas and Propagation (EUCAP)*, pp. 2759–2763, March 2012.

[12] M. Pelosi, O. Franek, M. B. Knudsen, G. F. Pedersen, and J. B. Andersen, “Antenna proximity effects for talk and data modes in mobile phones,” *IEEE Antennas and Propagation Magazine*, vol. 52, pp. 15–27, June 2010.

[13] K. R. Boyle, “The performance of gsm 900 antennas in the presence of people and phantoms,” in *Antennas and Propagation, 2003. (ICAP 2003). Twelfth International Conference on (Conf. Publ. No. 491)*, vol. 1, pp. 35–38 vol.1, March 2003.

[14] J. O. Nielsen, G. F. Pedersen, K. Olesen, and I. Z. Kovacs, “Statistics of measured body loss for mobile phones,” *IEEE Transactions on Antennas and Propagation*, vol. 49, pp. 1351–1353, Sep 2001.

[15] J. Krogerus, J. Toivanen, C. Icheln, and P. Vainikainen, “Effect of the human body on total radiated power and the 3-d radiation pattern of mobile handsets,” *IEEE Transactions on Instrumentation and Measurement*, vol. 56, pp. 2375–2385, Dec 2007.

[16] J. Ilvonen, O. Kivekas, J. Holopainen, R. Valkonen, K. Rasilainen, and P. Vainikainen, “Mobile terminal antenna performance with the user’s hand: Effect of antenna dimensioning and location,” *IEEE Antennas and Wireless Propagation Letters*, vol. 10, pp. 772–775, 2011.

[17] J. Holopainen, O. Kivekas, J. Ilvonen, R. Valkonen, C. Icheln, and P. Vainikainen, “Effect of the user’s hands on the operation of lower uhf-band mobile terminal antennas: Focus on digital television receiver,” *IEEE Transactions on Electromagnetic Compatibility*, vol. 53, pp. 831–841, Aug 2011.

[18] K. Zhao, J. Helander, D. Sjoberg, S. He, T. Bolin, and Z. Ying, “User body effect on phased array in user equipment for 5g mm wave communication system,” *IEEE Antennas and Wireless Propagation Letters*, vol. PP, no. 99, pp. 1–1, 2016.

[19] J. Helander and Z. Ying, “Stripline coupled antenna with periodic slots for wireless electronic devices.” US Patent, US 14/534,445, May, 2016.

[20] J. Helander, K. Zhao, Z. Ying, and D. Sjöberg, “Performance analysis of millimeter-wave phased array antennas in cellular handsets,” *IEEE Antennas and Wireless Propagation Letters*, vol. 15, pp. 504–507, 2016.

[21] J. Krogerus, J. Toivanen, C. Icheln, and P. Vainikainen, “User effect on total radiated power and 3-d radiation pattern of mobile handsets,” *Antennas and Propagation, 2006. EuCAP 2006. First European Conference on*, pp. 1–6, Nov 2006.

Igor Syrytsin was born in Saratov, Russia, in 1988. He received the B.S. degree in electronic engineering and IT and M.S. degree in wireless communication systems from Aalborg University, Aalborg, Denmark, in 2014 and 2016, respectively. Currently, he is pursuing the Ph.D. degree at Department of Electronic Systems at Aalborg University. His research interests include mm-Wave mobile antenna design and interactions between user and mobile antennas.

Shaui Zhang was born in Liaoning, China, in 1983. He received the B.E. degree from the University of Electronic Science and Technology of China, Chengdu, China, in 2007 and the Ph.D. degree in electromagnetic engineering from the Royal Institute of Technology (KTH), Stockholm, Sweden, in 2013. After his Ph.D. studies, he was a Research Fellow at KTH. In April 2014, he joined Aalborg University, Denmark, where he currently works as Assistant Professor. He is also an external antenna specialist at Bang & Olufsen, Denmark. In 2010 and 2011, he was a Visiting Researcher at Lund University, Sweden and at Sony Mobile Communications AB, Sweden, respectively. His research interests include: mobile terminal mmwave antennas, biological effects, UWB wind turbine blade deflection sensing, MIMO antenna systems, and RFID antennas.

Gert Frølund Pedersen was born in 1965. He received the B.Sc. and E.E. (Hons.) degrees in electrical engineering from the College of Technology in Dublin, Dublin Institute of Technology, Dublin, Ireland, in 1991, and the M.Sc.E.E. and Ph.D. degrees from Aalborg University, Aalborg, Denmark, in 1993 and 2003, respectively. Since 1993, he has been with Aalborg University where he is a Full Professor heading the Antenna, Propagation and Networking LAB with 36 researchers. He is also the Head of the Doctoral School on wireless communication with some 100 Ph.D. students enrolled. His research interests include radio communication for mobile terminals especially small antennas, diversity systems, propagation, and biological effects. He has published more than 175 peer reviewed papers and holds 28 patents. He has also worked as a Consultant for developments of more than 100 antennas for mobile terminals including the first internal antenna for mobile phones in 1994 with lowest SAR, first internal triple-band antenna in 1998 with low SAR and high TRP and TIS, and lately various multiantenna systems rated as the most efficient on the market. He has worked most of the time with joint university and industry projects and have received more than 12 M$ in direct research funding. He is currently the Project Leader of the SAFE project with a total budget of 8 M$ investigating tunable front end including tunable antennas for the future multiband mobile phones. He has been one of the pioneers in establishing over-the-air measurement systems. The measurement technique is now well established for mobile terminals with single antennas and he was chairing the various COST groups (swg2.2 of COST 259, 273, 2100, and now ICT1004) with liaison to 3GPP for over-the-air test of MIMO terminals. He is currently involved in MIMO OTA measurement.

Kun Zhao received the B.S. degree in Communication Engineering from Beijing University of Posts and Telecommunications (BUPT), Beijing, China in 2010 and M.S. degree in Wireless Systems from Royal Institute of Technology (KTH), Stockholm, Sweden, in 2012. Currently, he is working toward the Ph. D. degree at Department of Electromagnetic Engineering, KTH. He has been a visiting researcher at the Department of Electrical and Information Technology, Lund University, Sweden, and Sony Mobile Communication AB, Sweden. His current research interests include mmWave antenna and propagation for 5G communications, MIMO antenna systems, multiple antennas-user interactions and body centric wireless communications.

Thomas Bolin received the M.Sc. in Applied Physics and Electrical Engineering degree from Linköping University, Sweden in 1979. From 1979 to 1983 he was an RF-engineer at ITT Standard Radio & Telefon AB in Stockholm doing 1 kW HF PA design. From 1983 to 2001 he held a technical management position at Ericsson Mobile Communications in Lund Sweden doing RF and antenna product development but also OTA measurement technology development for mobile handsets. From 2001 to 2011 he held the same position within Sony Ericsson Mobile Communications in Lund and since 2011 at Sony Mobile Communications in Lund now more devoted to antenna research and standardization. Lately he assisted in development of cm-wave antenna arrays (15-30 GHz) for 5G.

Zhinong Ying (SM'05) is a principal engineer (senior expert) of antenna technology in Network Research Lab. Research and Technology, Sony Mobile Communication AB within Sony Group, Lund, Sweden. He joined Ericsson AB in 1995. He became Senior Specialist in 1997 and Expert in 2003 in his engineer career at Ericsson, and Principal Engineer at Sony Group. His main research interests are small antennas, broad and multi-band antenna, multi-channel antenna (MIMO) system, near- field and human body effects and measurement techniques. He has authored and co-authored over 90 papers in various of journal, conference and industry publications. He holds more than 80 patents and pending in the antenna and mobile terminal areas. He contributed a book chapter to the well known "Mobile Antenna Handbook 3rd edition" edited by Dr. H. Fujimoto. He had invented and designed various types of multi-band antennas and compact MIMO antennas for the mobile industry. One of his contributions in 1990's is the development of non-uniform helical antenna. The innovative designs are widely used in mobile terminal industry. His patented designs have reached a commercial penetration of more than several hundreds million products in worldwide. He received the Best Invention Award at Ericsson Mobile in 1996 and Key Performer Award at Sony Ericsson in 2002. He was nominated for President Award at Sony Ericsson in 2004 for his innovative contributions. He has been guest professor in Zhejiang University, China since 2002. He served as TPC Co-Chairmen in International Symposium on Antenna Technology (iWAT), 2007, and served as session organizer of several international conferences including IEEE APS, and a reviewer for several academic journals. He is a senior member of IEEE. He was a member of scientific board of ACE program (Antenna Centre of Excellent in European 6th frame) from 2004 to 2007.

Paper B

User Effects on the Circular Polarization of 5G Mobile Terminal Antennas

Igor Syrytsin, Shuai Zhang, Gert Frølund Pedersen, Zhinong Ying

The paper has been published in:
IEEE Transactions on Antennas and Propagation, Vol. 66, Issue 9, pp. 4906-4911, 2018.

Abstract

In 5G mm-wave mobile terminal applications, user's body has a very high chance to create blockage or shadow to the radiation patterns of handset antenna arrays. User effects on a circularly polarized phased array for 5G mobile applications for frequencies around 28 GHz are studied in this paper. Two figures of merit are defined: the total scan pattern and coverage efficiency of the circular polarization (CP). The user effects on the performance of a CP phased array are studied via two defined parameters. The investigations are carried out in talk mode (with a hand and a head) and in data mode (with a homogeneous whole-body phantom). The scattering properties of the proposed phantom are verified via the measurement of an antenna with known radiation parameters and a human. The CP coverage efficiency is relatively less affected by biological tissues than by the conventional coverage efficiency, though the absolute value of the CP coverage efficiency depends on a specific design. When user effects are introduced, the axial ratio (AR) bandwidth becomes approximately 0.8 to 1.3 GHz narrower. To realize the optimal CP performance and reduce the user effects of the CP coverage efficiency, a CP array at the bottom short edge of the ground plane should be chosen in talk mode, while the top short edge location should be chosen in data mode.

DOI:

https://ieeexplore.ieee.org/document/8399838

User Effects on the Circular Polarization of 5G Mobile Terminal Antennas

Igor Syrytsin, Shuai Zhang, Gert Frølund Pedersen, *Member, IEEE*, Zhinong Ying, *Senior Member, IEEE*

***Abstract*—In 5G mm-wave mobile terminal applications, user's body has a very high chance to create blockage or shadow to the radiation patterns of handset antenna arrays.**

User effects on a circularly polarized phased array for 5G mobile applications for frequencies around 28 GHz are studied in this paper.

Two figures of merit are defined: the total scan pattern and coverage efficiency of the circular polarization (CP). The user effects on the performance of a CP phased array are studied via two defined parameters. The investigations are carried out in talk mode (with a hand and a head) and in data mode (with a homogeneous whole-body phantom). The scattering properties of the proposed phantom are verified via the measurement of an antenna with known radiation parameters and a human. The CP coverage efficiency is relatively less affected by biological tissues than by the conventional coverage efficiency, though the absolute value of the CP coverage efficiency depends on a specific design. When user effects are introduced, the axial ratio (AR) bandwidth becomes approximately 0.8 to 1.3 GHz narrower. To realize the optimal CP performance and reduce the user effects of the CP coverage efficiency, a CP array at the bottom short edge of the ground plane should be chosen in talk mode, while the top short edge location should be chosen in data mode.

***Index Terms*—User effects, circular polarization, phased array, mobile handset antenna, 5G antenna, phantom.**

I. INTRODUCTION

THE millimeter/centimeter-wave (mm/cm-wave) frequencies have become an attractive candidate for 5G communication systems where phased arrays should be implemented at both mobile terminals and base stations [1]. Such arrays have been designed to increase the coverage performance of the mobile antenna as in [2] and [3]. Applying a circularly polarized antenna can create multiple benefits when communicating over a wireless medium. In [4], the delay spread can be reduced to 5 ns or even lower if highly directive CP antennas are applied. At 26 GHz, the measurements in [5] have shown that for an indoor non-line of sight (NLOS) scenario, the received signal strength depends on the polarization of the receiving and transmitting antennas. A channel with both Tx and Rx vertical polarization (VP) can be over 10 dB stronger than a channel with both Tx and Rx horizontal polarization (HP). By using a CP or polarization-reconfigurable phased arrays, there can be benefit to keeping the received power at high levels.

Human tissues are well known to be materials with high loss and high permittivity, which will likely affect the performance of mobile terminal antennas. The user impact on mobile terminal antennas has been extensively studied previously for low-frequency bands, such as GSM and LTE in [6] and for cm-waves in [7]. The user effects on the coverage efficiency of mobile phased arrays have been investigated at 3.5 GHz in [8] and at 15 GHz in [9]. A significant loss in the coverage efficiency was observed for both 3.5 GHz and 15 GHz. However, the user effects on the circular polarization (CP) performance of the phased antenna arrays have not been well analyzed at higher frequencies, e.g., between 26 and 31 GHz. In this paper, the user impact on the circular polarization performance of the mobile phased antenna array will be investigated for 5G applications.

A mobile circularly-polarized antenna array with end-fire radiation will be used in this investigation. User effects on the circular polarization performance of the phased antenna array along the frequency range from 26 to 31 GHz will be studied by simulations in CST Microwave Studio transient time domain solver. Two setups with the user will be considered: talk mode, with hand and head, and data mode, with a proposed whole-body homogeneous phantom. Then, the parameters of CP total scan pattern (TSP) and CP coverage efficiency will be introduced to quantify the effects of the user on the CP performance of the array.

II. GEOMETRY AND FREE-SPACE PERFORMANCE

The proposed array element consists of a magnetic dipole and an electric dipole. These two dipoles produce electric fields normal to each other with a 90° phase difference as described in [10]. The antenna is printed on a Rogers 3003 substrate with a thickness of 1.52 mm. The geometry of each antenna element is shown in Fig. 1. The vertical electric field is produced by two identical patches of 4.4 mm × 1.8 mm on each side of the ground plane. The horizontal electric field is produced by the two mirrored dipole arms with the length of 3.7 mm. The antenna is fed between the two patches to obtain a 90° phase difference between the fields, as shown in Fig. 1(a). The patches are connected by two vias with a radius of 0.45 mm. In this paper, the axial ratio (AR) beamwidth and AR bandwidth have been calculated according to the specification of AR $\leq$ 3 dB level. The AR beamwidth and AR bandwidth of the antenna will change with clearance size. Thus, a clearance of 10 mm is selected to obtain a reasonable AR beamwidth and AR bandwidth for this study. The electrically large ground plane of the phone chassis and substrate properties will affect the antenna performance of the low-frequency antenna designs in [10] and [11] at 28 GHz.

Grounding walls and holes were added to the design to suppress the unwanted surface waves. The proposed antenna has a -10 dB and -6 dB impedance bandwidth of 973 MHz (3.475 %) and 2.07 GHz (7.393 %), respectively. The fractional bandwidth was calculated at the central frequency of 28 GHz.

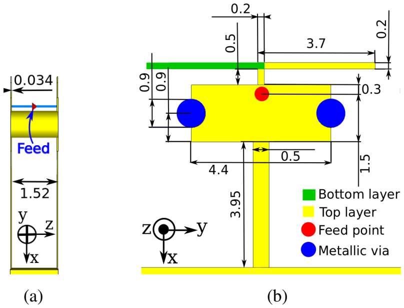

(a) (b)

Fig. 1. Geometry of the antenna element in (a) xz-plane and (b) in xy-plane (Unit: mm).

This work was supported by the Innovationsfonden project of RANGE.(Corresponding author: Shuai Zhang).

Igor Syrytsin, Shuai Zhang, and Gert Frølund Pedersen are with the Antennas, Propagation and Millimeter-wave Systems section at the Department of Electronic Systems, Aalborg University, Denmark (email: {igs,sz,gfp}@es.aau.dk).

Zhinong Ying is with the Corporate Technology Office, Sony Mobile Communication AB, Lund, Sweden.

A. *Array Geometry*

The proposed phased array is shown in Fig. 2. A total of 8 elements are combined into a linear array on the short edge of the ground plane. The antenna array's main lobe direction and the ϕ scan angle are illustrated in Fig. 2. The distance between elements is 7.6 mm (0.7λ).

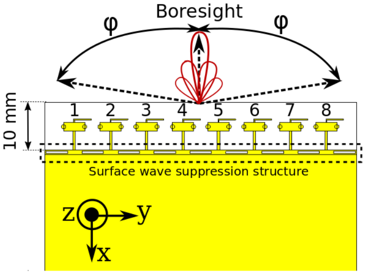

Fig. 2. Proposed antenna array definition, geometry, boresight and scan angle.

B. *Free-Space Performance*

The maximum gain of the array and the AR at the boresight (with in-phase elements) are shown in Fig. 3(a). The AR bandwidth of 4 GHz can be achieved. Maximum gain over 10 dBi is realized from 26 to 31 GHz.

When a beam is scanned into different directions in ϕ plane, the AR at the main beam direction for each scan angle is shown in Fig. 3(b) at 28 GHz. Please note that the curves in Fig. 3(b), Fig. 11, Fig. 12, Fig. 15 and Fig. 16 are plotted at 28 GHz but that similar tendencies have also been observed at the other frequencies in the band. The AR beamwidth (AR $\leq$ 3 dB) of 55° can be realized by the phased array. The maximum gain within the scanning range is over 11 dBi.

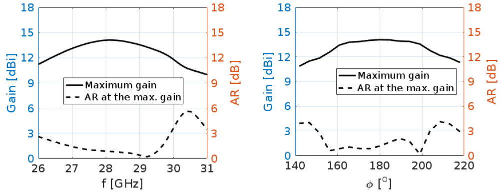

(a) (b)

Fig. 3. Performance of the proposed phased antenna array: (a) maximum gain and AR vs. frequency when the relative phase-shift between antenna elements is 0° and the (b) maximum gain and AR vs scan angle ϕ at 28 GHz.

C. *Figure Of Merit*

Next, the coverage performance of the array is investigated. The coverage efficiency is calculated from the total scan pattern (TSP) of the phased array, which is shown in Fig. 4(a). The TSP is obtained from all phased array patterns, corresponding to the different scan angles, by recording the best achievable gain at every angular distribution point.

The regular coverage efficiency has been defined as [2]:

$$\eta_c = \frac{\text{Coverage Solid Angle}}{\text{Maximum Solid Angle}} \tag{1}$$

where the maximum solid angle defined as 4π steradians. A CP coverage efficiency specifies the coverage efficiency defined in [2] with respect to the antenna's circular polarization performance. The CP coverage efficiency can be calculated from the total scan pattern by only considering the points in space where AR $\leq$ 3 dB. The CP coverage efficiency is defined in this paper as:

$$\eta_{c,CP} = \frac{\left.\text{Coverage Solid Angle}\right|_{AR<3\,\text{dB}}}{\text{Maximum Solid Angle}} \tag{2}$$

where the maximum solid angle is defined as 4π steradians.

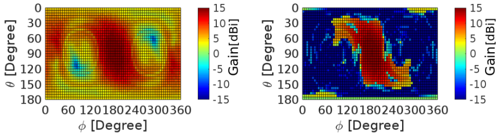

(a) (b)

Fig. 4. (a) Total scan pattern in a general case and (b) CP total scan pattern at 28 GHz.

The regular and CP coverage efficiencies of the array in free space are shown in Fig. 5. For the threshold gain lower than 5 dBi, the CP coverage efficiency of the curve is at least 0.4 lower than the corresponding free-space regular coverage efficiency curve. Moreover, the CP coverage efficiency curve cannot easily reach 100 % of coverage, which is limited by the CP performance of the proposed antenna. The free-space CP coverage curve is at $\eta_c = 0.6$ level for the gain lower than -20 dBi in Fig. 5.

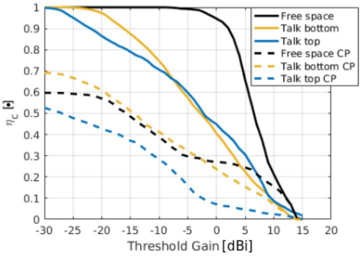

Fig. 5. Comparison of the regular coverage efficiency and CP coverage efficiency between the free space and talk mode.

III. Accuracy Verification of Simulations with Phantom

It is important to notice that CP measurements with the user are very time consuming and challenging. It is difficult to make the user sit/stand still for a prolonged period of measurement. These measurement setup challenges will lead to instability in the phase of the measured pattern. If the measured phase is not correct, then performing the beamforming correctly is nearly impossible. Therefore, simulations with realistic phantoms for data and talk modes have been done in CST Microwave Studio FDTD solver instead of the measurements. Furthermore, at the time of the writing, no standards for human gestures at high frequencies were available.

A. *Phantom Description*

For the data mode, a phantom is proposed in this paper for 28 GHz, and is shown in Fig. 6(a). The homogeneous full-body phantom is made of skin tissue with the dielectric permittivity of $\varepsilon_r = 16.5 + j16.5$. The parameters of different tissues (including skin) for up to 100 GHz have been measured in [12]. The proposed phantom dimensions are based on the mean values instead of using a specific human specimen. The length of the limbs for the whole-body phantom are chosen according to the average male human dimensions described in [13]. The average weight and body circumference are based on the measurements in [14]. The detailed dimensions of the phantom are shown in Table I. On the other hand, in the talk mode, the hand and head phantom gestures defined in the existing CTIA standards are used [15]. The skin tissue dielectric constant is chosen to be a value similar to that used for the whole-body phantom.

The use of the skin-only phantom is justified because the waves will not penetrate deep into the human tissue at these frequencies. For example, the skin depth at 28 GHz can be calculated as:

$$\delta_s = \sqrt{\frac{\rho}{\pi \cdot f \cdot \mu}} = 4.708\,\text{mm} \tag{3}$$

where ρ is a resistivity of the human tissue chosen to 245 Ωcm or 245E6 μΩcm [16], f is a frequency, and $\mu = \mu_0 \cdot \mu_r$ is skin permeability. For this calculation the $\mu_r = 1$ has been chosen. The phantom can be used to evaluate mobile antenna performance in data mode at a frequency of 28 GHz.

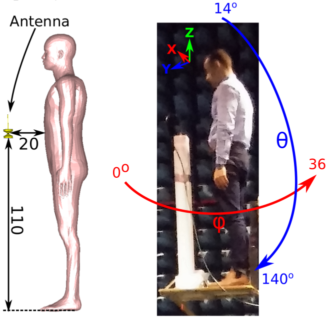

(a) (b)

Fig. 6. Setup with biconical antenna used in (a) simulation and (b) measurement (Unit: cm).

Table I. Dimensions of the phantom and the measured user.

Category	Phantom	User
Height	175.6 cm	174 cm
Neck circumference	42.8 cm	43 cm
Upper arm length	25 cm	24 cm
Upper arm circumference	27.8 cm	32 cm
Lower arm length	27 cm	27.7 cm
Wrist circumference	15 cm	16 cm
Chest circumference	108 cm	111 cm
Waist circumference	89 cm	86 cm
Hip circumference	101 cm	97 cm
Upper leg length	40 cm	40 cm
Lower leg length	50 cm	45 cm
Ankle circumference	22 cm	22 cm

B. *Scattering Properties of the Phantom*

The phantom's accuracy is verified by measuring the linearly polarized omnidirectional UWB antenna proposed by [17] in two orientations. The chosen antenna has a gain of approximately 5 dBi at 28 GHz. The measurements were made in an anechoic chamber using a single dual-polarized probe antenna in the far field. To remove the uncertainty of the user grip, the antenna is suspended during free-space simulations (Fig. 6(a)) and placed on a foam stand during the measurements (Fig. 6(b)). The coordinate system used in both measurement and simulation is shown in Fig. 6(b).

The measured user has some of the dimensions of the phantom's but different body types. In Table I, the dimensions of the user can be compared to the dimensions of the phantom. In Fig. 7, the simulated and measured radiation patterns with each user and different antenna orientations are shown. In general, the measured and the simulated patterns have a similar shape. The measurements are relatively more noisy due to the cable and connector used for the prototype in the 28 GHz band. In addition, the shadowing sizes are slightly different due to the difficulty of maintaining the exact same antenna position during the measurements. Furthermore, the user's gestures cannot be identical to the simulations.

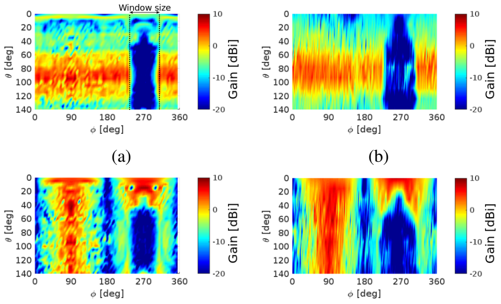

(a) (b) (c) (d)

Fig. 7. Radiation pattern at 28 GHz of (a) simulated antenna - θ polarized, (b) measured antenna - θ polarized, (c) simulated antenna - ϕ polarized, and (d) measured antenna - ϕ polarized.

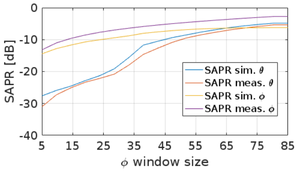

Fig. 8. SAPR of the θ and ϕ polarizations of bi-conical antenna simulated with the phantom and measured with the user.

Next, the shadowing region (around 270° in Fig. 7) in the measured and simulated radiation patterns was investigated. The shadowing antenna power ratio (SAPR) metric is used for this investigation and defined in [7] as:

$$SAPR(\Delta\theta, \Delta\phi) \triangleq \frac{P_{shadow\ in\ the\ window}}{P_{total}} \tag{4}$$

where $\Delta\theta = \theta_{max} - \theta_{min}$ is a window length in θ. Here, 140° is chosen, which is the maximum measured θ range. $\Delta\phi = \phi_{max} - \phi_{min}$ is a variable window, the size of which varies from 1° to 85°. The example of the *phi* window size is marked in Fig. 7(a). The window is centered around $\phi = 270°$. P_{shadow} is the power in the shadow (in the chosen area of a radiation pattern). P_{total} is the total radiated power of the antenna.

The formula describes how much lower the power is in the shadow compared to the total radiated power (TRP). In Fig. 8, the SAPR has been calculated for the ϕ and θ polarized radiation patterns of the bi-conical antenna in the measurements and simulations. The SAPR curves for the ϕ and θ polarizations have a very similar tendency in dB. The small difference between the simulated and measured results is because of the same reasons for those in Fig. 7. In general, the proposed phantom has similar external (scattering) properties as the real human user.

From this section, it can be concluded that a proposed phantom can be used to model the scattering properties of the user. This is concluded based on the investigation of the shadowing region created by the user's body and on corresponding calculations of SAPR for the theta and phi polarized antennas.

IV. TALK MODE SIMULATIONS

In this section, the phased array described in subsections II-A and II-B have been studied in talk mode, where the user is holding the mobile device close to the ear in the right hand. Investigations were performed to quantify the user effects on regular and CP coverage efficiency, AR bandwidth and AR beamwidth. In the simulation, more than 41 million mesh cells were used. The smallest cell size was 0.05 mm and the largest mesh cell size was 0.856 mm. The setup with the user's head and hand (talk mode) is shown in Fig. 9. The array is located on the bottom of the device in Fig. 9(a) or on the top in Fig. 9(b). The mobile device was placed according to the test standards as defined in [15], and the distance between the ear and the phone chassis was 4 mm.

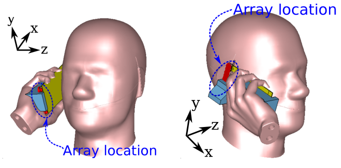

(a) (b)

Fig. 9. User setup with the proposed phased antenna array on the (a) bottom and (b) top.

A. AR Bandwidth

The AR and maximum gain are plotted in Fig. 10(a) for the bottom antenna location. The AR has less than 3 dB from 27 to 30.2 GHz, which corresponds to an AR bandwidth of 3.2 GHz. The AR bandwidth is 0.8 GHz lower than the free-space AR bandwidth. Maximum gain is at least 1 dB lower than in the case of free space. The AR and maximum gain are plotted in Fig. 10(b) for the top antenna location. Heavier shadowing is observed because the array is closer to the user's head. The AR is lower than 3 dB from 27.3 to 30 GHz, which corresponds to the AR bandwidth of 2.7 GHz. The AR bandwidth is 1.3 GHz and 0.5 GHz smaller than the case of the free space and when the antenna is located on the bottom, respectively. Maximum gain is actually 2 dB higher than the maximum gain in the free space due to scattering from the head.

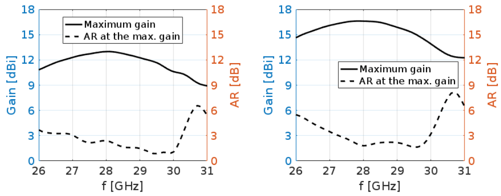

(a) (b)

Fig. 10. Axial ratio and maximum gain vs. frequency for (a) talk mode – bottom antenna location and (b) talk mode – top antenna location when the relative phase shift between antenna elements is 0°.

B. AR Beamwidth

The AR and maximum gain are plotted vs. scan angle in Fig. 11. The AR beamwidth of the array in talk mode – bottom location in Fig. 11(a) is around 55° from ϕ = 155 to 210°. Additionally, the gain for scan angles larger than ±35° (with respect to the boresight (180°)) is over 4 dB lower than that in the free space. The AR and maximum gain for the top antenna location are plotted vs. scan angle in Fig. 11(b). The AR beamwidth is around 40°. The maximum gain in the range from 150 to 190° is 2 dB higher than that in the free space.

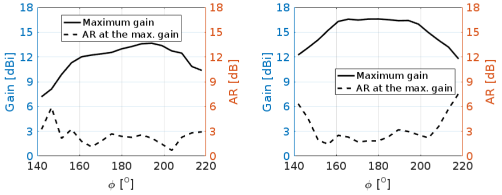

(a) (b)

Fig. 11. Axial ratio and maximum gain at 28 GHz vs. scan angle ϕ for (a) talk mode – bottom antenna location and (b) talk mode – top antenna location.

C. Total Scan Pattern

Regular and CP TSPs for the array top and bottom locations in the talk mode are shown in Fig. 12. The shadowing area created by the user's head and hand appears in all the TSPs. The regular TSP for the bottom antenna location in Fig. 12(a) is weaker than the one produced by the antenna in the free space in Fig. 4(a). However, the CP TSP for the same user setup in Fig. 12(b) is similar to the one in the free space in Fig. 4(b). Thus, the user has relatively less impact on the array CP performance when the bottom location is chosen.

When the array is located on the top edge, the shadowing occurs in the region from $\theta = 0$ to 60°. The regular TSP in Fig. 12(c) is around 2 dB stronger when $\theta = 110°$ and $\phi = 180°$ and has a different shape from the TSP in the free space in Fig. 4(a). Circular polarization only occurs in the small area around $\theta = 100°$ and $\phi = 180°$ in Fig. 12(d).

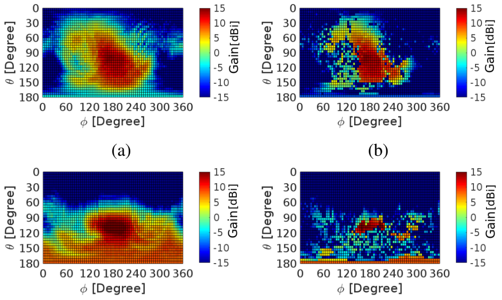

(a) (b)

(c) (d)

Fig. 12. Total scan patterns for talk mode at 28 GHz for (a) antenna on bottom – regular TSP, (b) antenna on bottom – CP TSP, (c) antenna on top – regular TSP, and (d) antenna on top – CP TSP.

D. Coverage Efficiency

Regular and CP coverage efficiency curves are shown in Fig. 5. CP coverage efficiency is calculated from the CP total scan pattern using Equation 2. The regular coverage efficiency is calculated using Equation 1. It can be observed that regular coverage efficiency has very similar values for both top and bottom positions. However, the CP coverage efficiency for the threshold gain lower than 8 dBi is 10 to 15 % higher for the bottom position than for the top position.

V. DATA MODE SIMULATIONS

In this section, the simulations of the phased array are completed in data mode with the whole-body phantom described in Section III. The chosen gestures are shown in Figure 13. In data mode, the user holds the mobile phone in front of the eyes with one hand. The angles used in this phantom setup are in the comfortable zone of a user as described in [13]. The distance between the head and the mobile device is approximately 28 cm. The coordinate system is always similar with respect to the mobile device ground plane to compare the array's total scan patterns simulated with user effects and in the free space. The simulations are performed with CST Microwave Studio with an FDTD solver and over 600 million mesh cells. The smallest cell size is 0.1 mm, and the largest cell size is 1.8 mm. A frequency range from 26 to 31 GHz is used.

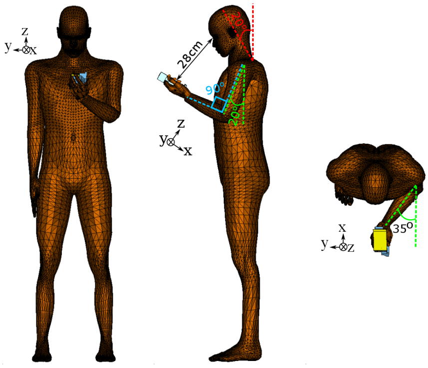

(a) (b) (c)

Fig. 13. Simulation setup in data mode with a homogeneous whole-body phantom shown in (a) front view, (b) side view, and (c) top view.

A. AR Bandwidth

The AR and maximum gain are plotted in Fig. 14 for the bottom and top antenna locations in data mode. For the top antenna location in Fig. 14(a) the AR bandwidth is 3 GHz (10.71 %), which is 1 GHz smaller than that in the free space. Maximum gain on average resembles the free-space case. The AR and maximum gain are plotted in Fig. 14(b) for the bottom antenna location. The AR in the band for the bottom antenna position is worse than 18 dB and, thus, is not visible in the figure. In this case, the array is pointed towards the user, and the main beam is blocked by the user.

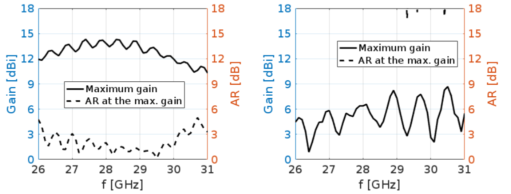

(a) (b)

Fig. 14. Axial ratio and maximum gain vs. frequency for (a) data mode – top antenna location and (b) data mode – bottom antenna location when the relative phase shift between antenna elements is 0°.

B. AR Beamwidth

The AR and maximum gain are plotted vs. scan angle in Fig. 15. For the array top location, the AR beamwidth of 20° is observed in Fig. 15(a). However, the AR is also lower than 3 dB when ϕ = 200° and ϕ = 160°. The maximum gain is comparable to the gain in the free space. The AR and maximum gain in data mode with the bottom location are plotted vs. scan angle in Fig. 15(b).The AR curve can never reach 3 dB and the maximum gain is lower than 0 dBi.

C. Total Scan Pattern

Regular and CP TSPs for the antenna array at the top and bottom locations in data mode are shown in Fig. 16. The regular TSP for the top antenna location is given in Fig. 16(a), which approximates the result in the free-space case shown in Fig. 4(a). The only difference is the presence of a shadow at ϕ = 0 and ϕ = 360°. Furthermore, the CP TSP in Fig. 16(b) is nearly identical to the one in the free space in Fig. 4(b). Thus, the user's hand and the body have virtually no impact on the antenna array CP performance when the array is located on the top. The TSP is plotted in Fig. 16(c) and Fig. 16(d) for the bottom antenna location. The shadow from the phantom is extremely strong, and only a small portion of the total is diffracted around the user. Furthermore, CP antenna performance is nonexistent when the antenna is located on the bottom.

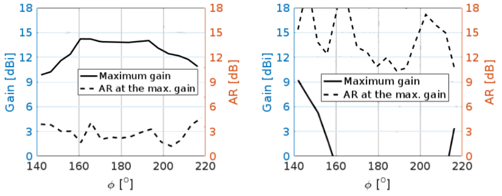

(a) (b)

Fig. 15. Axial ratio and maximum gain vs. ϕ scan angle at 28 GHz for (a) data mode – top antenna location and (b) data mode – bottom antenna location.

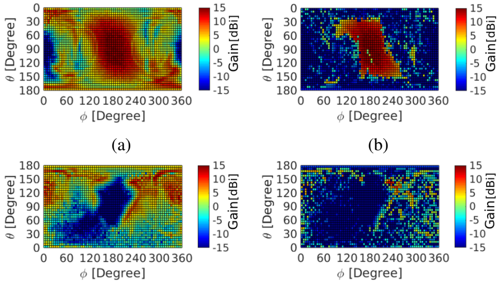

(a) (b) (c) (d)

Fig. 16. Total scan patterns in data mode at 28 GHz for the (a) antenna array on top – regular TSP, (b) antenna array on top – CP TSP, (c) antenna array on bottom – regular TSP, and (d) antenna array on bottom – CP TSP.

D. Coverage Efficiency

Fig. 17 shows the comparison of the coverage efficiency in data mode and in the free space. The CP curves for the free-space and top antenna locations have similar coverage for the threshold gain from 3 to 9 dBi. The CP coverage of the array in the bottom location is less than 10 % for gain from 0 to 7 dBi. All the curves for the CP coverage efficiency are similar below the threshold gain value of -5 dBi.

VI. COMPARISON

Comparisons between various simulated antenna parameters are shown in this section. The comparison of the AR bandwidth and AR beamwidth is summarized in Table II. In all cases, a significant loss in AR bandwidth was observed when the array is held by the user. However, AR beamwidths of similar value were achieved in talk mode – bottom location. For the other setups, the AR values are higher than 3 dB and can been observed for the different scan angles because of the user proximity. The CP array cannot be used in the data mode – bottom antenna location because of blockage by the user. In all cases, shadowing is mainly induced by the user's head and body. Furthermore, the user's arm and hand partially contribute

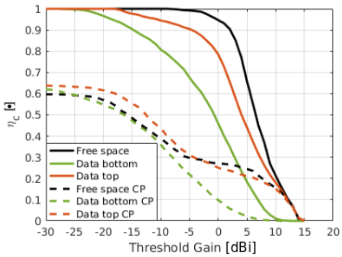

Fig. 17. Comparison of the regular coverage efficiency and CP coverage efficiency between the free space and data mode.

to the shadowing. However, in data mode, the shadowing from the head is small in comparison with the body shadowing. On the other hand, in talk mode, the main shadowing source is the user's head.

Table II. AR bandwidth and AR beamwidth and coverage efficiency at 28 GHz for different simulation setups.

Setup	AR bandwidth	AR beamwidth
Free space	4 GHz	55°
Talk mode – top	2.7 MHz	40°
Talk mode – bottom	3.2 GHz	55°
Data mode – top	3 GHz	20°
Data mode –bottom	None	None

The comparison of the coverage efficiency is shown in Fig. 18(a). The solid lines show regular coverage efficiency, and the dashed lines show CP coverage efficiency. As expected, the best regular coverage can be achieved by using the antenna array in the data mode - top location. All other regular coverage efficiency curves have a spread of a minimum of 10 dB. For the threshold gain $\leq$ -5 dBi all of the CP coverage efficiencies have a similar level except for talk mode – top location. For the threshold gain higher than -5 dBi, the curves for the data – top and talk-bottom have very similar coverage. The CP coverage performance of the array in talk-top and data-bottom locations has a similar shape but 5 to 15 % less coverage compared to the data top and talk bottom positions. Furthermore, the CP coverage efficiency curves are 15 to 25 % lower than the free-space curves for the threshold gain lower than 0 dBi. Coverage efficiency curves for the talk bottom and data top positions are plotted in dB in Fig. 18(b) to demonstrate the relative difference between the user and free space cases. In the region ($\leq$ 7 dBi), CP coverage efficiency is relatively less sensitive to user effects.

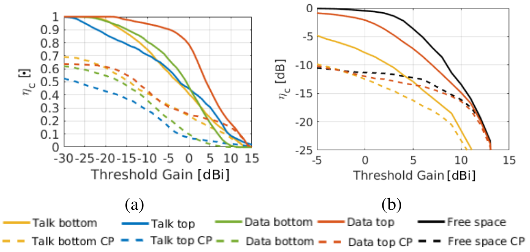

(a)

(b)

Fig. 18. Comparison of the regular coverage efficiency and CP coverage efficiency for free space, talk mode and data mode plotted (a) in numbers and (b) in dB.

VII. Conclusion

In this paper, user effects on a circular polarized phased array were studied for 5G mobile terminal applications. Two figures of merit have been introduced: the CP total scan pattern and CP coverage efficiency. The user effects on the CP performance of a mobile phased array were studied with the two defined parameters. The CP phased array was studied in talk mode (according to CTIA standards) and in data mode (with the CTIA hand and a homogeneous whole-body phantom). The antenna array was placed at the bottom and top locations on the mobile device ground plane. Circular polarization was relatively more robust to user impact than linear polarization if an array is placed in the right position of the ground plane. To realize the optimal CP performance with user effects in the talk mode, a CP phased array should be placed at the bottom short edge location, while in the data mode, the top short edge location should be used. As a result, the two phased antenna arrays should be placed on the top and bottom edge of the mobile device for optimal antenna performance.

References

[1] T. S. Rappaport, S. Sun, R. Mayzus, H. Zhao, Y. Azar, K. Wang, G. N. Wong, J. K. Schulz, M. Samimi, and F. Gutierrez, "Millimeter wave mobile communications for 5G cellular: it will work!," *IEEE Access*, vol. 1, pp. 335–349, 2013.

[2] J. Helander, K. Zhao, Z. Ying, and D. Sjöberg, "Performance analysis of millimeter-wave phased array antennas in cellular handsets," *IEEE Antenna Wireless Propag. Lett.*, vol. 15, pp. 504–507, 2016.

[3] S. Zhang, X. Chen, I. Syrytsin, and G. F. Pedersen, "A planar switchable 3D-coverage phased array antenna and its user effects for 28 GHz mobile terminal applications," *IEEE Trans. Antennas Propag.*, 2017 (in press).

[4] T. Manabe, Y. Miura, and T. Ihara, "Effects of antenna directivity and polarization on indoor multipath propagation characteristics at 60 GHz," *IEEE J. Sel. Areas Commun.*, vol. 14, pp. 441–448, Apr 1996.

[5] J. O. Nielsen and G. F. Pedersen, "Dual-polarized indoor propagation at 26 GHz," in *2016 IEEE 27th Annual International Symposium on Personal, Indoor, and Mobile Radio Communications (PIMRC)*, pp. 1–6, Sept 2016.

[6] J. Krogerus, J. Toivanen, C. Icheln, and P. Vainikainen, "User effect on total radiated power and 3-D radiation pattern of mobile handsets," *Antennas and Propagation, 2006. EuCAP 2006. First European Conference on*, pp. 1–6, Nov 2006.

[7] I. Syrytsin, S. Zhang, G. F. Pedersen, K. Zhao, T. Bolin, and Z. Ying, "Statistical investigation of the user effects on mobile terminal antennas for 5G applications," *IEEE Trans. Antennas Propag.*, 2017 (in press).

[8] I. Syrytsin, S. Zhang, and G. F. Pedersen, "Performance investigation of a mobile terminal phased array with user effects at 3.5 GHz for LTE advanced," *IEEE Antenna Wireless Propag. Lett.*, vol. 16, pp. 226–229, 2017.

[9] K. Zhao, J. Helander, D. Sjoberg, S. He, T. Bolin, and Z. Ying, "User body effect on phased array in user equipment for 5G mm wave communication system," *IEEE Antenna Wireless Propag. Lett.*, vol. 16, pp. 864–867, 2017.

[10] W. H. Zhang, W. J. Lu, and K. W. Tam, "A planar end-fire circularly polarized complementary antenna with beam in parallel with its plane," *IEEE Trans. Antennas Propag.*, vol. 64, pp. 1146–1152, Mar. 2016.

[11] M. You, W. J. Lu, B. Xue, L. Zhu, and H. B. Zhu, "A novel planar endfire circularly polarized antenna with wide axial-ratio beamwidth and wide impedance bandwidth," *IEEE Trans. Antennas Propag.*, vol. 64, pp. 4554–4559, Oct. 2016.

[12] C. Gabriel, S. Gabriel, and E. Corthout, "The dielectric properties of biological tissues: I. literature survey," *Phys. Med. Biol.*, vol. 41, pp. 2231–2249, 1996.

[13] J. Panero and M. Zelnik, *Human Dimension and Interior Space: A Source Book of Design Reference Standards.* Watson-Guptill, 1979.

[14] Health Examination Survey, The National Health and Nutrition Examination Surveys, and The Hispanic Health and Nutrition Examination Survey, *Anthropometric Reference Data for Children and Adults: United States, 2007–2010.* U.S. Government Printing Office, 2012.

[15] C. Telecommunications and I. A. (CTIA), "Test plan for wireless device over-the-air performance," *Revision Number 3.6.1*, November 2016.

[16] H. C. Burger and R. van Dongen, "Specific resistance of body tissues," *Phys. Med. Biol.*, vol. 5, no. 4, pp. 431–447, 1961.

[17] S. S. Zhekov, A. Tatomirescu, and G. F. Pedersen, “Antenna for ultrawideband channel sounding,” *IEEE Antenna Wireless Propag. Lett.*, vol. 16, pp. 692–695, 2017.

Paper C

User Impact on Phased and Switch Diversity Arrays in 5G Mobile Terminals

Igor Syrytsin, Shuai Zhang, Gert Frølund Pedersen

The paper has been published in:
IEEE Access, Vol. 6, pp. 1616-1623, 2018.

Abstract

In this paper, a mobile terminal phased array at 28 GHz with different scan angles is compared to a switch diversity antenna array at 28 GHz in the case of antenna beams pointing at the user's body. In the switch diversity antenna array, there is only one element out of eight operating each time. The study is carried out in data mode with a standing user, which includes both body blockage and user hand effects. The metrics of coverage efficiency, antenna shadowing power ratio and isotropic antenna shadowing power ratio are utilized in the investigation. It is found that the scan angle of a phased array higher than 90° is not necessary for this scenario because the user body will contribute to the total radiation at large angles by scattering the radiated energy around the body. For the linear phased antenna arrays on the edge of the mobile device ground plane it can be concluded that in order to achieve the highest coverage efficiency and lowest user shadowing it is more beneficial to use a phased array instead of a switch diversity array. However, if the losses of the phase shifters and the feeding network from the phased array are higher than 5 dB, the switch array can be used, which will also decrease the complexity of a system.

DOI:

https://ieeexplore.ieee.org/document/8166731

User Impact on Phased and Switch Diversity Arrays in 5G Mobile Terminals

Igor Syrytsin, Shuai Zhang, Gert Frølund Pedersen

***Abstract*—In this paper, a mobile terminal phased array at 28 GHz with different scan angles is compared to a switch diversity antenna array at 28 GHz in the case of antenna beams pointing at the user's body. In the switch diversity antenna array, there is only one element out of eight operating each time. The study is carried out in data mode with a standing user, which includes both body blockage and user hand effects. The metrics of coverage efficiency, antenna shadowing power ratio and isotropic antenna shadowing power ratio are utilized in the investigation. It is found that the scan angle of a phased array higher than 90° is not necessary for this scenario because the user body will contribute to the total radiation at large angles by scattering the radiated energy around the body. For the linear phased antenna arrays on the edge of the mobile device ground plane it can be concluded that in order to achieve the highest coverage efficiency and lowest user shadowing it is more beneficial to use a phased array instead of a switch diversity array. However, if the losses of the phase shifters and the feeding network from the phased array are higher than 5 dB, the switch array can be used, which will also decrease the complexity of a system.**

***Index Terms*—Mobile Terminal Antenna, 5G antenna, user effects, human shadowing, SAPR, SIAPR, coverage efficiency.**

I. INTRODUCTION

BECAUSE of the recent technological development in the direction of the fifth generation communication system phased mobile antenna arrays have become a very active research topic. The 5G mm-wave mobile communication system will probably occupy bands in the range from 20 GHz to 40 GHz [1]. At the mm-wave frequencies, the path loss is much higher than at the GSM or LTE frequencies used today. As enabler technology for the 5G in [2], phased mobile arrays can achieve gains up to 10 dBi, and thus can counteract the high path loss at cm or mm-wave frequencies [3], [4]. However, to achieve the best spatial coverage performance, the phased array should be scanned. In order to do that, multiple phase shifters and feeding network are required. Phase shifters with large phase shifts are usually lossy, and thus, will decrease the overall performance of the system when large array scan angles are desired. If a switched diversity (SD) array or a phased array with small phase shift can be applied, the loss of phase shifters can be minimized.

The cellular mobile device can have an arbitrary location when used. The conventional LTE and GSM antennas have an omni-directional radiation pattern but in 5G mm-wave systems the directional antennas with beam agility will be used. Thus, the metric for describing the spatial coverage of the 5G antenna system is needed. The concept of coverage efficiency was introduced in [5]. Then, it has been applied in [6] to characterize 5G mm-wave antennas in mobile terminals and quantify the spatial performance. Furthermore, this metric also takes into account the randomness of the mobile terminal orientation when used by a human. Not only the high spatial coverage of the 5G phased antenna array is important but also the user effects on the performance of phased antenna arrays are a significant issue. Recently it has been found in [7] that human shadowing has a significant impact on the performance of the mobile phased arrays at cm/mm-wave frequencies. Not to mention, even at the GSM/LTE frequencies, a shadowing up to −20 dB from the user's head has been observed in [8]. Most interestingly, the body loss of the mobile antennas at the 28 GHz is insignificant in comparison to the power lost in the shadowing region as described in [9]. Contradictory to the GSM/LTE frequencies, not only the user's head but also a full user's body should be considered for the performance verification of a mobile terminal antenna at the cm/mm-wave frequencies. The performance of the phased antenna array will indeed be affected by the user. A small amount of 1 to 4 dB of absorption loss will be induced [9]. Yet, those numbers are very low in comparison to the GSM frequencies, where absorption loss of 10 to 15 dB has been measured. Furthermore, at the user's effect on the detuning of operating frequency of the cm/mm-wave antenna is not significant. However, the shadowing at the cm/mm-wave frequencies is more severe than at the GSM/LTE frequencies. Thus, coverage efficiency metric cannot be used alone to verify the performance of the mobile terminal with the user. In order to quantify the shadowing effect at 28 GHz in [9] it has been proposed to characterize the shadowing region by means of Shadowing Antenna Power Ratio (SAPR) and Shadowing Isotropic Antenna Power Ratio (SIAPR). Multiple investigations of the human shadowing have been already done for 60 GHz WLAN, but effects of the human hand and arm have not been considered. In [10] a statistical model for human body shadowing has been proposed, but the model does not include the human hand. And finally, in [11] shadowing dependence on the transmission distance and human position between antennas has been investigated at the frequencies up to 30 GHz. However, the user was positioned between the antennas, and not interacting with the mobile device directly. All things considered, a comparison between a phased mobile antenna array and an SD antenna array has not been studied in user case yet.

In this paper, a mobile phased array's and SD array's performance with the user in data mode will be investigated at 28 GHz by applying metrics of SAPR, SIAPR and coverage

---

This work was supported by the InnovationsFonden project of RANGE, and also partially supported by AAU Young Talent Program.(Corresponding author: Shuai Zhang).

Igor Syrytsin, Shuai Zhang, and Gert Frølund Pedersen are with the Antennas, Propagation and Radio Networking section at the Department of Electronic Systems, Aalborg University, Denmark (email: {igs,sz,gfp}@es.aau.dk).

efficiency. In this investigation, it has been chosen to look at the most challenging scenario from the spatial coverage perspective. In this scenario, the base station is located behind the user and the mobile phased array is pointing towards the user's body as shown in Fig. 1. In this scenario, the big shadowing area will be created by the user's body. Thus, it is very interesting to investigate if the phased/SD array can be used in order to reduce that shadowing area. The investigation is carried out by simulating monopole mobile phased array with wide scan angle in CST Microwave Studio FDTD solver. In simulations, a full-body phantom holding a mobile terminal in the left hand has been used. Furthermore, the switch diversity characteristics of the same array are investigated by simulations and measurements with the phantom/user.

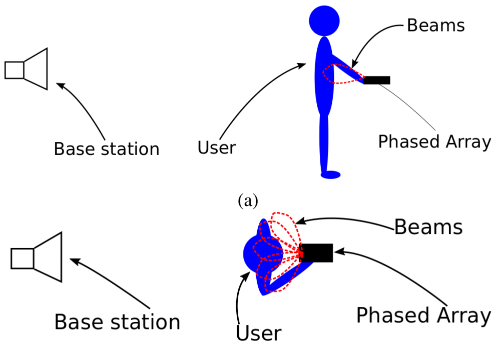

Fig. 1. The scenario where a base station is behind the user and mobile phased array pointing towards the user's body (a) side view and (b) top view.

II. Array Free Space Performance

In this paper, the same antenna array has been applied in two manners:

- As a phased array, where different weights are applied on each of the array element and then signals from all elements are summed together. In this study, only the phase has been applied as a weight (imitating real phase shifters in the application).
- As a switch diversity array, where only one antenna is used at a time. In the application, the 1P8T switch could be used for this purpose. One could expect diversity to be implemented through the usage of spatially separated antennas.

For the purpose of this investigation, it has been chosen to construct a simple monopole antenna array which is shown in Fig. 2. One piece of copper of 5 mm height has been added to the design in order to obtain the desired endfire radiation pattern, and suppress the surface wave. Because in the investigation, the wide scan angle of the phased antenna array is needed, the monopole array elements have been applied. The monopole array elements have an omnidirectional radiation pattern characteristics, which makes the perfect for this purpose. The monopole elements have a height of 1.9 mm and distance a between them is 5.5 mm($\lambda/2$).

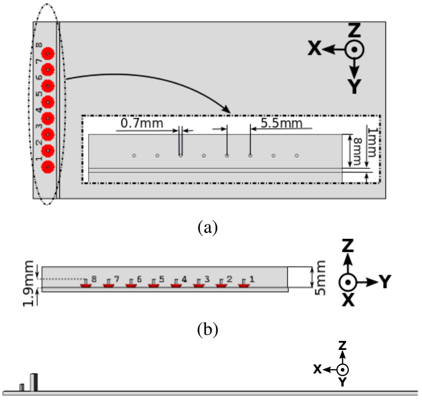

Fig. 2. Geometry of the proposed 28 GHz monopole array in (a) xy-plane, (b) yz-plane, and (c) xz-plane.

It has been selected to consider four different scan angles of the array. The chosen scan angles of 28°, 58° , 90° and 128° are illustrated in Fig. 3

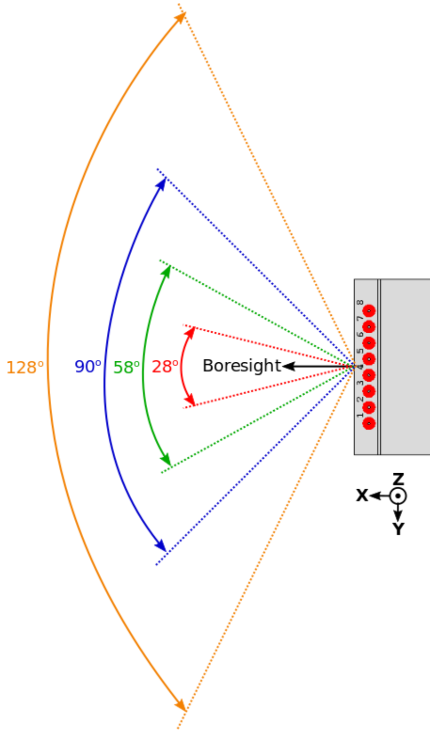

Fig. 3. Illustration of the four array's scan angles used in investigation.

In Fig. 4 the TSPs of the array with different scan angles.

This wide scan angle behavior is expected because each of the antenna elements have a radiation pattern with a wide main beam. Furthermore, the SD pattern of the antenna array is shown in Fig. 4(e). The SD pattern is calculated by switching among 8 available antennas, instead of using the phase shifters to change the beam direction of the phased array. The SD pattern of the proposed antenna array is considerably weaker.

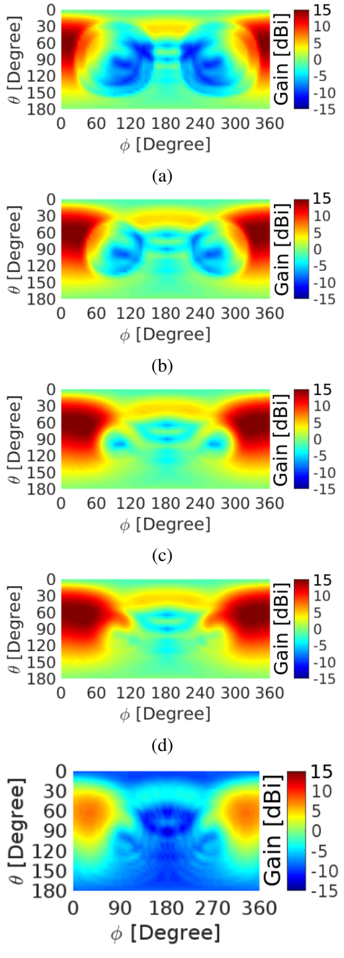

(a)

(b)

(c)

(d)

(e)

Fig. 4. Total scan patterns of the phased antenna array at 28 GHz in free space for (a) 28° scan angle, (b) 58° scan angle, (c) 90° scan angle, (d) 128° scan angle, and (e) SD pattern.

To investigate the spatial performance of the phased antenna array the coverage efficiency metric is used. Coverage efficiency is defined as [6]:

$$\eta_c = \frac{\text{Coverage Solid Angle}}{\text{Maximum Solid Angle}} \qquad (1)$$

where maximum solid angle defined as 4π steradians in order to account for the arbitrary angle of arrival and arbitrary orientation of the mobile device. The coverage efficiency is calculated from the total scan pattern with respect to the chosen set of the gain values. Here it has been chosen to use gain values ranging from -10 to 15 dBi.

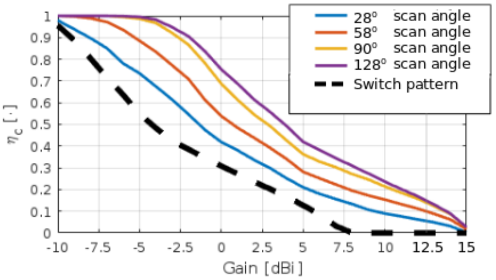

Fig. 5. Coverage efficiency of the proposed phased antenna array in free space.

The coverage efficiency of the proposed antenna array in free space is shown for all four chosen phase shift steps in Fig. 5. The coverage efficiency of SD pattern antenna array is also shown in Fig. 5. The difference in the coverage efficiency between blue, red and yellow curves is around 10 % at 0 dBi gain and becomes smaller as gain increases. The difference between the dashed curve for the SD pattern antenna array and the worst of the phased antenna array curves is 5 % for the gain range from 0 dBi to 7.5 dBi. It can clearly be seen that phased antenna array is much more efficient than the SD pattern array in free space.

III. USER IMPACT

In this section, the performance of the phased array with different scan angles and the SD antenna array will be investigated with the human phantom in data mode. The simulation setup with the phantom is shown in Fig. 6. It is important to notice that it is difficult to make the user sit/stand still for a prolonged period of measurement time. The errors due to user movement will lead to the phase instability in the measurement. The beamforming cannot be performed correctly when the measured radiation patterns have an incorrect phase, however when measuring the SD array the phase errors are not important because only magnitude of the radiation pattern is of interest. Thus, the simulations of the phased array are more reliable than the measurements. At this current moment, no standards for human gestures have been defined for cm/mm-wave 5G mobile terminals. Thus, it has been chosen to use the proposed full-body realistic phantom [12] and simulate it in CST Microwave Studio FDTD solver. The length of the limbs, body circumference and weight of the phantom has been based on the average values for human male, defined in [13] and [14]. The hand gesture of the phantom complies with the CTIA standards for data mode [15]. The dimensions of the phantom can be found in Table I.

The homogeneous full-body male phantom is made of skin tissue with real and imaginary parts of $\varepsilon_r = 16.5 + j16.5$. The parameters of different tissues up to 100 GHz have been measured in [16]. A homogeneous model has been used because at the 28 GHz the waves will not penetrate deep into human tissue. For instance, the skin depth at 28 GHz can be calculated to 1.158 mm if a resistivity of the human tissue of 245 Ωcm [17] has been used in calculations.

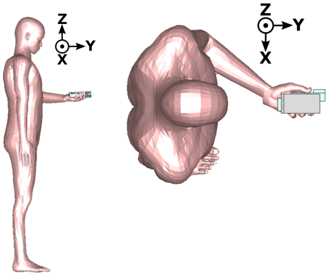

(a) (b)

Fig. 6. Simulation setup with the human phantom in (a) side view and (b) top view.

Table I. Dimensions of the phantom and the measured user.

Category	Phantom	User
Height	175.6 cm	174 cm
Neck circumference	42.8 cm	43 cm
Upper arm length	25 cm	24 cm
Upper arm circumference	27.8 cm	32 cm
Lower arm length	27 cm	27.7 cm
Wrist circumference	15 cm	16 cm
Chest circumference	108 cm	111 cm
Waist circumference	89 cm	86 cm
Hip circumference	101 cm	97 cm
Upper leg length	40 cm	40 cm
Lower leg length	50 cm	45 cm
Ankle circumference	22 cm	22 cm

A. Phased Antenna Array

The simulated total scan patterns of the phased antenna array with the human phantom are shown in Fig. 7. It can clearly be seen that more space around the user can be covered if larger scan angle of the antenna array is used, but the power in the shadowing area almost remains the same.

The dependency of the scan angle of a phased array on shadowing antenna power ratio (SAPR), shadowing isotropic antenna power ratio (SIAPR), and coverage efficiency is also investigated, which is shown in Fig. 8. The SAPR and SIAPR are defined as [9]:

$$SAPR(\Delta\theta,\Delta\phi) \triangleq \frac{P_{shadow\ in\ the\ window}(\Delta\theta,\Delta\phi)}{P_{total}} \tag{2}$$

$$SIAPR(\Delta\theta,\Delta\phi) \triangleq \frac{P_{shadow\ in\ the\ window}(\Delta\theta,\Delta\phi)}{P_{isotropic}} \tag{3}$$

where:

- $\Delta\theta$ is the window size in θ
- $\Delta\phi$ is the window size in ϕ
- $P_{shadow\ in\ the\ window}(\Delta\theta,\Delta\phi)$ is the power in the window of the chosen size.
- P_{total} is the total radiated power (TRP) of the antenna.
- $P_{isotropic}$ is the total radiated power of the isotropic antenna if transmit power is 0 dB.

The SAPR and SIAPR metrics describe how much the power in the shadowing area is lower than the TRP of the reference antenna. The SAPR parameter depends on the antenna design, because the TRP of the chosen antenna is used. The TRP will vary, depending of the antenna efficiency. However, the SIAPR parameter is not antenna specific because the TRP of the isotropic antenna is used in the equation, which is constant.

In this paper, the $\Delta\theta$ window width is constant and chosen to the maximum of 180° (or 140° because of the measurement system constraints) because the shadowing from the user's body spans along the full range of the elevation plane. Then, SAPR and SIAPR are calculated for the $\Delta\phi$ values from 1 to 90°. In Fig. 8(a) the difference in the SAPR for the phased antenna array performing with different scan angles is very small. It occurred because SAPR metric uses total power as a reference, where total power is not constant. This means that power in the shadow does not change with respect to the total power. However, the SIAPR in Fig. 8(b) have different values for the window sizes larger than $\theta = 30°$. The difference of 2.5 dB can be observed for the window sizes

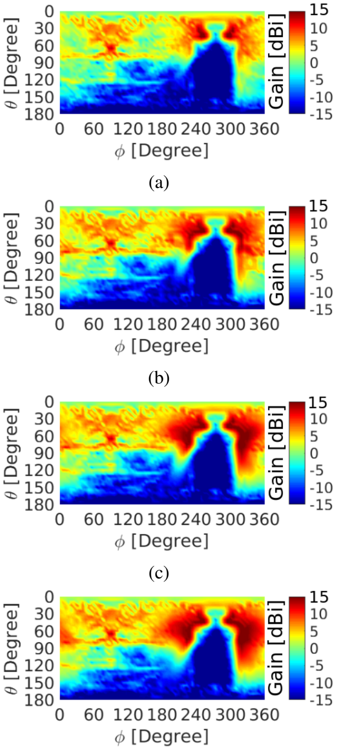

(a)

(b)

(c)

(d)

Fig. 7. Simulated at 28 GHz total scan patterns of the phased antenna array with the user with (a) 28° scan angle, (b) 58° scan angle, (c) 90° scan angle, (d) 128° scan angle.

larger than $\theta = 30°$. Furthermore, there is no difference in the performance of the antenna arrays with 90° and 128° scan angles. The difference in the coverage efficiency is very small for the phased antenna arrays with 58°, 90°, and 128° scan angles due to scattering by the user's body.

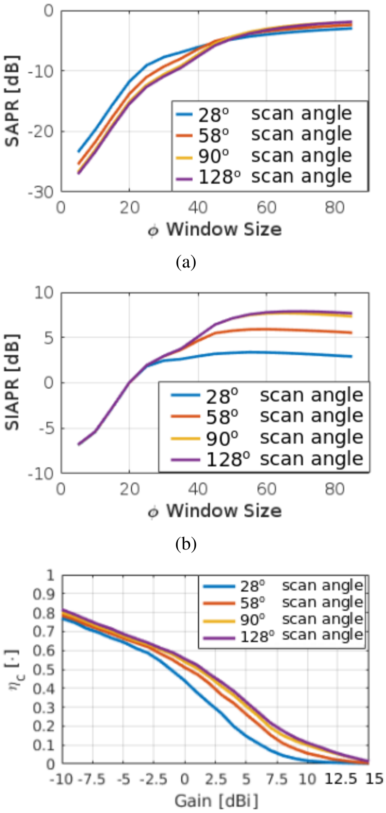

(a)

(b)

(c)

Fig. 8. Plots of (a) SAPR, (b) SIAPR, and (c) coverage efficiency of the phased antenna array with the user at 28 GHz

B. Switch Diversity Antenna Array

In this subsection, the SD antenna array performance is measured and simulated by using the same setup, described in Sec. III-A. The simulations have been done in CST Microwave Studio using the time domain solver. The 876 million mesh cells have been used in the simulation. The smallest mesh cell size is 0.044 mm and the biggest mesh cell size is 0.856 mm. The mesh is denser in the locations where the currents are strong. On the other hand, the measurements have been done in the anechoic chamber with a single dual-polarized probe antenna. The resolution of 14° in the elevation plane and 2° in azimuth plane has been chosen. The coarse resolution in the elevation plane has been chosen in order to reduce the measurement time. Shorter measurement time will ensure that the person under the test can stand still without significant discomfort. Because of the measurement system limitations, only the elevation angles up to 140° could be measured. The 10 frequency points have been measured for each position of the probe antenna, however only results at 28 GHz have been presented in this paper. However, a real human specimen has been used in the measurement instead of a phantom. The dimensions of the human under test is shown in Table I. Actually, many of the major dimensions of the human and phantom are similar. Furthermore, the simulations and measurements of the SD array are compared to the phased array in this section. The phased array antenna performance has not been measured with the user because the phase is unstable in the proposed measurement setup with available measuring equipment. To verify the simulated results, the prototype of the mobile phased monopole antenna array has been constructed. The geometry of the prototype is shown in Fig.9. No feeding network has been constructed, and instead, each of the monopoles has its own cable of the same length.

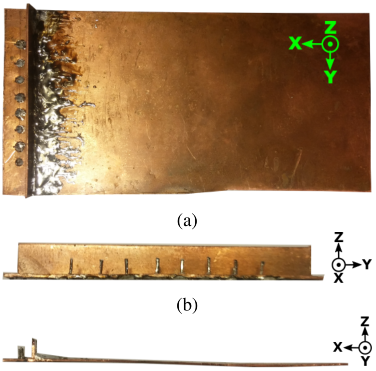

(a)

(b)

(c)

Fig. 9. Geometry of monopole antenna array prototype in (a) xy-plane, (b) yz-view, and (c) xz view.

First, the antenna array prototype has been measured in the free space, as shown in Fig. 10(a), and then it has been measured with the user, as shown in Fig. 10(b). For the free space case the coordinate system is different from the simulations because the prototype has been rotated in order to get easier access to the cables. All of the measurements have been done in the anechoic chamber. The user has similar height as the phantom, but different build. Furthermore, the effects of the clothes have not been included in the simulations.

Then, it has been chosen to compare the radiation patterns of the simulated and measured antennas in the free space. The comparison of the measured and simulated patterns of the center element 4 and the edge element 8 are shown in Fig. 11. The gain of the measured radiation patterns is on average 1 dB higher than the gain of the simulated radiation patterns. The edge element has a slightly different pattern than the center element, which is expected because of the edge effects.

Usually, the measurement will have inaccuracies such as movement of the user under the measurement, different phone

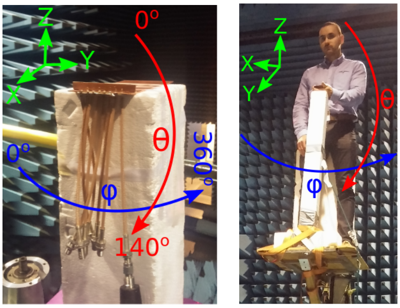

(a) (b)

Fig. 10. Measurement setup in (a) free space and (b) with the user.

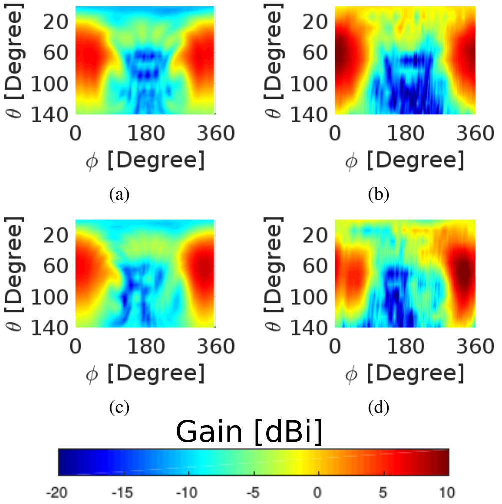

(a) (b)

(c) (d)

Fig. 11. Radiation patterns of (a) simulated element 4, (b) measured element 4, (c) simulated element 8, and (d) measured element 8 at 28 GHz.

grip, random effect of clothing. Furthermore, the phase is very challenging to control accurately at 28 GHz when measurements are done with the user. Even a small user movement will result in the phase error in the order of hundreds of degrees. Thus, the beamforming cannot be performed if the phase stability requirement is not satisfied. Because of the phase stability issue, only the measured SD patterns are considered in this section. The total SD patterns of the simulated and measured with the user antenna arrays are shown in Fig. 12. The measured total SD pattern is more noisy and less power is present on the right side of the user ($\phi = 330°$), because of the user's grip difference. However, the user's shape is still visible at $\phi = 270°$.

Finally, to investigate the performance difference of the simulated and measured antenna arrays with the user, it has been chosen to calculate coverage efficiency (Fig 13(a)), SAPR (Fig. 13(b)), and SIAPR (Fig. 13(c)). In all of the figures,

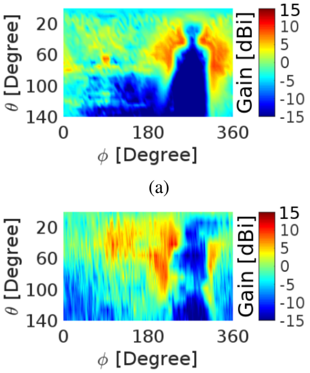

(a)

(b)

Fig. 12. Total SD pattern of (a) simulated antenna array and (b) measured antenna array.

the simulation results follow the measurements very well. It has been chosen to compare the switch diversity array to the phased array low scan angle of 28° because the highest SAPR and similar SIAPR for all of the scan angles of the phased antenna array can be observed for the small window sizes (Fig. 8(a) and Fig. 8(a)). The curve for the low phased array scan angle of 28° has also been added to the figures of coverage efficiency, SAPR, and SIAPR in Fig. 13. The difference between the coverage efficiency curves for the switchable pattern array and phased array with 28° scan angle is on average 5 to 10 % in Fig. 13(a). The difference in coverage efficiency decrease for the high gains ≥ 7.5 dBi. In Fig. 13(b) the SAPR difference between phased array with 28° scan angle and switchable pattern array is around 5 dB for the window sizes less than 30°. The SIAPR of the phased array with the scan angle of 28° is 5 dB higher than SIAPR of SD array for window sizes less than 40°.

IV. CONCLUSION

In this paper, the switch diversity antenna array has been compared to the phased mobile antenna array with different scan angles by simulating and measuring in free space and with a standing user in data mode. The investigation has been done at 28 GHz. For the linear endfire phased arrays on the short edge of the ground plane it can be concluded that in order to achieve the highest coverage efficiency and lowest user shadowing it is always more beneficial to use phased array than the switched pattern antenna array. However, this is concluded based on the assumption that the combined losses of the phase shifters and feeding network is less than 5 dB.

The increase in coverage efficiency of up to 30 % at the gain of 7.5 dBi in the free space can be achieved if the phased array with a scan angle bigger than 90° in comparison to the switch diversity array. The increase in coverage efficiency of up to 20 % at the gain of 7.5 dBi is expected when the antenna array is used by the user in data mode. However, scan angles bigger than 90° does not increase the coverage performance dramatically. The SAPR and SIAPR for the window sizes less than 30° are very similar for all of the chosen scan angles.

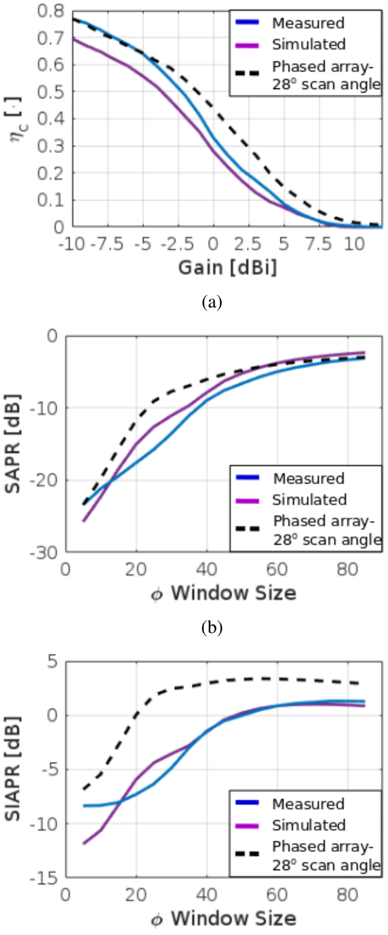

(a)

(b)

(c)

Fig. 13. Plots of (a) total SD pattern of the array, (b) SAPR, and (c) SIAPR of the SD antenna array with the user.

In this case, most of the energy radiating from the antenna is blocked and only a small portion of the energy is scattered around the body.

The SAPR is on average 5 dB and SIAPR is 5 to 7 dB lower for the switch diversity antenna array than the phased antenna array. In practice, if the losses of the phase shifters and feeding network is higher than 5 dB the switch diversity antenna array can be used in the studied scenario, which will also decrease the complexity of a system.

Finally, it can be noticed that the results may change with both antenna array location, radiation pattern direction (broadside or endfire) and body position (position of the mobile terminal with respect to the user's body). Nonetheless, the orientation of the mobile can still be very random. Such factors as hand grip (two hands - horizontal orientation , one hand horizontal orientation, one hand vertical orientation, etc.), different angle of the arm, and distance from the antenna to the body will influence the size of the shadowing region and performance of the phased antenna array system. However the conclusion of the paper is still very useful and meaningful because user's body will always scatter the field and contribute to the total radiation of antenna. Thus, large scan angle of the phased array is not always beneficial in order to obtain the good coverage efficiency. Furthermore, because the phased array and and SD array using the same array configuration and elements, so even if the conditions (antenna pattern, type, body location, etc.) may change the relative relations in the shadowed region between SD and phased array will be similar.

REFERENCES

[1] T. S. Rappaport, S. Sun, R. Mayzus, H. Zhao, Y. Azar, K. Wang, G. N. Wong, J. K. Schulz, M. Samimi, and F. Gutierrez, "Millimeter wave mobile communications for 5G cellular: It will work!," *IEEE Access*, vol. 1, pp. 335–349, 2013.

[2] W. Roh, J. Y. Seol, J. Park, B. Lee, J. Lee, Y. Kim, J. Cho, K. Cheun, and F. Aryanfar, "Millimeter-wave beamforming as an enabling technology for 5G cellular communications: theoretical feasibility and prototype results," *IEEE Commun. Mag.*, vol. 52, pp. 106–113, feb 2014.

[3] N. Ojaroudiparchin, M. Shen, S. Zhang, and G. F. Pedersen, "A switchable 3-d-coverage-phased array antenna package for 5g mobile terminals," *IEEE Antennas and Wireless Propag. Lett.*, vol. 15, pp. 1747–1750, 2016.

[4] S. Zhang, X. Chen, I. Syrytsin, and G. F. Pedersen, "A planar switchable 3D-coverage phased array antenna and its user effects for 28 GHz mobile terminal applications," *IEEE Trans. Antennas Propag.*, vol. 65, pp. 6413 – 6421, 2017.

[5] M. U. Rehman, X. Chen, C. G. Parini, and Z. Ying, "Evaluation of a statistical model for the characterization of multipath affecting mobile terminal GPS antennas in sub-urban areas," *IEEE Trans. Antennas Propag.*, vol. 60, pp. 1084–1094, Feb 2012.

[6] J. Helander, K. Zhao, Z. Ying, and D. Sjöberg, "Performance analysis of millimeter-wave phased array antennas in cellular handsets," *IEEE Antennas Wireless Propag. Lett*, vol. 15, pp. 504–507, 2016.

[7] K. Zhao, J. Helander, D. Sjoberg, S. He, T. Bolin, and Z. Ying, "User body effect on phased array in user equipment for 5G mm wave communication system," *IEEE Antennas Wireless Propag. Lett*, vol. 16, 2017.

[8] J. B. Andersen, J. O. Nielsen, and G. F. Pedersen, "Absorption related to hand-held devices in data mode," *IEEE Transactions on Electromagnetic Compatibility*, vol. 58, pp. 47–53, Feb 2016.

[9] I. Syrytsin, S. Zhang, G. F. Pedersen, K. Zhao, T. Bolin, and Z. Ying, "Statistical investigation of the user effects on mobile terminal antennas for 5G applications," *IEEE Trans. Antennas Propag.*, vol. 65, pp. 6596 – 6605, 2017.

[10] S. Obayashi and J. Zander, "A body-shadowing model for indoor radio communication environments," *IEEE Trans. Antennas Propag.*, vol. 46, pp. 920–927, Jun 1998.

[11] N. Tran, T. Imai, and Y. Okumura, "Study on characteristics of human body shadowing in high frequency bands: Radio wave propagation technology for future radio access and mobile optical networks," *2014 IEEE 80th Vehicular Technology Conference (VTC2014-Fall)*, pp. 1–5, 2014.

[12] I. Syrytsin, S. Zhang, G. F. Pedersen, and Z. Ying, "User effects on circular polarization of 5G mobile terminal antennas," *IEEE Trans. Antennas Propag.*, 2017 (Submitted).

[13] J. Panero and M. Zelnik, *Human dimension and interior space: A source book of design reference standards*. Watson-Guptill, 1979.

[14] Health Examination Survey, The National Health and Nutrition Examination Surveys, and The Hispanic Health and Nutrition Examination Survey, *Anthropometric reference data for children and adults: United States, 2007–2010.* U.S. Government Printing Office, 2012.

[15] C. Telecommunications and I. A. (CTIA), "Test plan for wireless device over-the-air performance," *Revision Number 3.6.1*, Nov. 2016.

[16] C. Gabriel, S. Gabriel, and E. Corthout, "The dielectric properties of biological tissues: I. literature survey," *Phys. Med. Biol.*, vol. 41, p. 2231–2249, 1996.

[17] H. C. Burger and R. van Dongen, "Specific resistance of body tissues," *Phys. Med. Biol.*, vol. 5, no. 4, pp. 431–447, 1961.

Paper D

Compact Quad-Mode Planar Phased Array with Wideband for 5G Mobile Terminals

Igor Syrytsin, Shuai Zhang, Gert Frølund Pedersen, and and Art Morris

The paper has been published in:
IEEE Transactions on Antennas and Propagation, Vol. 66, Issue 9, pp. 4648-4657, 2018.

Abstract

In this paper a quad-mode endfire planar phased antenna array with wide scan angle and 1.2 mm clearance is proposed for 5G mobile terminals. The proposed antenna can obtain over 8 GHz of impedance bandwidth. Here is suggested to efficiently combine a multi-mode array element with different radiation patterns for each mode into a phased antenna array. In the array, similar and wide embedded radiation patterns are obtained for the all four modes. Furthermore, a coaxial to differential stripline transition is designed in this work. The differential feeding structure is very compact and utilizes only MMPX connector and vias. The total scan pattern and coverage efficiency of the measured and simulated phased array antenna are calculated in the range from 25 to 33 GHz, and a good agreement between measured and simulated results is observed. The mean coverage efficiency along the frequency range is very similar, but minor difference in variance of coverage efficiency is observed in the measurements. The coverage efficiency of around 50 % for the threshold gain of 5 dBi is achieved in the chosen frequency range.

DOI:

https://ieeexplore.ieee.org/document/8370121

Compact Quad-Mode Planar Phased Array with Wideband for 5G Mobile Terminals

Igor Syrytsin, Shuai Zhang, Gert Frølund Pedersen, *Senior Member IEEE*, and Art Morris, *Fellow, IEEE*

***Abstract*—In this paper a quad-mode endfire planar phased antenna array with wide scan angle and 1.2 mm clearance is proposed for 5G mobile terminals. The proposed antenna can obtain over 8 GHz of impedance bandwidth. Here is suggested to efficiently combine a multi-mode array element with different radiation patterns for each mode into a phased antenna array. In the array, similar and wide embedded radiation patterns are obtained for the all four modes. Furthermore, a coaxial to differential stripline transition is designed in this work. The differential feeding structure is very compact and utilizes only MMPX connector and vias. The total scan pattern and coverage efficiency of the measured and simulated phased array antenna are calculated in the range from 25 to 33 GHz, and a good agreement between measured and simulated results is observed. The mean coverage efficiency along the frequency range is very similar, but minor difference in variance of coverage efficiency is observed in the measurements. The coverage efficiency of around 50 % for the threshold gain of 5 dBi is achieved in the chosen frequency range.**

***Index Terms*—Antennas, mobile handset antenna, radiation pattern, coverage efficiency, total scan pattern, 5G antenna, planar antenna, wideband antenna, 5G phased array.**

I. INTRODUCTION

IN the past few years, interests in the centimeter (cm) and millimeter (mm)-wave bands have grown [1]. In order to achieve communication speeds in GB/s the 28 GHz band has already been allocated by FCC for the future cellular communication systems. At the cm and mm-wave frequencies, higher free space path loss becomes a bigger design consideration for the link budgets. However, by using the directional high gain antennas the path loss can be compensated [2]. Furthermore, directional antennas can reduce doppler shift spread [3], reduce delay spread in wideband communication channels [4], and decrease the path loss exponent [5]. However, in the cellular communication systems the user mobility, urban indoor and outdoor propagation environments, and arbitrary mobile device orientation are some of the most important factors affecting the design of base and mobile station antennas. Thus, the beam steering should be implemented both at mobile and base stations to obtain the good link quality.

In order to verify the performance of the mobile device considering the arbitrary user equipment orientation the coverage efficiency metric has been proposed in [6]. This metric is especially useful in the characterization of the mobile phased antenna array's performance [7]. Multi-polarized antenna array configuration for mmWave 5G mobile terminals has been proposed in [8]. A low-profile beam steering antenna solution for future 5G cellular applications has been designed and analyzed in [9]. A Vivaldi phased antenna array has been studied with the user in [10]. Compact 4G MIMO antenna integrated with a 5G array has been designed and evaluated in [11]. In order to increase the coverage of the phased mobile antenna array, two different methods have been introduced in [12] and [13]. In [12] the 3D coverage has been realized by switching between 3 sub-arrays mounted on a folded 3D structure. On the other hand, in [13] the 3D coverage has been achieved by using a surface wave in order to change radiation pattern main beam directions of the three planar sub-arrays. The bandwidth of the shown antennas is not so big and the wider bandwidth is wanted in order to achieve higher data rates. Furthermore, the exact operating frequency and bandwidth of the 5G communication system is still unknown. The phased mobile antenna array with wide scan angle has been proposed in [14]. However, the antenna does not have a large bandwidth. The bow-tie phased antenna array in [15] has a wide bandwidth and wide scan angle. Yet, designs in [14] and [15] require at least 6 mm clearance and only simulation results have been presented. The feeding network and connectors have not been implemented in these designs.

In this paper a quad-mode planar antenna with -10 dB bandwidth of 8.2 GHz and -6 dB bandwidth of 10.8 GHz with the clearance of 1.2 mm is proposed for the 5G mobile terminals. The wide bandwidth and wide scan angle is obtained by combining four modes. The wide embedded radiation patterns are achieved for the all four modes. Because of the wide embedded radiation patterns of array elements, the wide scan angle is achieved by the proposed array. In this paper, the coaxial to differential stripline transition is used to differentially feed the proposed array elements without a balun structure. In the final design the endfire radiation pattern has been obtained along the full operating frequency range of the array. In this paper, the endfire and broadside directions are defined as the directions along and perpendicular to the phone chassis, respectively. The final design is simulated in CST Microwave Studio and measured in the anechoic chamber.

In section II the properties of the proposed antenna are discussed using a simplified feed. Then, in section III the antenna element's operation in a linear array is examined. Later in section IV the more complex feeding with the connector is introduced. Finally, in section V the performance of the proposed mobile 5G phased antenna array with connectors

---

This work was supported by the InnovationsFonden project of RANGE.(Corresponding author: Shuai Zhang).

Igor Syrytsin, Shuai Zhang, and Gert Frølund Pedersen are with the Antennas, Propagation and Millimeter-wave Systems section at the Department of Electronic Systems, Aalborg University, Denmark (email: {igs,sz,gfp}@es.aau.dk).

Art Morris is with wiSpry, Irvine, CA 92618 USA

will be verified through measurements and simulations.

II. ANTENNA GEOMETRY AND PRINCIPLE OF OPERATION

In this section, the antenna geometry and operation principle will be explained. The 3D figure of the antenna geometry is shown in Fig. 1(a). The substrate has been made transparent in order to expose the internal antenna structure. The antenna element consists of two dipole arms on each side of the PCB. The dipole arms are joined to the ground plane on each side of PCB and also the top dipole arm is connected to the bottom one by two vias, as shown in Fig. 1(b) and Fig. 1(c). Other vias are utilized in order to suppress the unwanted surface wave. The notch, located between the two dipole arms, is used for impedance matching of the antenna. The Rogers RO3003 substrate with the height of 1.524 mm, relative permittivity of 3 and loss tangent of 0.001 has been used in the design. In a proposed setup, the antenna is fed between two vias by a discrete port on the top layer, as shown in Fig. 1.

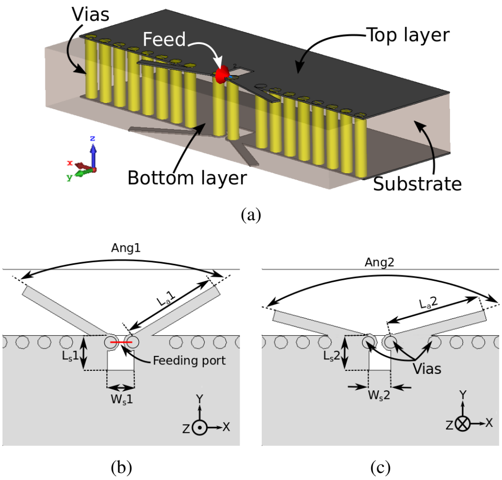

(a)

(b) (c)

Fig. 1. (a) 3D view of the proposed antenna element, geometry of the proposed antenna in (b) top PCB view and (c) bottom PCB view.

When the antenna is excited, four distinctive modes are achieved. The sketch of the electric field produced by the each mode can be observed in Fig. 2. It can be noticed that modes 1 and 2 are generated by the dipole on the top PCB layer and modes 3 and 4 are generated by the dipoles on the bottom layer. When the antenna is resonating in the mode 1 and 3 the electric field is present between each of the dipole arms and the ground plane. When the antenna is resonating in mode 2 and 4 the electric field of dipole-like nature can be observed between the dipole arms in Fig. 2.

The reflection coefficient of the antenna and resonant frequencies of the modes are shown in Fig. 3(a). The reflection coefficient is plotted for the antenna with dimensions of: $Ang1 = 110°$ and $Ang2 = 140°$, lengths $L_a1 = L_a2 = 2.2\,\text{mm}$, diameter of vias is 0.3 mm, the length of dipoles is 2.2 mm. Furthermore, the impedance of the antenna is plotted on smith chart in Fig. 3(b). The impedance circles for all four modes can be observed at the resonant frequencies.

The resonant frequencies of the modes 1 and 2 depend on the length L_a1 and the resonant frequencies of the modes 3 and 4 are determined by the length L_a2. Furthermore, the resonant frequency of the modes are also affected by the angles $Ang1$ and $Ang2$. The Fig. 4(a) and Fig. 4(b) show parametric sweeps of angles from 100° to 160°. It can be seen that when Ang1 is changed, the resonances of modes 1 and 2 are affected. The Fig.4(b) shows that when the Ang2 is varied then the resonant frequencies of modes 3 and 4 are affected. However, the matching of modes 1 and 2 is affected as well.

The resonant frequencies of all the modes depend also on the height and dielectric constant of the substrate. The diameter of the two vias at the end of the dipole arms is also an important factor. The dimensions of the notch on the top layer and the bottom layer can be adjusted in order to change the antenna matching properties.

In order to obtain the desired performance of the antenna, the lengths L_a1 and L_a2 should be chosen to obtain two lower and two higher resonances. The position of resonances can be adjusted by changing angles Ang2 and Ang1. Ang2 is adjusted first, since it mainly changes mode 3,4 and affect mode 1 2. Next, adjust angle 1 since it mainly varies mode 1 2. Finally, the matching of modes can be fine tuned by altering the dimensions of the notches.

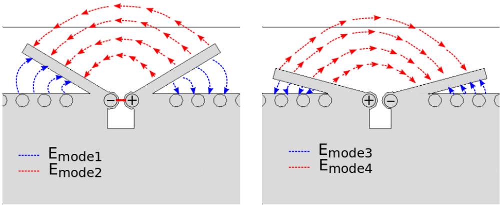

(a) (b)

Fig. 2. Electric fields of the proposed antenna's modes in (a) top view and (b) bottom view.

The surface currents of the proposed antenna on the top copper plane are shown in Fig. 5 in order to get a better insight on the operating mechanism of the proposed antenna. It can be observed that the surface currents are strong for the mode 1 and 2 and weak for the mode 3 and 4 on the top copper plane. The surface currents spread along the edge for the mode 1 and concentrate close to the dipole and notch for the mode 2. The surface currents on the bottom copper plane for all modes are shown in Fig. 6. In this case, the reverse behavior can be observed: mode 3 and 4 have stronger surface currents than mode 1 and 2. In the way similar to the mode 1 and 2, mode 3 has strong surface currents along the edge of the ground plane and mode 4 have currents concentrated around the notch and dipole arms. From the Fig. 5 and Fig. 6 it can be concluded that the antenna on the top copper plane contributes to the radiation of modes 1 and 2 and the antenna on the bottom copper plane contributes to the radiation of modes 3 and 4.

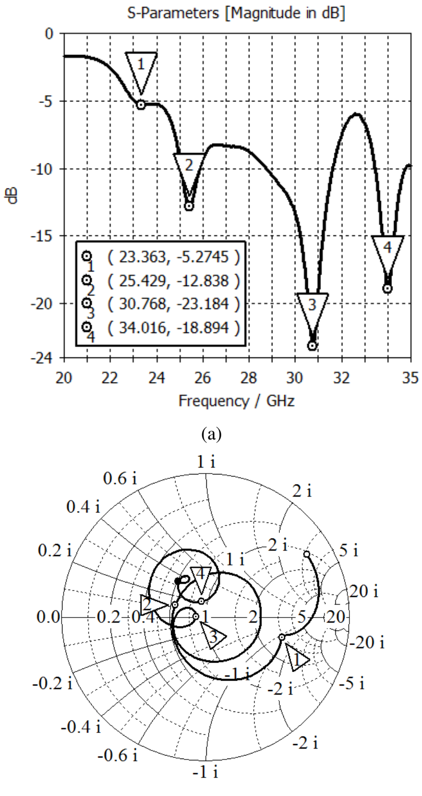

(a)

(b)

Fig. 3. (a) Reflection coefficient of the proposed antenna element, and (b) impedance of the proposed antenna plotted in Smith chart.

Furthermore, because the currents for the modes 1 and 3 are different from the surface currents of modes 2 and 4 it will be expected that those modes would have different radiation patterns when excited. The radiation patterns of a single antenna element are shown in Fig. 7 for all four modes. It can be clearly seen that radiation patterns of the modes 1 and 3 do not have a wanted end-fire radiation pattern. The two-lobe radiation pattern of modes 1 and 3 occurs because the E-field for those two modes concentrated between the dipole arms and the ground plane as shown in Fig. 2. However, the similar endfire radiation pattern is needed if the proposed antenna element should operate efficiently in an wideband array.

III. OPERATION IN AN ARRAY

In order to investigate the performance of the proposed element even further, a uniform linear array of 8 elements has been constructed on the short edge of the typical modern mobile phone ground plane, as shown in Fig. 8. In the application, the distance of 5.5 mm between elements has been chosen.

By introducing the neighboring elements, the open loop has been formed by the dipole arm of a neighboring element, the edge of the ground plane and one of the dipole arms of the

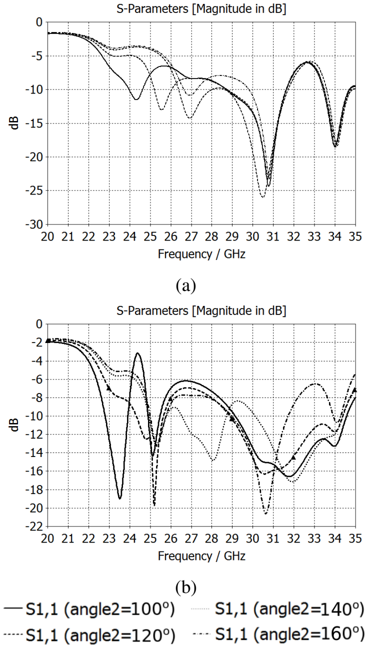

(a)

(b)

Fig. 4. Parametric sweep of (a) Ang1 and (b) Ang2.

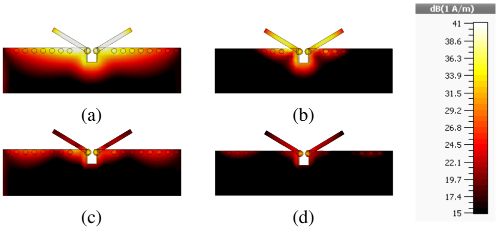

(a) (b)

(c) (d)

Fig. 5. Surface currents on the top copper plane of the proposed antenna operating in (a) mode 1, (b) mode 2, (c) mode 3, and (d) mode 4.

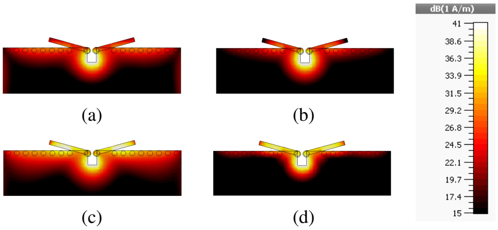

(a) (b)

(c) (d)

Fig. 6. Surface currents on the bottom copper plane of the proposed antenna operating in (a) mode 1, (b) mode 2, (c) mode 3, and (d) mode 4.

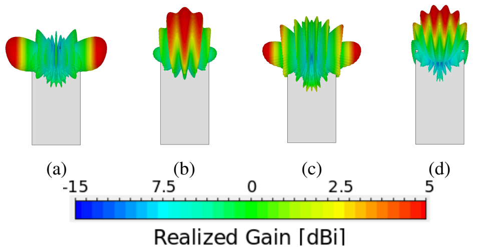

Fig. 7. Radiation pattern of the proposed antenna element in (a) mode 1, (b) mode 2, (c) mode 3, and (d) mode 4.

driven antenna. In Fig. 9 it is displayed how the surface currents will change when neighboring elements are introduced. This open loops help efficiently reduce the surface currents flowing on the ground for all four modes, and especially for modes 1 and 3. In this way, all the four modes will have similar current distributions and radiation patterns.

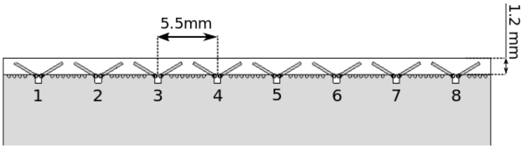

Fig. 8. The geometry of the proposed antenna array.

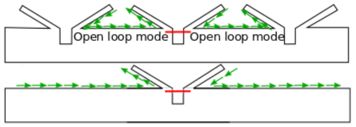

Fig. 9. Sketch of the open loop formed by neighboring elements.

The surface currents of the proposed array element, located between two other elements, are shown on the top and bottom copper planes in Fig. 10 and Fig. 11, respectively. It can be clearly observed that the current distributions for four modes are similar, where the currents mainly concentrate around the driven element and two formed open loops. It is also noticed that the surface currents on the ground plane edge in mode 3 (see Fig. 11(c)) are relatively stronger than the other modes. Nonetheless, the mutual coupling between array elements is low and the isolation is always over 10 dB within the operating band.

The embedded radiation patterns of the proposed array element are shown in Fig. 12. It can be observed that when the proposed element operates in the array the endfire radiation pattern can be achieved in all of the modes. However, as expected from the corresponding surface currents, the radiation pattern for the mode 3 in Fig. 12(c) is not exactly endfire. Two sidelobes can be observed in Fig. 12(c), but the gain at the sidelobes is not that high in comparison to the main lobe. In addition, the inter-element spacing affects the sidelobe levels of the modes 1 and 3. And there is a compromise between the sidelobes of the modes 1 and 3.

It can clearly be seen that radiation patterns are not orthogonal anymore, as in the case in Fig. 7. Due to the open loops formed by the neighboring elements and the ground plane in-between, the endfire radiation pattern are obtained for all the four modes.

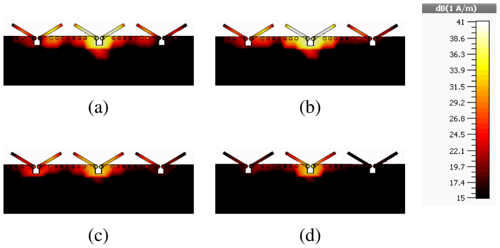

Fig. 10. Surface currents on the top copper plane of the proposed array element operating in (a) mode 1, (b) mode 2, (c) mode 3, and (d) mode 4.

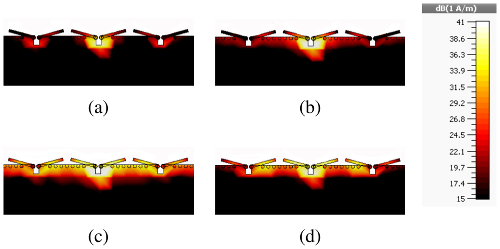

Fig. 11. Surface currents on the bottom copper plane of the proposed array element operating in (a) mode 1, (b) mode 2, (c) mode 3, and (d) mode 4.

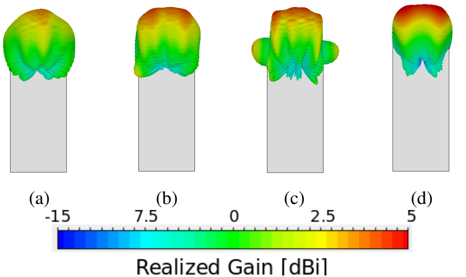

Fig. 12. Embedded radiation patterns of the proposed array element in (a) mode 1, (b) mode 2, (c) mode 3, and (d) mode 4.

Finally, the realized gain and sidelobe levels of the array are investigated for the different number of array elements. The isolation between elements is not shown because the metric of the realized gain already includes the coupling between array elements and return loss. The maximum realized gain of the array and sidelobe level are shown in Fig. 13 for array sizes from 2 to 8 elements. As expected, the realized gain increases and sidelobe level decreases with the number of elements. Yet, it can be seen that the difference between 7 and 8 element array is not significant. However, in the application the 8-element array has been chosen because the feeding network for the

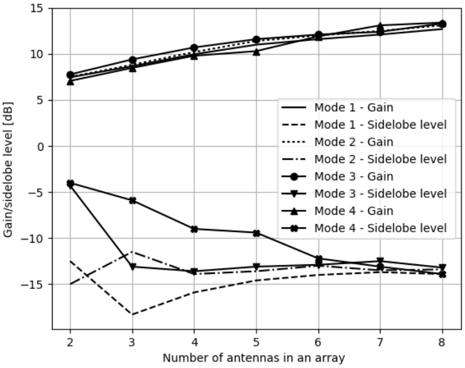

Fig. 13. Realized gain and sidelobe level of the proposed antenna array of different number of elements.

array of the odd number of elements is more challenging to make. Finally, one can notice that the difference of the curves for the maximum gain are within 1 dB for all of the modes.

IV. COAXIAL TO DIFFERENTIAL STRIPLINE TRANSITION

The proposed antenna has to be differentially driven as shown in Fig. 1. Usually, a Wilkinson power divider and a wideband 180° phase shifter are used to make a differential feeding. An example of this antenna feeding technique is shown in [16]. Another way to achieve the differential feeding is to use the 180° ring hybrid coupler. However, hybrid coupler structures are large in size and would significantly decrease the area available for the electronic components on the mobile phone ground plane. In this paper, it has been proposed to make a less complex coaxial to differential stripline transition in order to achieve the differential feeding of the antenna.

The overview of the antenna structure in 3D (where the substrate has been made transparent) and the internal feeding structure of the proposed antenna are shown in Fig 14. The differential stripline is connected to the two middle vias on the antenna structure. One of those vias is connected to the coaxial inner connector and the other is connected to the coaxial ground. The MMPX PCB CMD jack [17] (model number: $82_{M}MPX-S50-0-2$) has been mounted on the top ground plane. The PCB jack has been placed as close as possible to the antenna, in order to reduce the length and loss of the differential stripline.

The coaxial part of the connector extends all the way to the top ground plane. At the other end, the differential stripline has been connected to the top and bottom dipole antennas through the vias. Furthermore, now the antenna structure is more complex and requires at least one more additional layer for the differential stripline. Finally, the surface wave suppression vias have been added around the feeding structure. The exploded view of the connector and feeding structure is shown in Fig. 14(c).

The micro-via connected to the inner connector (center conductor) of the coaxial cable and one of the striplines. The through via connects the both ground planes, an outer-connector of the coaxial cable and the other stripline together. By using the proposed structure a balun is not required in order to achieve differential feeding of the antenna.

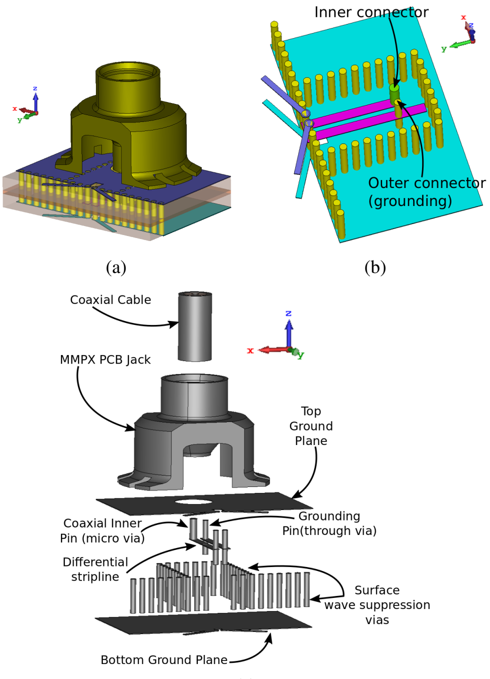

(a) (b)

(c)

Fig. 14. (a) 3D view of the antenna with the MMPX connector and feeding structure and (b) view of the internal feeding structure, and (c) Exploded view of the connector and feeding structure.

V. PHASED ARRAY WITH CONNECTORS

In this section a final phased array design, consisting of the 8 antennas with 8 MMPX connectors, is presented. The proposed phased antenna array performance is verified by the simulations in the CST Microwave Studio with more than 35.7 million FDTD mesh cells. The smallest cell size is 0.037 345 7 mm and largest cell size is 0.746 58 mm. Furthermore, the prototype of the array is constructed and measured in the anechoic chamber.

A. Geometry

The proposed phased antenna array has been made on the four copper layers. Two Taconic RF-30 ($\varepsilon_r = 3,\ \tan(\delta) = 0.0014$) 0.762 mm substrates have been glued with FR-4 ($\varepsilon_r = 4.3,\ \tan(\delta) = 0.025$) glue with 0.2 mm thickness. However, the FR4 glue does not affects the performance of the antenna significantly. The overview of the layers used in the antenna array PCB construction is shown in Fig. 15(a). The full PCB layout is shown in Fig. 15(b) and Fig. 15(c), consisting of four layers, vias and microvias. Because of the connector physical dimension limitations, it has been chosen to mount connectors both on the top and bottom layers. It can be seen that a mixture of micro-vias and vias has been used. The layer 2 is separated from the layer 3 by the 0.2 mm thick FR-4 glue.

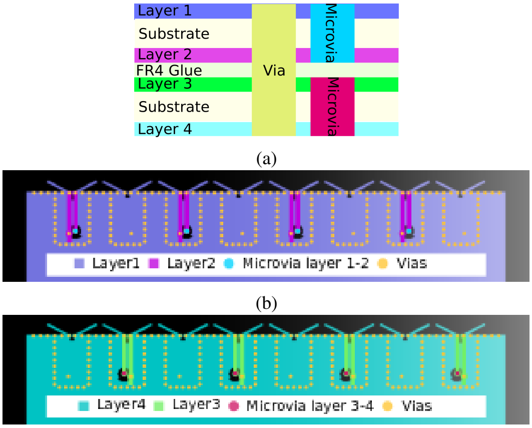

(a)

(b)

(c)

Fig. 15. Overview of the layers in the antenna structure (a) Overview of the PCB layers, (b) layer 1 and 2, and (c) layer 3 and 4.

The top and side views of the phased antenna array are shown in Fig. 16. Only the top the PCB has been shown because the bottom of the PCB looks exactly the same as the top. The dimensions of the ground plane are 106 × 47.5 mm. The clearance is only 1.2 mm, as shown in Fig. 16. The side view of the PCB is shown in Fig. 16(b) where connectors mounted on the both sides of the PCB can be spotted. Furthermore, the Taconic RF-30 layers are displayed in the light blue. The dimensions of the array element has been altered in respect to the Fig. 1 because the feeding point has been moved, and also the ground plane thickness has been increased (FR4 glue has been added). The final antenna element has following dimensions:

- Dipole length $L_a1 = L_a2 = 2.4\,\text{mm}$
- Angle between the dipole arms $Ant1 = Ang2 = 63°$
- $L_s1 = 0.9\,\text{mm}$
- $L_s2 = 0.6\,\text{mm}$
- $W_s1 = 0.5\,\text{mm}$
- $W_s2 = 0.4\,\text{mm}$
- Width of the dipole arms = 0.2 mm
- Diameter of vias is 0.3 mm
- Distance between vias is 0.4 mm
- Microvia diameter is 0.4 mm
- Stripline width is 0.4 mm
- Distance between striplines is 0.21 mm
- Thickness of all copper planes is 0.034 mm

B. Measurement Procedure

Next, the phased antenna array prototype and measurement setup are shown in Fig. 17. The zoomed in view of the connectors and antennas can be seen in Fig. 17(a). However, the solder has not been included in the simulations. The coordinate system can be seen in Fig. 17(b). In measurement only one antenna has been measured at a time, and 20 dB attenuators have been connected to the two neighboring elements. The available measurement system can only measure up to 140° in the elevation plane. Thus, it has been chosen to orient antenna in such a way, so the maximum gain is measured in $\theta = 0°$ direction. Furthermore, the system has better resolution at the top and worse resolution at the sides ($\theta = 90°$ plane). The 5° resolution has been chosen both in the elevation and azimuth planes.

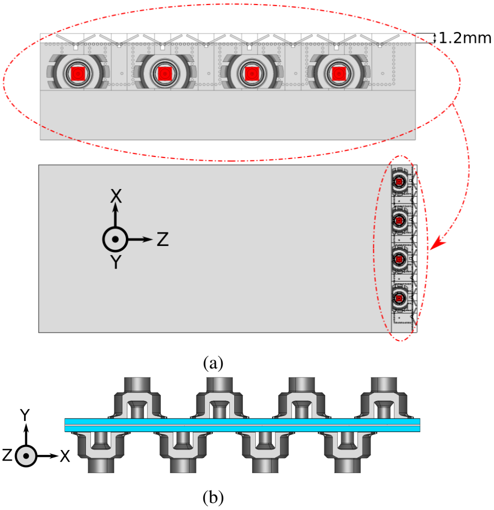

(a)

(b)

Fig. 16. Geometry of the phased antenna array with connectors (a) top view and (b) side view.

Typically, it is very challenging to measure the phase of the antenna radiation pattern accurately in the anechoic chamber. On the other hand, the magnitude of the radiation pattern can be obtained by comparing it to the known antenna (a standard gain horn has been used here). In order to measure the phase accurately the phase center of the measurement system should be found and located first. In this measurement, the phase center has been located by using a simple monopole antenna and a probe horn. The monopole antenna is rotated and the 2D radiation pattern is measured by the probe horn. The phase of the monopole antenna is constant when the antenna is located in the phase center of the measurement system.

After locating the system phase center, there are two ways of measuring the antenna array accurately. The first way is to put the antenna array center at the phase center of a measuring system and do not move the array location while all the elements are measured. The second way is to move each measured antenna element to the phase center of a measurement system each time when the measurement is performed.

If the phase center is fixed to each array element, then the gain of phased array can be computed as:

$$G_{array} = G_1 \cdot e^{j(k \cdot d \cdot sin(\theta)+\beta_1)} + G_2 \cdot e^{j(k \cdot d \cdot sin(\theta)+\beta_2)} + \ldots + G_8 \cdot e^{j(k \cdot d \cdot sin(\theta)+\beta_8)} \tag{1}$$

where:

- $G_1 \ldots G_8$ is a measured gain pattern of each antenna element.
- $k = \frac{2\pi}{\lambda}$ is a wave number.
- θ is the angle between the array scanning direction and the boresight direction.
- $\beta_1 \ldots \beta_8$ is a phase shift at each element's feed.

However, if the phase center is fixed with respect to the whole array, then the term $k \cdot d \cdot sin(\theta)$ is already included in the measurement. Thus the Eq.1 can be reduced to the following form:

$$G_{array} = G_1 \cdot e^{j \cdot \beta_1} + G_2 \cdot e^{j \cdot \beta_2} + \ldots + G_8 \cdot e^{j \cdot \beta_8} \tag{2}$$

Theoretically both methods are equally accurate for obtaining the correct radiation pattern phase. However, if the exact location of array element's phase center is not known, then the first method will be more accurate.

Finally, when processing the results it is important to mention that the pattern of each element should be calibrated at the boresight. In order to perform the beamforming correctly, the phase of each element at the boresight should have the same value. Furthermore, the phase calibration at the boresight should be done for co-polarized measurement, because the phase is more correct if the gain of antenna is high. In this paper the first measurement method has been applied.

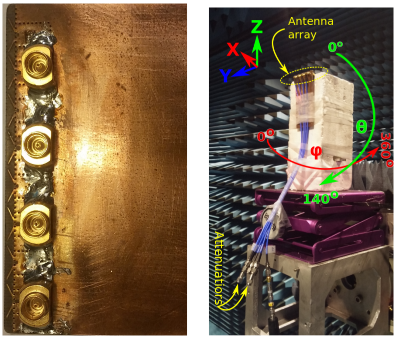

(a) (b)

Fig. 17. Prototype of the phased antenna array with connectors (a) zoomed in and (b) suspended in the anechoic chamber.

C. S-parameters

The simulated and measured reflection coefficients of the phased antenna array are shown in Fig. 18. It can be noticed that the four resonances, shown in Fig. 3(a), cannot be observed anymore because the geometry of the antenna has been changed. Furthermore, the parasitic resonance at the frequencies lower than 24 GHz can be observed both in simulations and measurements. Only 7 antennas have been measured because the antenna number 8 on the edge was not working because of the prototype production error. However, it can clearly be seen that simulations and measurements agree quite well. Only, the region around 30 GHz has around −6 dB matching, which is an acceptable value for a mobile antenna.

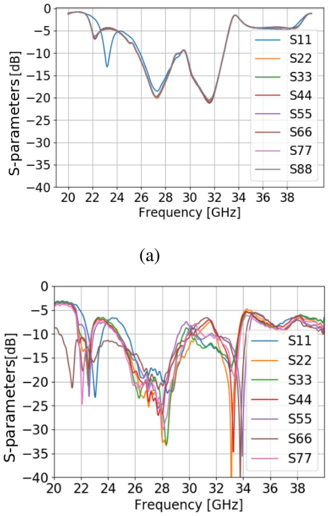

(a)

(b)

Fig. 18. Embedded reflection coefficients of (a) simulated array and (b) measured array.

D. Scan Angle

To investigate the scanning performance of the phased antenna array it has been chosen to look on the scan angle. In order to illustrate the scan angle, the main beam of the phased antenna array has been shown in the scanning range from -90° to 90° in Fig. 19. Notice that in order to form the array, the radiation pattern of the broken antenna element number 8 has been obtained by mirroring the radiation pattern of the element number 1. This can be done because of the antenna array symmetry around Z-axis. Furthermore, because connectors are mounted on the both sides of PCB, in post-processing the phase of every second antenna should be altered 180° in order to execute the beamforming correctly. Because in the final design the four modes could not be distinguished it has been chosen to illustrate the scanning results for the frequencies of 25, 27, 29, 31, and 33 GHz. Nonetheless, the measurements have been carried out in the frequency band from 25 to 33 GHz.

Wide scan angle behavior of the phased array can be observed in both simulations and measurements. However, the gain of the measured radiation patterns is higher when array is scanned to the large scan angles. Furthermore, the position of the beams for each scan angle in simulations and measurements are similar, which means that the prototype has correct dimensions and distance between elements. The beamforming pattern in Fig. 19(a) is more peaky than measurements in Fig. 19(b). It can also be observed that in Fig. 19(h) the maximum gain is 2 dB lower than that in simulations in Fig. 19(g). In Fig. 19(e) the simulated gain is approximately 2 dB lower than measured in Fig. 19(f).

The scan angle of the proposed phased antenna array is comparable to the other proposed mobile phased array designs. In [12] a switchable antenna array with the scan angle of around ±80° has been proposed. In [13] a slot antenna array with the scan angle of ±70° has been designed. Then, in [9] a low profile antenna has been proposed with the scan angle of ±80°. Finally, in [14] the wide scan antenna array with the scan angle of over ±85° has been proposed. However, all of those phased array designs have a narrow band characteristics or require big clearance to achieve wide scan angles.

E. Total Scan Pattern

In order to investigate the coverage of the phased antenna array, the total scan pattern (TSP) has been calculated. The total scan pattern is a combination of all possible phased antenna array's scan angles, where the best possible gain has been chosen at each spatial point. Progressive phase shifts of -180 to 180° have been applied to the antenna elements both in measurements and simulations. It has been chosen to show the TSP in the θ ranges from 0 to 140° both for measurements and simulations in order to reach the fair comparison.

The TSPs for the 25, 27, 29, 31 and 33 GHz frequencies are plotted in Fig. 20. First, it can be noticed that the maximum gain is higher for the measured array prototype. Also, the measured TSP of the prototype is not uniform because of the probable reflections in the anechoic chamber. Then again, the shapes of the total scan patterns for the simulations and measurements look similar.

F. Coverage Efficiency

Importantly, in order to have a full picture of the proposed phased antenna array performance the coverage efficiency has been calculated for the frequencies from 25 to 33 GHz. The coverage efficiency described the spatial coverage of the phased antenna array system and defined as [7]:

$$\eta_c = \frac{\text{Coverage Solid Angle}}{\text{Maximum Solid Angle}} \tag{3}$$

where maximum solid angle defined as 4π steradians.

The curves for the simulated and measured coverage efficiency are shown in Fig. 21. The lowest coverage can be observed at 30 GHz both in simulations and measurements. However, the measured coverage efficiency at 30 GHz, especially in the high gain region ($\geq$ 7 dBi), is lower than the simulated. The highest achievable simulated coverage occurs at 27 and 28 GHz. Having said that, the measured coverage at 25 GHz is also very high.

Finally, the mean and variance values of the coverage efficiency have been calculated from all frequency curves in Fig. 21. The simulated and measured mean coverage efficiency have very similar coverage values down to 2.5 dBi of threshold gain. The 50 % coverage with the gain of 5 dBi has been achieved. It means that if another proposed array is placed on the opposite edge of the ground plane and then the coverage efficiency of 100 % would be achieved with the gain of 5 dBi. The measured coverage efficiency has as much as 0.5 % more variance at the gain of 5 dBi in Fig. 22(b). These variance values can be explained by the unwanted reflections are present in the anechoic chamber under the measurement. The variance is lower towards the very low and very high gains.

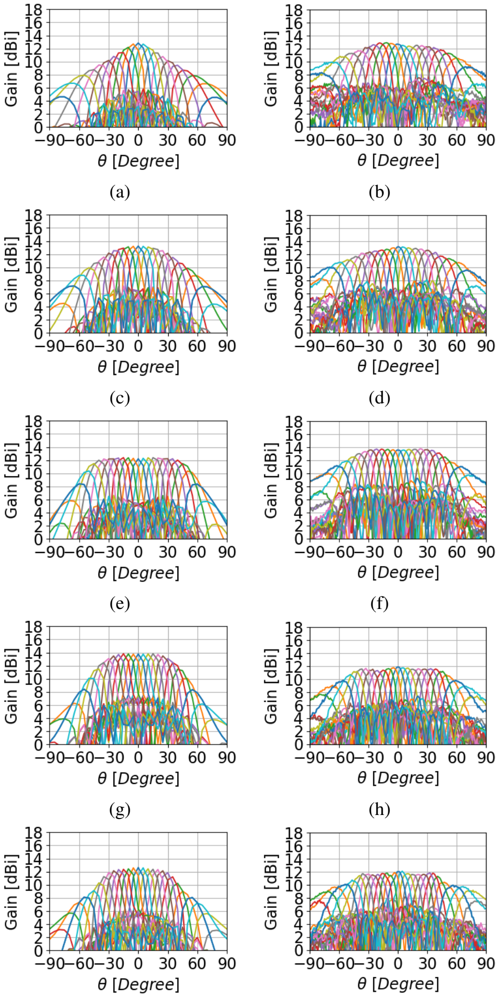

(a) (b) (c) (d) (e) (f) (g) (h) (i) (j)

Fig. 19. 2D scan of the proposed phased antenna array (a) simulations at 25 GHz, (b) measurements at 25 GHz, (c) simulations at 27 GHz, (d) measurements at 27 GHz, (e) simulations at 29 GHz, (f) measurements at 29 GHz, (g) simulations at 31 GHz, (h) measurements at 31 GHz, (i) simulations at 33 GHz, and (j) measurements at 33 GHz.

VI. CONCLUSION

In this paper, a quad-mode endfire planar phased 5G mobile antenna array with large scan angle and extremely small

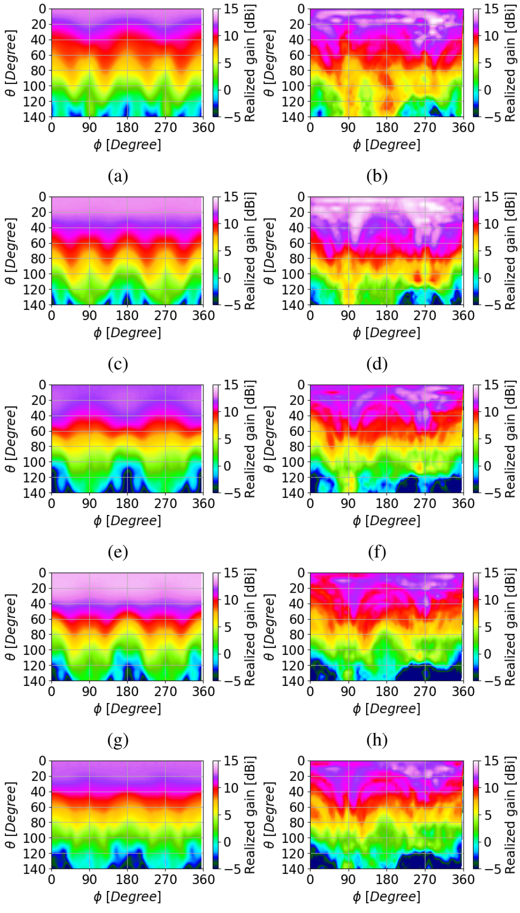

(a) (b) (c) (d) (e) (f) (g) (h) (i) (j)

Fig. 20. Total scan patterns of the proposed phased mobile antenna array (a) simulations at 25 GHz, (b) measurements at 25 GHz, (c) simulations at 27 GHz, (d) measurements at 27 GHz, (e) simulations at 29 GHz, (f) measurements at 29 GHz, (g) simulations at 31 GHz, (h) measurements at 31 GHz, (i) simulations at 33 GHz, (j) measurements at 33 GHz.

clearance has been proposed. The array element designed in this paper has different radiation patterns for each mode, but when combined into a linear array the embedded radiation patterns of an element are similar. The optimal distance between elements should be chosen in order to obtain the clean endfire embedded radiation patterns for the array elements in all modes. Furthermore, it has been shown how the surface currents and radiation patterns of an element change when combined into an array.

In order to make the proposed element design more practical for the mobile terminal applications, it has been chosen to used MMPX connectors and a feeding structure. Here it has been proposed to use coaxial to differential stripline feeding transition. Then a four-layer PCB has first been simulated in CST Microwave Studio and then measured in the anechoic

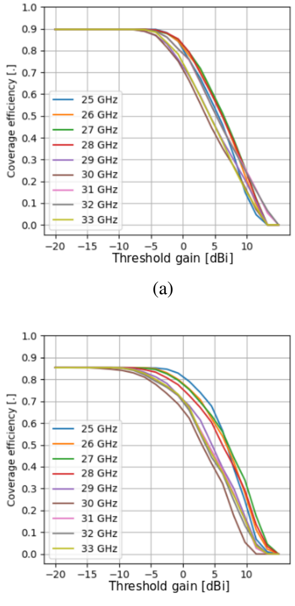

(a)

(b)

Fig. 21. Coverage efficiency of the phased antenna array: (a) simulations and (b) measurements.

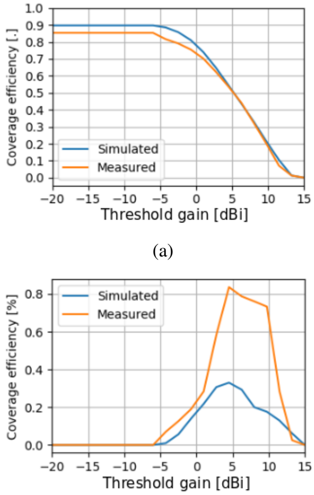

(a)

(b)

Fig. 22. Statistical investigation of measured and simulated coverage efficiency: (a) mean and (b) variance.

chamber. The final phased antenna array design has a scan angle of over 140° and impedance bandwidth of 8 GHz.

Finally, the total scan pattern and coverage efficiency of the measured and simulated phased array antenna have been calculated in the range from 25 to 33 GHz. The total scan patterns have the similar shapes for simulations and measurements. The mean coverage efficiency along the frequency range is very similar in measurements and simulations, but the measured antenna array has slightly more variance in the coverage efficiency between the frequency points. The coverage efficiency of around 50 % with the gain of 5 dBi has been achieved on average in the chosen frequency range.

REFERENCES

[1] T. S. Rappaport, S. Sun, R. Mayzus, H. Zhao, Y. Azar, K. Wang, G. N. Wong, J. K. Schulz, M. Samimi, and F. Gutierrez, “Millimeter Wave Mobile Communications for 5G Cellular: It Will Work!,” *IEEE Access*, vol. 1, pp. 335–349, 2013.

[2] W. Roh, J. Y. Seol, J. Park, B. Lee, J. Lee, Y. Kim, J. Cho, K. Cheun, and F. Aryanfar, “Millimeter-wave beamforming as an enabling technology for 5G cellular communications: theoretical feasibility and prototype results,” *IEEE Commun. Mag.*, vol. 52, pp. 106–113, Feb. 2014.

[3] S. J. Nawaz, N. M. Khan, M. N. Patwary, and M. Moniri, “Effect of Directional Antenna on the Doppler Spectrum in 3-D Mobile Radio Propagation Environment,” *IEEE Trans. Veh. Technol.*, vol. 60, no. 7, pp. 2895–2903, 2011.

[4] T. Manabe, Y. Miura, and T. Ihara, “Effects of antenna directivity and polarization on indoor multipath propagation characteristics at 60 GHz,” *IEEE Journal on Selected Areas in Communications*, vol. 14, pp. 441–448, Apr. 1996.

[5] Y. Azar, G. N. Wong, K. Wang, R. Mayzus, J. K. Schulz, H. Zhao, F. Gutierrez, D. Hwang, and T. S. Rappaport, “28 GHz propagation measurements for outdoor cellular communications using steerable beam antennas in New York city,” *2013 IEEE International Conference on Communications (ICC)*, pp. 5143–5147, 2013.

[6] M. U. Rehman, X. Chen, C. G. Parini, and Z. Ying, “Evaluation of a statistical model for the characterization of multipath affecting mobile terminal GPS antennas in sub-urban areas,” *IEEE Trans. Antennas Propag.*, vol. 60, pp. 1084–1094, Feb. 2012.

[7] J. Helander, K. Zhao, Z. Ying, and D. Sjöberg, “Performance analysis of millimeter-wave phased array antennas in cellular handsets,” *IEEE Antenna Wireless Propag. Lett.*, vol. 15, pp. 504–507, 2016.

[8] W. Hong, S. T. Ko, Y. Lee, and K. H. Baek, “Multi-polarized antenna array configuration for mmWave 5G mobile terminals,” *2015 International Workshop on Antenna Technology (iWAT)*, pp. 60–61, Mar. 2015.

[9] W. Hong, K. Baek, Y. Lee, and Y. G. Kim, “Design and analysis of a low-profile 28 GHz beam steering antenna solution for Future 5G cellular applications,” *Microwave Symposium (IMS), 2014 IEEE MTT-S International*, pp. 1–4, Jun. 2014.

[10] N. Ojaroudiparchin, M. Shen, and G. F. Pedersen, “Design of Vivaldi antenna array with end-fire beam steering function for 5G mobile terminals,” *2015 23rd Telecommunications Forum Telfor (TELFOR)*, pp. 587–590, 2015.

[11] R. Hussain, A. T. Alreshaid, S. K. Podilchak, and M. S. Sharawi, “Compact 4G MIMO antenna integrated with a 5G array for current and future mobile handsets,” *IET Microwaves, Antennas & Propagation*, vol. 11, no. 2, pp. 271–279, 2017.

[12] N. Ojaroudiparchin, M. Shen, S. Zhang, and G. F. Pedersen, “A Switchable 3-D-Coverage-Phased Array Antenna Package for 5G Mobile Terminals,” *IEEE Antennas Wireless Propag. Lett.*, vol. 15, pp. 1747–1750, 2016.

[13] S. Zhang, X. Chen, I. Syrytsin, and G. F. Pedersen, “A Planar Switchable 3D-Coverage Phased Array Antenna and Its User Effects for 28 GHz Mobile Terminal Applications,” *IEEE Trans. Antennas Propag.*, vol. 65, pp. 6413–6421, Dec. 2017.

[14] N. Ojaroudiparchin, M. Shen, and G. F. Pedersen, “Wide-scan phased array antenna fed by coax-to-microstriplines for 5G cell phones,” *2016 21st International Conference on Microwave, Radar and Wireless Communications (MIKON)*, pp. 1–4, 2016.

[15] N. O. Parchin, M. Shen, and G. F. Pedersen, “End-fire phased array 5G antenna design using leaf-shaped bow-tie elements for 28/38 GHz MIMO applications,” *2016 IEEE International Conference on Ubiquitous Wireless Broadband (ICUWB)*, pp. 1–4, 2016.

[16] M. Z. Azad and M. Ali, “Novel wideband directional dipole antenna on a mushroom like ebg structure,” *IEEE Trans. Antennas Propag.*, vol. 56, pp. 1242–1250, May 2008.

[17] Huber+Suhner, “MMPX 67 GHz /80 Gbps Snap-on Connectors.” http://pdf.directindustry.com/pdf/huber-suhner/mmpx-connectors/30583-293349.html.

Igor Syrytsin was born in Saratov, Russia, in 1988. He received the B.S. degree in electronic engineering and IT and M.S. degree in wireless communication systems from Aalborg University, Aalborg, Denmark, in 2014 and 2016, respectively. Currently, he is pursuing the Ph.D. degree at Department of Electronic Systems at Aalborg University. His research interests include mm-wave mobile antenna design and interactions between user and mobile antennas.

Shaui Zhang received the B.E. degree from the University of Electronic Science and Technology of China, Chengdu, China, in 2007 and the Ph.D. degree in electromagnetic engineering from the Royal Institute of Technology (KTH), Stockholm, Sweden, in 2013. After his Ph.D. studies, he was a Research Fellow at KTH. In April 2014, he joined Aalborg University, Denmark, where he currently works as Associate Professor. In 2010 and 2011, he was a Visiting Researcher at Lund University, Sweden and at Sony Mobile Communications AB, Sweden, respectively. He was also an external antenna specialist at Bang & Olufsen, Denmark from 2016-2017. He has coauthored over 40 articles in well-reputed international journals and over 14 (US or WO) patents. His research interests include: mobile terminal mm-wave antennas, biological effects, CubeSat antennas, UWB wind turbine blade deflection sensing, MIMO antenna systems, and RFID antennas.

Gert Frølund Pedersen was born in 1965. He received the B.Sc. and E.E. (Hons.) degrees in electrical engineering from the College of Technology in Dublin, Dublin Institute of Technology, Dublin, Ireland, in 1991, and the M.Sc.E.E. and Ph.D. degrees from Aalborg University, Aalborg, Denmark, in 1993 and 2003, respectively. Since 1993, he has been with Aalborg University where he is a Full Professor heading the Antenna, Propagation and Networking LAB with 36 researchers. He is also the Head of the Doctoral School on wireless communication with some 100 Ph.D. students enrolled. His research interests include radio communication for mobile terminals especially small antennas, diversity systems, propagation, and biological effects. He has published more than 175 peer reviewed papers and holds 28 patents. He has also worked as a Consultant for developments of more than 100 antennas for mobile terminals including the first internal antenna for mobile phones in 1994 with lowest SAR, first internal triple-band antenna in 1998 with low SAR and high TRP and TIS, and lately various multiantenna systems rated as the most efficient on the market. He has worked most of the time with joint university and industry projects and have received more than 12 M$ in direct research funding. He is currently the Project Leader of the SAFE project with a total budget of 8 M$ investigating tunable front end including tunable antennas for the future multiband mobile phones. He has been one of the pioneers in establishing over-the-air measurement systems. The measurement technique is now well established for mobile terminals with single antennas and he was chairing the various COST groups (swg2.2 of COST 259, 273, 2100, and now ICT1004) with liaison to 3GPP for over-the-air test of MIMO terminals. He is currently involved in MIMO OTA measurement.

Arthur S. Morris III (S'90–M'91–SM'04–F'13) received the B.S. degree in physics and also in electrical engineering and M.S. and Ph.D. degrees in electrical engineering from North Carolina State University (NCSU), Raleigh, NC, USA, in 1983, 1986, and 1993, respectively. As a Scientist/Engineer with a concentration on physical electronics and electromagnetic fields for over 30 years, he has contributed to device technologies ranging from traveling-wave tubes to millimeter-wave heterojunction bipolar transistors and has developed products for markets from high-voltage instrumentation to broadband communication systems. In 1999, he joined Coventor, to lead software and hardware development to drive the transition of microelectromechanical systems (MEMS) and microsystems from the laboratory into products for RF and optical applications. He is a cofounder of Wispry Inc., Irvine, CA, USA, which spun out of Coventor in 2002. He is the company's Chief Technical Officer (CTO) and leads the development of high-performance programmable RF products for high-volume markets utilizing MEMS, CMOS, and advanced packaging. He is an Adjunct Professor with NCSU.

Paper E

User Shadowing Suppression for 5G mm-wave Mobile Terminal Antennas

Igor Syrytsin, Shuai Zhang, Gert Frølund Pedersen, and and Art Morris

The paper has been published in:
IEEE Transactions on Antennas and Propagation, Vol. 67, Issue 6, pp. 4162-4172, 2019.

Abstract

In 5G mm-wave mobile terminal applications, the user's body has a very high chance of creating blockage or shadow in the radiation patterns of handset antenna arrays. In this paper, we find that the corner positions of a handset chassis yield the best performance for the 5G mm-wave array system in terms of spatial coverage when user effects are considered. To prove that claim, a prototype of a 5G mm-wave antenna system was constructed using the SIW lens and MMPX connectors and was compared to the more general case. The lens is simulated and measured with the user in talk, data and dual-hand modes. It has been shown that the method proposed in this paper can be used as general guideline for the 5G phased array construction. Finally, two configurations of sub-arrays placed diagonally on the opposite corners of the mobile device were investigated to compare them to each other and to the setup with sub-arrays in all the corners.

DOI:

https://ieeexplore.ieee.org/document/8370121

User Shadowing Suppression for 5G mm-wave Mobile Terminal Antennas

Igor Syrytsin, Shuai Zhang, *Senior Member IEEE*, Gert Frølund Pedersen, *Senior Member IEEE*, and Art Morris, *Fellow, IEEE*

***Abstract*—In 5G mm-wave mobile terminal applications, the user's body has a very high chance of creating blockage or shadow in the radiation patterns of handset antenna arrays. In this paper, we find that the corner positions of a handset chassis yield the best performance for the 5G mm-wave array system in terms of spatial coverage when user effects are considered. To prove that claim, a prototype of a 5G mm-wave antenna system was constructed using the SIW lens and MMPX connectors and was compared to the more general case. The lens is simulated and measured with the user in talk, data and dual-hand modes. It has been shown that the method proposed in this paper can be used as general guideline for the 5G phased array construction. Finally, two configurations of sub-arrays placed diagonally on the opposite corners of the mobile device were investigated to compare them to each other and to the setup with sub-arrays in all the corners.**

***Index Terms*—Mobile terminal antenna, antenna array, 5G, cm-wave, diversity, user impact.**

I. INTRODUCTION

LATELY the topic of beamforming at a mobile terminal for the 5th generation communication systems has been heavily studied. In [1], it has been proposed to use mm-wave frequencies for the 5G to achieve higher data rates. Already in 2017, eleven candidate bands in the frequency range between 24.25 GHz and 86 GHz have been discussed at the World Radiocommunication Conference [2]. To compensate for the path loss at the higher frequencies, high gain phased antenna arrays can be applied [3]. Furthermore, not only the peak gain but also the spatial coverage of the antenna have been recognized as important parameters. Spatial coverage performance is extremely important because the orientation of the mobile device is usually unknown. To characterize the spatial coverage, a metric of coverage efficiency has been introduced in [4] and then applied in [5] to characterize the performance of 5G mm-wave mobile devices.

Multiple mobile phased antenna array solutions already exist in the academic literature. Multi-polarized antenna arrays for the 5G mm-wave were constructed in [6]. A low-profile beam-steerable antenna for 5G mobile terminals was designed and analyzed in [7], and an even smaller antenna array with a clearance of 1.2 mm was proposed in [8]. To increase the 3D coverage of the 5G mobile antenna system, two different methods were proposed in [9] and [10]: folding the antenna structure and surface wave excitation, respectively. By increasing the scan angle, the higher coverage efficiency performance was obtained in [11] and [12]. Circularly polarized antennas for the 5G mobile terminals were developed in [13]–[15], which can improve the BER by always matching the polarization of the antenna and the channel. Then, to steer the beams with low loss and to reduce the system complexity, two passive parasitic elements were applied to scatter the main beam in [16]. Finally, in [17], it has been shown how a 4G MIMO antenna can be integrated with a 5G mm-wave array on the typical ground plane.

However, the user will also have a significant impact on the coverage performance of a mobile phased antenna array. Good coverage with a peak gain of at least 7 dBi is expected from the mobile antenna arrays. However, when the array is subjected to the user effects, the spatial coverage will drop significantly due to the blockage induced by the user, but the body loss is considerably lower than the body loss of sub 5 GHz mobile antennas [18]. However, body blockage at the 28 GHz is not as severe at 60 GHz, which has been investigated in [19]. At the resonant frequency of 15 GHz, the loss due to user effects has been evaluated in [20]. Similar or even greater losses would be expected for the mobile antenna arrays designed at the resonant frequency of 28 GHz, as shown in [18]. Effects of the full metal case and user's hand were also studied in [21], where the gain of at least 6.9 dBi has been achieved even with user effects considered. In [22], the user impact on switch diversity and phased antenna arrays for mobile devices was researched, and it has been found that beamforming is not always advantageous when user effects are considered. However, in the switch diversity case, only a single element on the short edge was studied, but the best array positions on the whole ground plane had not yet been assessed. Finally, in [23], a dual sub-array antenna system for 5G mobile terminals with SAR reduction capabilities was proposed, but it must be noted that in cm-mm-wave bands, power density should be used to evaluate a phantom electromagnetic wave absorption instead of SAR as given in [24]. Switchable phased antenna arrays had already been proposed in [10], but the optimal positions for the antenna array have not yet been found when user effects are considered. In this paper, a method of finding the most suitable locations on the whole ground plane for the 5G mobile terminal phased array is proposed at the frequency of 28 GHz. Then, the antenna array is constructed, based on the proposed guidelines and both measured and simulated

This work was supported by the InnovationsFonden project of RANGE.(Corresponding author: Shuai Zhang).

Igor Syrytsin, Shuai Zhang, and Gert Frølund Pedersen are with the Antennas, Propagation and Millimeter-wave Systems section at the Department of Electronic Systems, Aalborg University, Denmark (email: {igs,sz,gfp}@es.aau.dk).

Art Morris is with wiSpry, Irvine, CA 92618 USA

with the user. In Section II, the optimal positions for a 5G antenna array of four elements in a handset are obtained with the presence of the user effects. Then, in Section III, several planar sub-arrays are placed in the chosen locations on the ground plane. Furthermore, a substrate integrated waveguide (SIW) beamforming lens is applied for each sub-array. Later, the free space measured results of the two sub-arrays with two lenses in one corner are compared to the simulations in the CST Microwave studio. In Section IV, the proposed array is simulated and measured with the user in the talk, data and dual-hand mode, and in Section V, the two common array configurations are investigated. Finally, the effectiveness of the proposed method is assessed in section VI.

II. OPTIMAL ARRAY POSITION INVESTIGATION

In this section, the optimal antenna array positions where the lowest user impact is observed are determined. Here, the array coverage performance losses due to user blockage are the main contributor. The body loss is very low at mm-wave frequencies [18], so it is not an important factor for the investigation. Three setups using the homogeneous phantom as shown in Fig. 1 are considered. The phantom is made of skin tissue with $\varepsilon_r = 19 + 19j$ at 28 GHz. The antenna is simulated in three setups: talk mode in Fig. 1(a), data mode in Fig. 1(b), and dual hand mode in Fig. 1(c). The chosen phantom was first proposed in [25], based on the typical average physical dimensions of a male human being. The left-handed phantom is used in talk and data mode simulations. However, if the right-handed phantom is used, then the radiation patterns will be mirrored along the horizontal axis because of the phantom and antenna array symmetry.

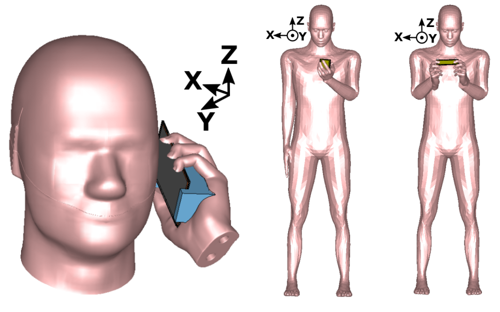

(a) (b) (c)

Fig. 1. Simulation setup with the user in (a) talk mode, (b) data mode, and (c) dual hand mode.

A. Simulation Setup

To investigate the user impact for the different array locations, we considered as many positions as physically possible on a typical ground plane with a size of 63 mm × 132 mm. Furthermore, the performance of the antennas with endfire and broadside radiation was compared at 28 GHz. For the purpose of the study, the antenna structure consisting of 120 antenna elements (64 Vivaldi and 56 slot antenna elements), as shown in Fig. 2, was constructed. The zoomed view of the antenna elements is also demonstrated in Fig. 2. The center-to-center distance between elements is $\lambda/2$ at 28 GHz.

To simplify the investigation, only 4 elements were combined into an array at a time. Each array is a phased array with the maximum scan angle of ±40 degrees. In this study, a sliding array principle was adopted, where each array can be composed of any four neighboring elements, but only linear arrays can be constructed. In Fig. 2, all of the positions of the sliding array are illustrated. A total of 40 Vivaldi (endfire) array positions and 32 of slot (broadside) positions were considered. All antennas were simulated one by one; then, the phased arrays were constructed in post-processing. The phase shifter and feeding network losses have not been accounted for in this work. However, in application these losses will be significant.

The total scan pattern (TSP) and coverage efficiency (CE) were calculated for each position of the sliding arrays. The TSP is extracted from all of the possible radiation patterns produced by the phased array with all the possible phase shifts. At each spatial point, the best possible gain value is chosen. The CE is then calculated from the TSP and describes the spatial coverage of the phased antenna array system. CE is defined as [5]:

$$\eta_c = \frac{\text{Coverage Solid Angle}}{\text{Maximum Solid Angle}} \quad (1)$$

where maximum solid angle is defined as 4π steradians.

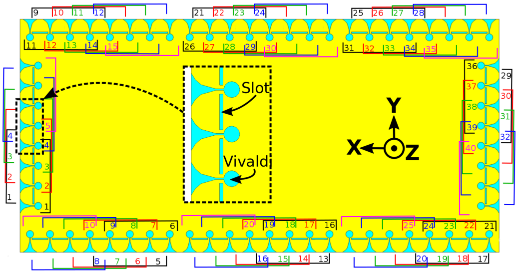

Fig. 2. Antenna structure used for the purpose of the optimal array investigation when user effects are considered. Vivaldi array positions are marked on the inside of the ground plane and the slot array positions are marked on the outside of the ground plane.

B. Best Possible Antenna Performance

In this subsection, the combined endfire array performance is compared to the combined broadside antenna performance. For this purpose, the TSP is calculated for all the possible sliding array positions. The TSP of all possible Vivaldi arrays is shown in Fig. 3. In free space in Fig. 3(a), the endfire arrays cover the region from $\theta = 20°$ to $\theta = 160°$ with high gain of 10 dBi. In contrast, regions where $\theta = 0$ to $20°$ and $\theta = 160$ to $180°$ are only covered with a gain of 3 dBi. Next, the TSP for the talk mode is displayed in Fig. 3(b). The shadow from the user's head is visible at $\phi = 300°$ and spans from 40 to 120° in θ, which is much smaller than the shadowing areas measured/simulated in [10], [18], [20], [22]. This already showed that using more sub-arrays distributed around the phone chassis has a beneficial effect on reducing the user blockage. In Fig. 3(c), the TSP for the data mode is illustrated. The shadowing area at $\phi = 270°$ is also much narrower than the shadowing areas discussed in [10], [18], [20], [22]. Finally, in Fig. 3(d) the shadowing area for dual-hand mode is at least 20° wider in ϕ direction than that observed in the data mode, as shown in in Fig. 3(c). These results are expected because both user's hands are on the mobile device at the same time; thus, more antenna elements are covered.

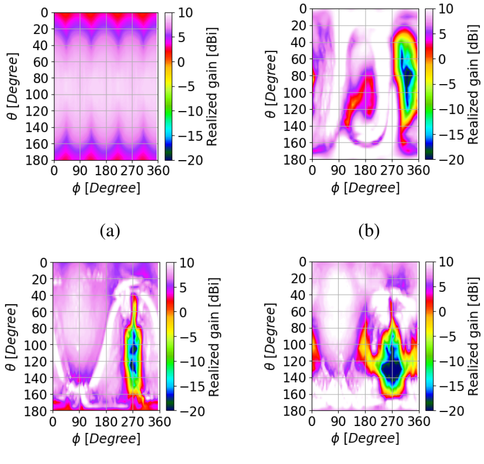

(a) (b)

(c) (d)

Fig. 3. TSP for all possible sliding Vivaldi arrays in (a) free space, (b) talk mode, (c) data mode, and (d) dual-hand mode.

The TSPs of all possible sliding slot arrays with broadside radiation patterns are shown in Fig. 4. In free space, the slot arrays cover the space opposite to the space of the Vivaldi arrays in Fig. 4(a). However, the gain of slot arrays is lower than the gain of Vivaldi arrays. The shadowing area in total scan patterns of slot arrays is very similar to one of Vivaldi arrays, but the maximum gain in all of the setups with a user is lower. As seen both in Fig. 3 and Fig. 4, the blind spots appear behind the user's body in data and dual-hand modes and behind the head in talk mode. In these blind spots, bad wireless connections at 28 GHz are expected. However, in the indoor scenario, the reflections from the walls, floor and ceiling and diffractions from the corners will contribute to the radiated power in the shadowing region. However, in the outdoor scenario, mostly line of sight components will be dominant, and the number of the scatterers close to the user will be very small.

Next, the CE performance is calculated from the TSPs in Fig. 3 and Fig. 4 and shown in Fig. 5. The CE of the Vivaldi arrays is shown in Fig. 5(a). The 100 % coverage for the threshold gain of 3 dBi can be achieved by these arrays. If the $\eta_c = 0.8$ is considered, the threshold gain in free space is then 7.5 dBi, in talk mode is 0 dBi, in data mode is 6 dBi, and in dual-hand mode is 2.5 dBi. However, in Fig. 5(b), the performance of slot arrays in free space is at least 2 dB worse for 100 % coverage. At the $\eta_c = 0.8$, the threshold gain of 5 dBi is expected in free space, 0 dBi in talk and dual-hand modes, and 2.5 dBi in data mode. In the region of coverage $\eta_c \leq 0.3$ the threshold gain for the setups with the user is truly higher because the user's body/head becomes an efficient scatterer. From this study, we can conclude that if all the possible sliding array positions are used, then the endfire arrays show better performance both in free space and in user cases.

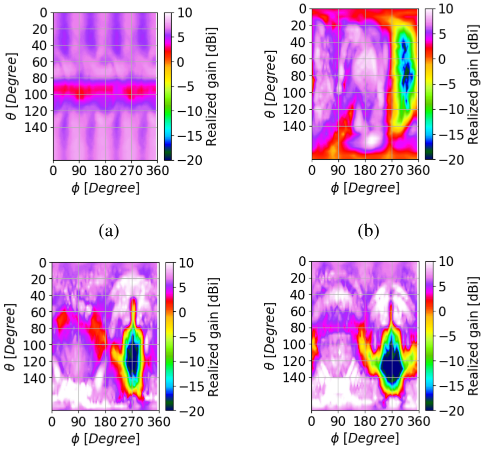

(a) (b)

(c) (d)

Fig. 4. TSP for all possible sliding slot arrays in (a) free space, (b) talk mode, (c) data mode, and (d) dual-hand mode.

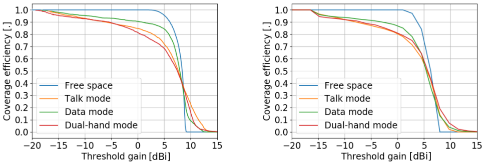

(a) (b)

Fig. 5. CE of all possible sliding (a) Vivaldi arrays and (b) slot arrays.

C. Best Position Evaluation

In this subsection, the performance of the sliding 4-element phased array is inspected in each of the positions on the ground plane. The CE is calculated for each sliding array position for both slot and Vivaldi arrays. Hence, four CE curves, like the CE curves displayed in Fig. 5, are obtained for each sliding array position.

To quantify the performance of the sliding array at the specific position, we decided to use metrics of mean threshold gain and coverage efficiency variance (CEV) at the mean threshold gain. These two metrics are calculated at the CE values of $\eta_c = 0.8$, $\eta_c = 0.5$ and $\eta_c = 0.2$. The mean of the threshold gain is calculated from the results in the free space, talk, data, and dual hand modes at the specific coverage efficiency value. The CEV is obtained between the results of talk, data, and dual hand modes at the specific mean gain value for each curve. The mean gain and variance values are shown for all of the sliding array positions at three specific CE values in Fig. 6.

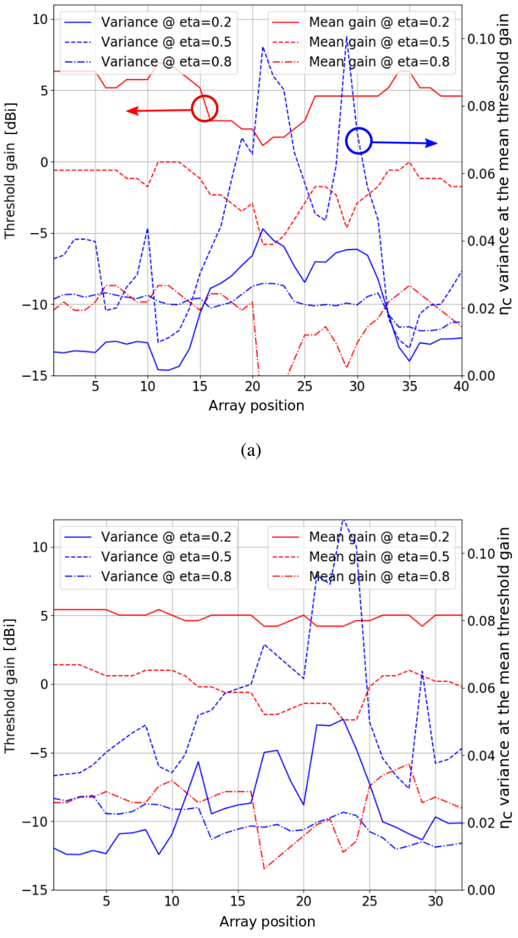

(a)

(b)

Fig. 6. Mean threshold gain and CEV between the free space, talk, data and dual-hand modes for (a) Vivaldi arrays, and (b) Slot arrays.

In this investigation, the positions where the mean gain is high and variance is low are considered to be optimal for good array performance because when the variance is low, the difference between the array performance in free space, talk, data, and dual hand modes is smaller. Thus, the antenna is not affected significantly by a user at these positions. In Fig. 6, an interesting trend can be observed. At the positions where the mean gain is high, the variance is low, which ias also true for all chosen values of coverage efficiency $\eta_c = 0.8$, $\eta_c = 0.5$ and $\eta_c = 0.2$. Generally, positions 1 to 15 and positions 35 to 40 are quite good for the endfire (Vivaldi) array placement in Fig. 6(a). Positions 1 to 12 and 25 to 32 are also good for the broadside (slot) array placement in Fig. 6(b).

Next, we investigated how much the mean gain and variance are correlated between the endfire and broadside arrays. The correlation coefficient was calculated between the endfire and broadside arrays in all the positions for all possible coverage efficiency values. The correlations in the mean and variance values are shown in Fig. 7. In all cases, the correlation coefficient is higher than 0.75. In conclusion, the performance of the antenna array does not depend so much on antenna type but mostly on the position of the array on the ground plane.

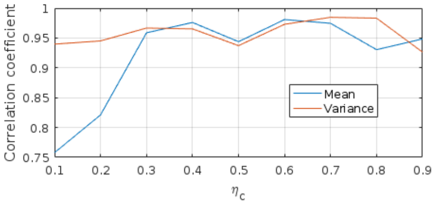

Fig. 7. Correlation coefficient between the broadside and endfire antenna elements.

To illustrate where the best positions of the arrays are located, only the mean gain of the endfire arrays is considered. The endfire array is chosen because it is the array with the most positions on the ground plane. Furthermore, it does not matter which array to choose because of the high correlation between endfire and slot arrays. At $\eta_c = 0.5$, the highest CEV value is observed. The high variance means large performance variation across the data, talk, and dual- hand modes, so the value of $\eta_c = 0.5$ could be considered the worst scenario. The hypothesis is that if the proposed method works for the $\eta_c = 0.5$, then it should work for the other coverage efficiency values as well. The normalized mean gain is shown at $\eta_c = 0.5$ for different positions around the ground plane. The gain alone can be the indicator of a good position because when the gain is high, the variance is low, as shown in Fig. 6. Each position of the 4-element array has been marked by the color of the corresponding normalized mean gain value and is shown in Fig. 8 on a typical mobile phone ground plane. The positions where the mean gain values equal 0 dBi are very suitable for the array placement and represent the best possible gain for the chosen array. At the positions where the color bar value is -3.5 dBi, the mean gain will be at least 3.5 dBi lower than the best possible mean gain with the same coverage. Fig. 8 clearly shows that the best positions are located around the corners of the mobile device. However, if the right-handed phantom is used for the talk and data simulations, then the picture in Fig. 8 will be mirrored along the horizontal axis because of the phantom and antenna array symmetry.

III. ARRAY IMPLEMENTATION WITH THE LENS

Based on the guidelines from Section II, the antenna array was constructed and tested with a real human in the anechoic chamber to verify the effectiveness of the method proposed in Section II. Usually, the phased array prototype is measured element by element and then, the results are combined in post-processing where the beamforming patterns are computed. To

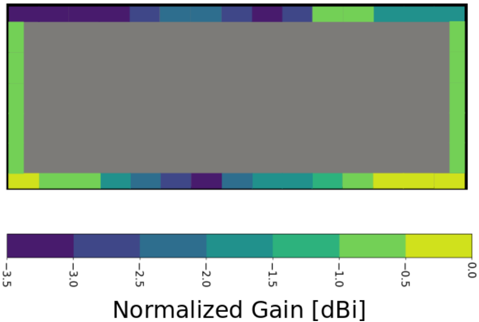

Fig. 8. Normalized mean gain at all of different 4-element sliding array positions around the mobile device ground plane.

obtain the correct beamforming patterns, both the phase and the magnitude of each element should be measured without errors. However, the phase stability is impossible to achieve because fixing a user in a perfect static position during the long measurement is not possible.

Any user will involuntarily make small movements that could be neglected when measuring at the LTE frequencies, but at 28 GHz, even small deviations of 2.5 mm of the antenna position will induce a 90-degree phase error. Applying a full body phantom could be a solution to eliminating the small movements during the measurements. However, at the current time, the full body phantoms at frequencies higher than 3.5 GHz are extremely expensive. Therefore, in this work, the array beamforming is achieved by a lens by switching between the input ports, so no phase shifters or extra post processing steps are required.

In addition, endfire radiation patterns are more preferred in practical applications, which are single directional instead of bi-directional such as broadside radiation patterns. The Vivaldi antenna in Section II has endfire radiation patterns, but the clearance is relatively large. To make the final design more suitable for applications, H-plane horn antennas will be used in the following, which have much smaller clearance and the endfire radiation patterns.

A. Lens Geometry

The four-port SIW lens utilized in this work has a structure similar to the structure described in [26]. However, the angles of SIW and the antenna element type were altered to reduce the total size. The geometry of the SIW lens is shown in Fig. 9. The structure is made on a single layer substrate of Rogers RO3550B with the height of 0.762 mm. Then, four MMPX connectors were used to feed the SIW in Fig. Fig. 9(a). The vias for the lens have a diameter of 1.5 mm, and vias used to feed the SIW have the diameter of 0.4 mm. The distance between vias is 2 mm.

A simple H-plane horn [27] that can be directly excited by SIW is chosen. However, contrary to [27], only two strips are used for the horn to reduce the ground plane clearance. In Fig. 9(b), the ground plane clearance of 2.2 mm has been obtained. The radiating element length is 5.5 mm, and the gap between elements is 0.2 mm.

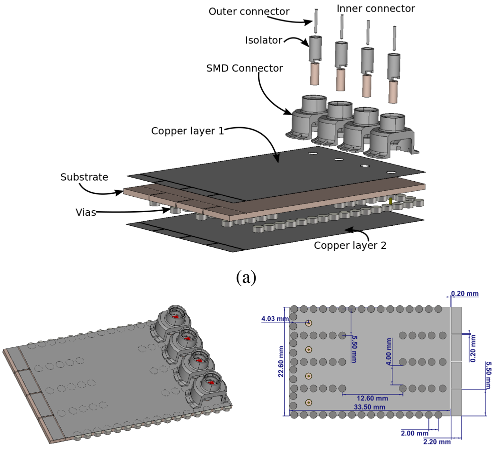

(a)

(b) (c)

Fig. 9. Antenna array with the lens (a) 3D view and (b) dimensions.

B. Operation Principle

To understand the operating principle of the lens, the maximum surface currents inside the lens are shown in Fig. 10. The purpose of the lens is to convert the TM10 mode of SIW to the TM40 mode inside the lens. Then, TM40 is used to feed the antenna elements at the end of the lens. The lens bends the wave inside the substrate in the clockwise direction when port 1 is excited in Fig. 10(a) and in the counterclockwise direction in Fig. 10(b). The surface current strength on the element 4 in Fig. 10(a) is approximately 4 dB weaker than the surface currents on the other three elements. A similar tendency can be observed for the elements 3 and 4 in Fig. 10(b). As a consequence, the beamwidth of a combined radiation pattern will be slightly larger than ideal. The isolation S32 and S14 are over 10 dB, and the isolation S12 and S34 are higher than 7.7 dB. Furthermore, because of the lens size, the loss in the dielectric is significant at 29.5 GHz. Thus, the efficiency of the proposed lens is -3 dB for ports 2 and 3 and -4 dB for the ports 1 and 4.

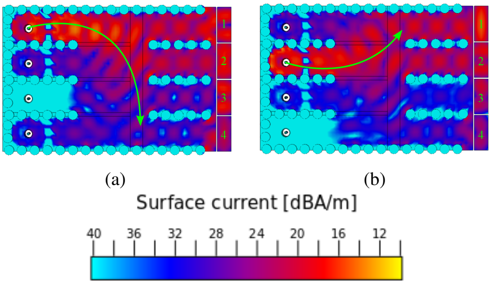

(a) (b)

Fig. 10. Surface currents inside the SIW lens observed when (a) port 1 is excited and (b) port 2 is excited.

To investigate how the proposed lens compares to the conventional array of 4 elements, the performance of the array with and without the lens is compared in Fig. 11. In the array without a lens, the antenna elements are excited directly by the waveguide ports. The phase shift steps used for the beamforming setup are (-100, -50, 50, 100 degrees), which means that the maximum phase shift needed for the four-element array is ±300°. The performance of the phased array is comparable to the implementation with the lens in Fig. 11, but the sidelobes are higher for the lens. Nonetheless, to implement this 4-element phased array, a maximum phase shift of ±300° is required. In the application, phase shifters with such requirements will make the array more lossy than the lens, which only requires a switch.

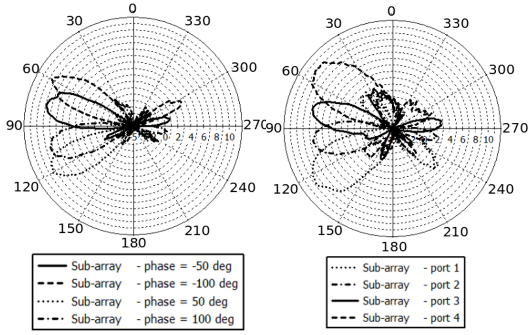

(a) (b)

Fig. 11. Performance comparison of (a) phased array implementation and (b) lens implementation.

C. lens Integration

In this subsection, the lens proposed in Subsection III-A is integrated on a big ground plane. The ground plane size corresponds to the size of a typical mobile device and is shown in Fig. 12(a). The two sub-arrays are placed on the corner of the ground plane. Three layers of copper with 2 layers of the substrate are used in the design in Fig. 12(a). Furthermore, to reduce the ground plane influence on the antenna elements, the small reflectors with the height of 3 mm are added on each side of the ground plane.

The reflection coefficients for both sub-arrays are shown in Fig. 13. Reflection coefficients of the measured lens are generally shifted towards lower frequencies. Furthermore, for ports 1 and 4, two resonances are obtained from the measurements, but only one is obtained in the simulations in Fig. 13(a) and Fig. 13(b). The two lenses are identical, but because connectors have not been mounted perfectly, the difference in matching between the lenses can be observed. Notice here that the lens is operating optimally at the frequency of 29.5 GHz. This frequency is different from the one used for investigation in Section II. However, the difference in the user impact at 28 and 29.5 GHz is insignificant.

Next, the proposed dual sub-array system is measured in the anechoic chamber as shown in Fig. 12(b). In this investigation, we propose to use the antenna system with two sub-arrays on each corner, according to the suggestions from Section II. However, to simplify the manufacturing process, we chose to make a prototype with only two sub-arrays. However, in the investigation, the ground plane is rotated around the X-axis and Y-axis to obtain radiation patterns in all the desired directions, as shown in Fig. 14.

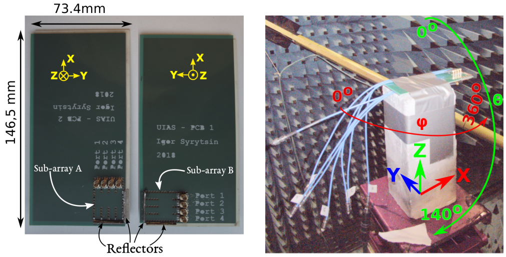

(a) (b)

Fig. 12. (a) two prototype PCBs with one sub-array on each and (b) prototype measured in the anechoic chamber.

The calculated TSP from the simulations and the measurements of the total combined system of 8 sub-arrays are shown in Fig. 15. The directions of the radiation for each sub-array are similar. In the simulations, the radiation patterns obtained by exciting ports 1 and 4 of each SIW lens have a higher maximum gain than the radiation patterns obtained by exciting ports 2 and 3. However, in the measurements, the radiation patterns of ports 2 and 3 have the highest maximum gain. Finally, the CE of the proposed system is calculated and shown in Fig. 18. The CE curve for the measurements is steeper.

IV. User Impact

First, in Section II, we proposed to put antenna arrays in the corners of the mobile phone ground plane. To account for the left-handed and right-handed users, we chose to place a lens in all the corners of the ground plane, as shown in Fig. 14. To verify the proposal of Section II, the prototype was simulated and measured in free space, talk, data, and dual-hand modes, as shown in Fig. 1. In measurements, the phantom is replaced by a user with dimensions like a phantom, as shown in Fig. 16. The same user was participating in the measurements and in the phantom accuracy verification in [25]. The rope has been used in all three setups to secure the user. The foam stand is added to the measurement setup to ensure that the height, angle, and distance to the body remain constant and similar to the simulations.

The radiation patterns at each lens port are measured, and the prototype is rotated to replicate the similar setup, as described in Fig. 14. A TSP is calculated for each of the setups and is shown in Fig. 17. In the talk mode depicted in Fig. 17(a), the shadow from the head appears bigger than the shadow from the head in the measurement in Fig. 17(b). In Fig. 17(c), the shadow looks similar to the measurement of the prototype in the data mode in Fig. 17(d). However, the power behind the user is stronger in the measurement of data mode. Similar conclusions can be drawn from the comparison between simulated and measured results for the dual-hand mode in Fig. 17(e) and Fig. 17(f). However, the shadowing from the head is smaller in the simulations. In all

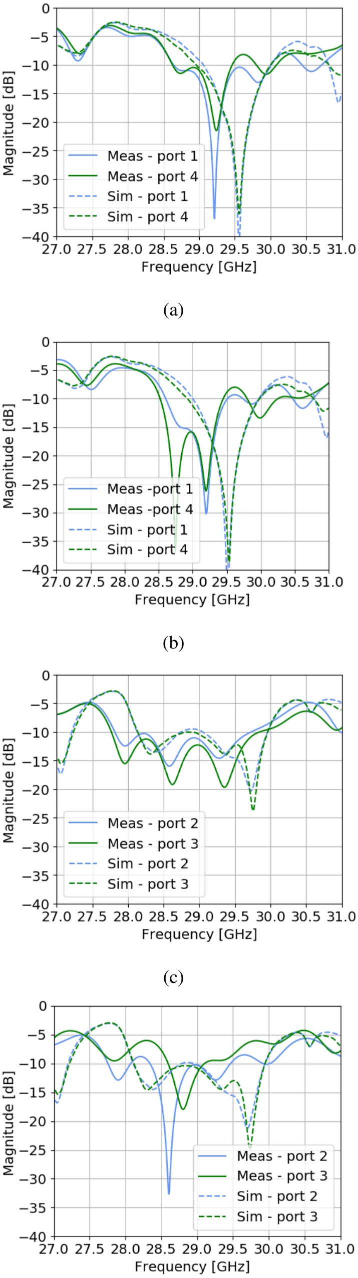

(a)

(b)

(c)

(d)

Fig. 13. Reflection coefficients of the (a) Sub-array A at ports 1 and 4, (b) Sub-array B at ports 1 and 4, (c) Sub-array A at ports 2 and 3, and (d) Sub-array B at ports 2 and 3.

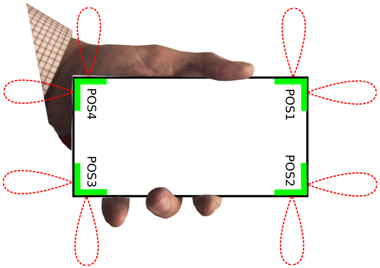

Fig. 14. Antenna array positions considered for the investigation and corresponding radiation pattern directions. The hand has been added to illustrate the grip example with the left hand.

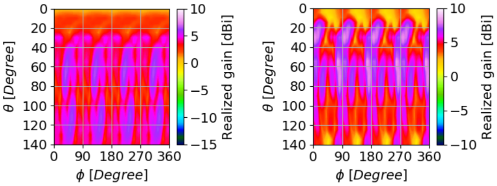

(a) (b)

Fig. 15. Total scan pattern of the (a) simulated and (b) measured SIW lens antenna system.

the measurements, the user appears to be able to redirect a considerable amount into the shadow.

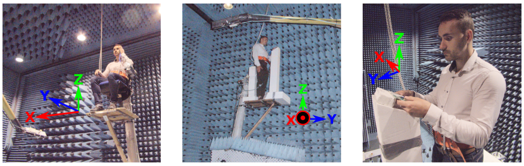

(a) (b) (c)

Fig. 16. Measurement setups with the user in (a) talk mode, (b) data mode, and (c) dual-hand mode.

Finally, the coverage performance results from the measurements and simulations are compared for the four setups in Fig. 18. First, the spread between the data mode, talk mode, and free space curves is larger in the measurements. For the CE of 0.5, the value of threshold gain of 2.5 dBi can be observed in simulations for data and dual-hand modes and 3 dBi for the talk mode in Fig. 18(a). However, in measurements, the gain value of 2.5 dBi at $\eta_c = 0.5$ is obtained in dual-hand mode. Then, the gain of 1.5 dBi and 0.5 dBi is achieved for the data and talk modes, respectively. The performance of the prototype in talk mode is quite different from simulations to measurements, which can be explained by the grip of the user. In talk mode, the user's grip is a very important parameter for the antenna performance, but it is very difficult to replicate the simulated CTIA grip with the actual user.

In [25], a loss of 8.5 dB from free space to talk and data mode curves at $\eta_c = 0.5$ is observed. In [20], a loss of 7.5 to 10 dB is observed for the talk mode, and a loss of approximately 3 dB is observed for the data mode. However, the results in [20] cannot be directly compared to the design proposed in this

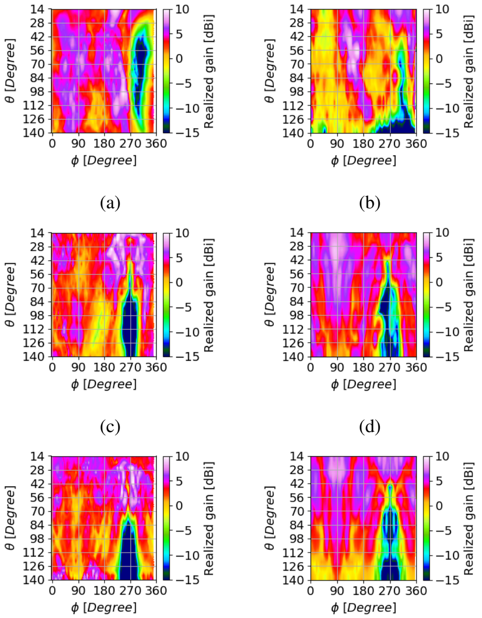

(a) (b)

(c) (d)

(e) (f)

Fig. 17. Total scan patterns of the user (a) simulated in talk mode, (b) measured in talk mode, (c) simulated in data mode, (d) measured in data mode, (e) simulated in dual-hand mode, and (f) measured in dual-hand mode.

paper, because the frequency in [20] is 12 GHz lower; thus, an actual user will affect the waves differently. In this work, a loss of 2.5 dB for the dual-hand mode, 3 dB for the data mode, and 4.5 dB for the talk mode is observed for $\eta_c = 0.5$. These values are lower than the loss observed in the previous works. Furthermore, the talk mode could be considered not as important because an actual user will usually use GSM in talk mode and the fast data rate 5G mm-wave in data and dual-hands modes.

V. Investigation of Other Array Configurations

Next, we chose to investigate how the popular [28] alternative array configurations will affect the coverage performance. We investigated how the performance of the sub-array arrangement in positions 1 and 3 (configuration A) compares to the performance of sub-array arrangement in positions 2 and 4 (configuration B), as shown in Fig. 14. Here, we show only the measured results because they represent the actual scenario.

The TSP for free space, talk, data, and dual-hand modes is depicted in Fig. 19. The free space TSPs for both configurations will be the same but shifted by 90° in ϕ direction, which we have chosen not to show here, as user effects are the main purpose of this investigation. However, in the talk mode, the position of the shadow is different because of the different antenna positions with respect to the user's head, as shown in Fig. 19(a) and Fig. 19(b). An interesting observation can be made for results in a data mode in Fig. 19(d), where

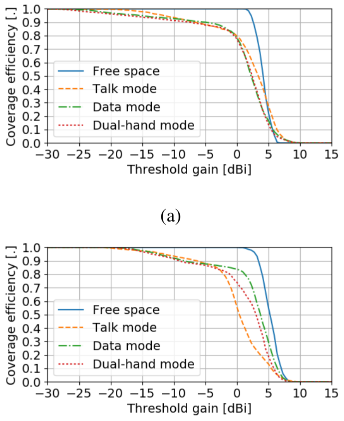

(a)

(b)

Fig. 18. Coverage efficiency of the (a) simulated and (b) measured antenna system.

the power inside the shadowing area is much stronger than the power inside the shadowing area in Fig. 19(c). We speculate that the antenna array proximity to the skin in configuration B will excite a surface wave on the user's hand and thus transfer more power behind the user. Finally, in the dual-hand mode in Fig. 19(e) and Fig. 19(f), the TSPs look very similar, as expected from the setup symmetry.

Next, the CE is calculated for both configurations and shown in Fig. 20. Instantly, we notice that configuration A is the best to use in the data mode. At a CE level of 0.5, the value of the threshold gain of -2 dBi is observed for configuration B and 2.5 dBi for configuration A, which yields an improvement of 4.5 dB. The CE curves for dual-hand mode are very similar, as expected from the setup symmetry. Finally, only a very small improvement in talk mode only could be seen for the high coverage region ≤ 0.7, where the configuration B is better. However, we can conclude that to account for both right- and left-handed users, the final setup used in the applications should include arrays in all four corners of the device, as shown in Fig. 14.

VI. Assessment of Method's Effectiveness

In this section, the effectiveness of the method that helps to find the best possible position for the array discussed in Section II will be verified. First, to make a fair comparison, the elements in Fig. 2 are arranged into the same configuration as shown in Fig. 14, as has been demonstrated to be advantageous in Section V. In Section II, it has already been established that the user effects on the antenna depend strongly on the antenna locations and not the antenna type. Thus, we chose to consider only endfire (Vivaldi) arrays from Section II.

To verify if the method proposed in Section II works, the mean and variance of the coverage efficiency have been computed for all possible sliding Vivaldi array positions corresponding to Fig. 5(a). If the method proposed in this paper is valid, then both CE mean and variance should be similar for

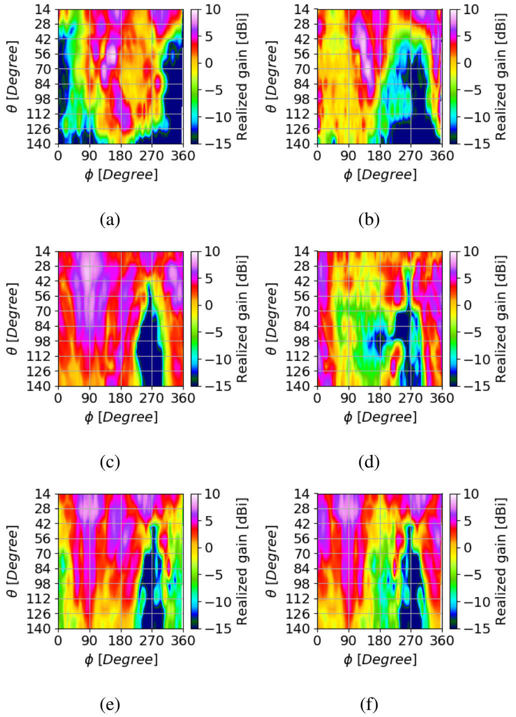

(a) (b) (c) (d) (e) (f)

Fig. 19. Measured total scan patterns of the user (a) conf. A – free space, (b) conf. – free space, (c) conf. A – talk mode, (d) conf. B – talk mode, (e) conf. A – data mode, (f) conf. B – data mode, (g) conf. A – dual-hand mode, and (h) conf. B – dual-hand mode.

the case with the sliding Vivaldi array (best possible scenario) and the corner Vivaldi array in the configuration, as presented in Fig. 14. As seen here, both CE mean and variance are indeed similar for these two cases as shown in Fig. 21.

Finally, the Vivaldi antenna arrays are compared to the SIW lens arrays in a similar way. Notice that the loss of the lens is on average approximately 4 dB, which does not occur in the Vivaldi arrays, so the curves for the Vivaldi arrays are moved 4 dB to the right to obtain the fair comparison, as shown in Fig. 21. All the mean coverage efficiency curves have a very similar shape, but the curves for the variance in Fig. 21(b) have a slight difference, especially at the part with the peak variance. Endfire arrays have 2 dB lower peak variance than the results of the simulated SIW lens system. Additionally, the measured SIW lens system has 5 dB higher maximum variance than the endfire arrays. However, the measured results show lower variance for the threshold gain below -10 dBi. From this assessment, we can conclude that the method proposed in Section II, as expected, can be used for determining the best location for any antenna type, as the user impact depends strongly on the antenna location instead of the antenna type.

VII. CONCLUSION

In this paper, the guidelines for the best possible positions of the 4-element phased 5G mobile array are presented. In

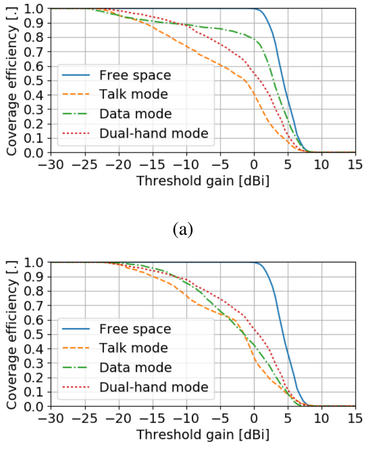

(a)

(b)

Fig. 20. Total scan pattern of the sub-arrays arranged in (a) configuration A and (b) configuration B.

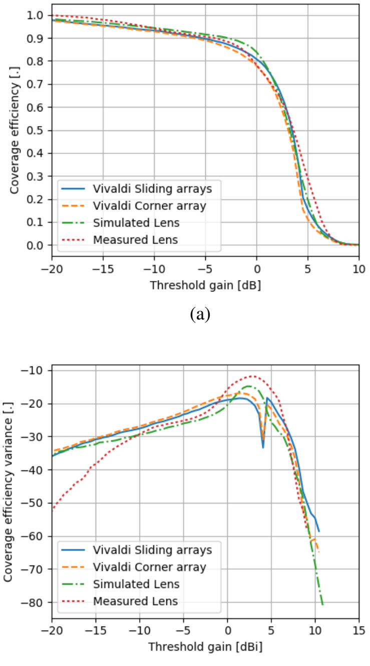

(a)

(b)

Fig. 21. Comparison of the sliding arrays, corner arrays, measured and simulated lenses by computing (a) mean coverage efficiency and (b) coverage efficiency variance.

this paper, simulations and measurements were performed in three different user-antenna setups: data mode, talk mode and dual-hand mode. The user shadowing effects can be efficiently suppressed with arrays in all four corners of the mobile phone chassis. Then, based on these guidelines, the antenna array was constructed and tested with the real humans in the anechoic chamber to verify the effectiveness of the guidelines. To obtain the correct beamforming patterns with the user and avoid phase errors, the SIW lens sub-array implementation was chosen. The proposed setup is compared to the one with the Vivaldi arrays in two different configurations. A very small difference in the mean and variance of coverage efficiency was found. Thus, the proposed guidelines in this paper are general and can be used for any 5G mm-wave antenna type.

REFERENCES

[1] T. S. Rappaport, S. Sun, R. Mayzus, H. Zhao, Y. Azar, K. Wang, G. N. Wong, J. K. Schulz, M. Samimi, and F. Gutierrez, "Millimeter wave mobile communications for 5G cellular: It will work!," *IEEE Access*, vol. 1, pp. 335–349, 2013.

[2] J. Lee, E. Tejedor, K. Ranta-aho, H. Wang, K. T. Lee, E. Semaan, E. Mohyeldin, J. Song, C. Bergljung, and S. Jung, "Spectrum for 5G: Global status, challenges, and enabling technologies," *IEEE Comm. Mag.*, vol. 56, pp. 12–18, Mar. 2018.

[3] W. Roh, J. Y. Seol, J. Park, B. Lee, J. Lee, Y. Kim, J. Cho, K. Cheun, and F. Aryanfar, "Millimeter-wave beamforming as an enabling technology for 5G cellular communications: theoretical feasibility and prototype results," *IEEE Commun. Mag.*, vol. 52, pp. 106–113, February 2014.

[4] M. U. Rehman, X. Chen, C. G. Parini, and Z. Ying, "Evaluation of a statistical model for the characterization of multipath affecting mobile terminal GPS antennas in sub-urban areas," *IEEE Trans. Antennas Propag.*, vol. 60, pp. 1084–1094, Feb. 2012.

[5] J. Helander, K. Zhao, Z. Ying, and D. Sjöberg, "Performance analysis of millimeter-wave phased array antennas in cellular handsets," *IEEE Antenna Wireless Propag. Lett.*, vol. 15, pp. 504–507, 2016.

[6] W. Hong, S. T. Ko, Y. Lee, and K. H. Baek, "Multi-polarized antenna array configuration for mmwave 5G mobile terminals," *2015 International Workshop on Antenna Technology (iWAT)*, pp. 60–61, Mar. 2015.

[7] W. Hong, K. Baek, Y. Lee, and Y. G. Kim, "Design and analysis of a low-profile 28 GHz beam steering antenna solution for future 5G cellular applications," *Microwave Symposium (IMS), 2014 IEEE MTT-S International*, pp. 1–4, Jun. 2014.

[8] I. Syrytsin, S. Zhang, G. F. Pedersen, and A. Morris, "Compact quad-mode planar phased array with wideband for 5G mobile terminals," *IEEE Trans. Antennas Propag.*, 2018,(in press).

[9] N. Ojaroudiparchin, M. Shen, S. Zhang, and G. F. Pedersen, "A switchable 3-D-coverage-phased array antenna package for 5G mobile terminals," *IEEE Antennas Wireless Propag. Lett.*, vol. 15, pp. 1747–1750, 2016.

[10] S. Zhang, X. Chen, I. Syrytsin, and G. F. Pedersen, "A planar switchable 3-D-coverage phased array antenna and its user effects for 28-GHz mobile terminal applications," *IEEE Trans. Antennas Propag.*, vol. 65, pp. 6413–6421, Dec 2017.

[11] N. Ojaroudiparchin, M. Shen, and G. F. Pedersen, "Wide-scan phased array antenna fed by coax-to-microstriplines for 5G cell phones," *2016 21st International Conference on Microwave, Radar and Wireless Communications (MIKON)*, pp. 1–4, 2016.

[12] N. O. Parchin, M. Shen, and G. F. Pedersen, "End-fire phased array 5G antenna design using leaf-shaped bow-tie elements for 28/38 GHz MIMO applications," *2016 IEEE International Conference on Ubiquitous Wireless Broadband (ICUWB)*, pp. 1–4, 2016.

[13] K. R. Mahmoud and A. M. Montaser, "Design of dual-band circularly polarised array antenna package for 5g mobile terminals with beam-steering capabilities," *IET Microwaves, Antennas Propagation*, vol. 12, no. 1, pp. 29–39, 2018.

[14] I. Syrytsin, S. Zhang, and G. F. Pedersen, "Circularly polarized planar helix phased antenna array for 5G mobile terminals," in *2017 International Conference on Electromagnetics in Advanced Applications (ICEAA)*, pp. 1105–1108, Sept 2017.

[15] S. Zhang, I. Syrytsin, and G. F. Pedersen, "Substrate-insensitive phased array with improved circularly-polarized scan angle for 5G mobile terminals," in *2017 12th European Conference on Antennas and Propagation (EUCAP)*, Apr. 2018.

[16] S. Zhang, I. Syrytsin, and G. F. Pedersen, "Compact beam-steerable antenna array with two passive parasitic elements for 5G mobile terminals at 28 GHz," *IEEE Trans. Antennas Propag.*, 2018,(in press).

[17] R. Hussain, A. T. Alreshaid, S. K. Podilchak, and M. S. Sharawi, "Compact 4G MIMO antenna integrated with a 5G array for current and future mobile handsets," *IET Microwaves, Antennas & Propagation*, vol. 11, no. 2, pp. 271–279, 2017.

[18] I. Syrytsin, S. Zhang, G. F. Pedersen, K. Zhao, T. Bolin, and Z. Ying, "Statistical investigation of the user effects on mobile terminal antennas for 5G applications," *IEEE Trans. Antennas Propag.*, vol. 65, pp. 6596–6605, Dec 2017.

[19] T. Wang, M. Umehira, H. Otsu, S. Takeda, T. Miyajima, and K. Kagoshima, "A twin cylinder model for moving human body shadowing in 60GHz wlan," in *2015 21st Asia-Pacific Conference on Communications (APCC)*, pp. 188–192, Oct 2015.

[20] K. Zhao, J. Helander, D. Sjöberg, S. He, T. Bolin, and Z. Ying, "User body effect on phased array in user equipment for the 5G mmwave communication system," *IEEE Antenna Wireless Propag. Lett.*, vol. 16, pp. 1847–1850, 2017.

[21] B. Yu, K. Yang, C. Y. D. Sim, and G. Yang, "A novel 28 GHz beam steering array for 5G mobile device with metallic casing application," *IEEE Trans. Antennas Propag.*, vol. 66, pp. 462–466, Jan. 2018.

[22] I. Syrytsin, S. Zhang, and G. F. Pedersen, "User impact on phased and switch diversity arrays in 5G mobile terminals," *IEEE Access*, vol. 6, pp. 1616–1623, 2018.

[23] J. Bang and J. Choi, "A SAR reduced mm-wave beam-steerable array antenna with dual-mode operation for fully metal-covered 5G cellular handsets," *IEEE Antenna Wireless Propag. Lett.*, vol. 17, pp. 1118–1122, Jun. 2018.

[24] B. Xu, K. Zhao, B. Thors, D. Colombi, O. Lundberg, Z. Ying, and S. He, "Power density measurements at 15 GHz for RF EMF compliance assessments of 5G user equipment," *IEEE Trans. Antennas Propag.*, vol. 65, pp. 6584–6595, Dec 2017.

[25] I. Syrytsin, S. Zhang, G. F. Pedersen, and Z. Ying, "User effects on the circular polarization of 5G mobile terminal antennas," *IEEE Trans. Antennas Propag.*, vol. 66, pp. 4906–4911, Sep. 2018.

[26] Y. J. Cheng and Y. Fan, "Millimeter-wave miniaturized substrate integrated multibeam antenna," *IEEE Trans. Antennas Propag.*, vol. 59, pp. 4840–4844, Dec 2011.

[27] L. Wang, M. Garcia-Vigueras, M. Alvarez-Folgueiras, and J. R. Mosig, "Wideband H-plane dielectric horn antenna," *IET Microwaves, Antennas Propagation*, vol. 11, no. 12, pp. 1695–1701, 2017.

[28] W. Hong, K. H. Baek, and S. Ko, "Millimeter-wave 5G antennas for smartphones: Overview and experimental demonstration," *IEEE Trans. Antennas Propag.*, vol. 65, pp. 6250–6261, Dec 2017.

Igor Syrytsin was born in Saratov, Russia, in 1988. He received the B.S. degree in electronic engineering and IT and M.S. degree in wireless communication systems from Aalborg University, Aalborg, Denmark, in 2014 and 2016, respectively. Currently, he is pursuing the Ph.D. degree at Department of Electronic Systems at Aalborg University. His research interests include mm-wave mobile antenna design and interactions between user and mobile antennas.

Shaui Zhang received the B.E. degree from the University of Electronic Science and Technology of China, Chengdu, China, in 2007 and the Ph.D. degree in electromagnetic engineering from the Royal Institute of Technology (KTH), Stockholm, Sweden, in 2013. After his Ph.D. studies, he was a Research Fellow at KTH. In April 2014, he joined Aalborg University, Denmark, where he currently works as Associate Professor. In 2010 and 2011, he was a Visiting Researcher at Lund University, Sweden and at Sony Mobile Communications AB, Sweden, respectively. He was also an external antenna specialist at Bang & Olufsen, Denmark from 2016-2017. He has coauthored over 40 articles in well-reputed international journals and over 14 (US or WO) patents. His research interests include: mobile terminal mm-wave antennas, biological effects, CubeSat antennas, UWB wind turbine blade deflection sensing, MIMO antenna systems, and RFID antennas.

Gert Frølund Pedersen was born in 1965. He received the B.Sc. and E.E. (Hons.) degrees in electrical engineering from the College of Technology in Dublin, Dublin Institute of Technology, Dublin, Ireland, in 1991, and the M.Sc.E.E. and Ph.D. degrees from Aalborg University, Aalborg, Denmark, in 1993 and 2003, respectively. Since 1993, he has been with Aalborg University where he is a Full Professor heading the Antenna, Propagation and Networking LAB with 36 researchers. He is also the Head of the Doctoral School on wireless communication with some 100 Ph.D. students enrolled. His research interests include radio communication for mobile terminals especially small antennas, diversity systems, propagation, and biological effects. He has published more than 175 peer reviewed papers and holds 28 patents. He has also worked as a Consultant for developments of more than 100 antennas for mobile terminals including the first internal antenna for mobile phones in 1994 with lowest SAR, first internal triple-band antenna in 1998 with low SAR and high TRP and TIS, and lately various multiantenna systems rated as the most efficient on the market. He has worked most of the time with joint university and industry projects and have received more than 12 M$ in direct research funding. He is currently the Project Leader of the SAFE project with a total budget of 8 M$ investigating tunable front end including tunable antennas for the future multiband mobile phones. He has been one of the pioneers in establishing over-the-air measurement systems. The measurement technique is now well established for mobile terminals with single antennas and he was chairing the various COST groups (swg2.2 of COST 259, 273, 2100, and now ICT1004) with liaison to 3GPP for over-the-air test of MIMO terminals. He is currently involved in MIMO OTA measurement.

Arthur S. Morris III (S'90–M'91–SM'04–F'13) received the B.S. degree in physics and also in electrical engineering and M.S. and Ph.D. degrees in electrical engineering from North Carolina State University (NCSU), Raleigh, NC, USA, in 1983, 1986, and 1993, respectively. As a Scientist/Engineer with a concentration on physical electronics and electromagnetic fields for over 30 years, he has contributed to device technologies ranging from traveling-wave tubes to millimeter-wave heterojunction bipolar transistors and has developed products for markets from high-voltage instrumentation to broadband communication systems. In 1999, he joined Coventor, to lead software and hardware development to drive the transition of microelectromechanical systems (MEMS) and microsystems from the laboratory into products for RF and optical applications. He is a cofounder of Wispry Inc., Irvine, CA, USA, which spun out of Coventor in 2002. He is the company's Chief Technical Officer (CTO) and leads the development of high-performance programmable RF products for high-volume markets utilizing MEMS, CMOS, and advanced packaging. He is an Adjunct Professor with NCSU.

Paper F

Characterization and Modeling of the User Blockage for 5G

Peiye Liu, Igor Syrytsin, Shuai Zhang, Jesper Ødum Nielsen, and Gert Frølund Pedersen

The paper has been submitted to:
IEEE Transactions on Antennas and Propagation, 2019.

Abstract

In this work a stochastic 3D user shadowing model is presented which can be used in the frequency range 28 GHz ±6 GHz. *The user shadowing model is based on measurements with 18 subjects of different heights and gender and modeled as a stochastic process which follows the Gaussian distribution in each of the three defined spatial regions. To characterize the user shadowing pattern new metrics of shadowing CDF and USIR are proposed. The proposed model can be used for ray tracing or link simulations as it has been shown that any horizontally polarized mobile antenna can be applied to the model.*

At the time of the creation of this PDF, the paper was still under review and is therefore not included in this public version. The reader is therefore referred to the publication channel or if needed to contact the author for a copy of the paper.

DOI:

Characterization and Modeling of the User Blockage for 5G

Peiye Liu, Igor Syrytsin, Shuai Zhang, *Senior Member IEEE*, Jesper Ødum Nielsen, Gert Frølund Pedersen, *Senior Member IEEE*

***Abstract*—In this work a stochastic 3D user shadowing model is presented which can be used in the frequency range around 28 GHz ±6 GHz. To characterize the user shadowing pattern new metrics of shadowing CDF and USIR are proposed. The user shadowing model is based on measurements with 18 subjects of different heights and gender. For simplicity the user shadowing pattern is divided in three regions based on the mean shadowing pattern obtained from the measurements. Each of the spatial regions is modeled as a stochastic process which follows the Gaussian distribution. It has been shown that any horizontally polarized mobile antenna is compatible with the presented model. The proposed user shadowing pattern model can be directly used for the 5G mm-wave ray tracing or link simulations.**

***Index Terms*—Mobile terminal antenna, antenna array, 5G, mm-wave, shadowing, user impact, blockage.**

I. INTRODUCTION

IN the recent few years the 5th generation (5G) wireless communication systems have attracted a high level of interest and been developed rapidly. One of the main purposes of 5G is to provide users with high throughput. This goal can be achieved in multiple different ways, for example increasing the number of transmit and receive antennas or increase the bandwidth of the system. For the 5G massive MIMO systems, besides the frequencies below 3.5 GHz, microwave and millimeter wave frequencies will also be occupied in order to obtain wider bandwidth [1]. In 2017, multiple candidate bands between 24.25 GHz and 86 GHz have been proposed at the World Radiocommunication Conference [2]. However, at the microwave and millimeter wave frequencies the path loss becomes more severe, but transmitting with more power is not a viable solution as it will create more interference to the co-channel cells and also will drain the battery of the mobile terminal more quickly. One of the solutions to this problem is to increase the gain of the antennas [3]. Base stations are already equipped with multiple high gain antennas, but at mobile terminal side, a high gain antenna are more challenging to implement because of the device size limitations. Furthermore, a spatial beamforming technique will be required in order to steer the main beam of the antenna towards the base station. A full spatial coverage is also required from the handset antenna which can be oriented in any possible way. Spatial coverage can be characterized by using a coverage efficiency metric, which has been proposed in [4] and then used to assess the performance of the 5G handset antennas in [5]. Then, in [6] the circular polarized coverage efficiency metric has been proposed in order to characterize the circular polarized handset antennas.

Furthermore, the handset antenna and the user cannot be so easily separated and significant blockage from the user is expected at the mm-wave frequencies [7], but the body loss is much lower than that at sub 6GHz bands. Blockage from the user is not as severe at 28 GHz as that at 60 GHz [8], but still should be considered when assessing the performance of the 5G mm-wave mobile communication link. 3GPP community has already proposed some models for the user shadowing [9]. However, those models are highly inaccurate and extremely simplified. One of the modes represents the user blockage by a rectangular space with -30 dB attenuation inside and another model takes into the account the diffractions around the user's body. In real life the user's body shadow shape is more complicated than a rectangular space, and also in addition to the diffractions, creeping waves and surface waves will change the shape of the user blockage considerably. To characterize the user blockage in [7] it has been proposed to use the metric of shadowing power ratio (SAPR) in addition the already existing coverage efficiency metric. At 15 GHz the user effects has been measured with a phased array in [10], and a strong shadowing effect from the human body, which is around 20-25 dB, is observed and significant losses in the coverage efficiency have been recorded. The user shadowing pattern can be affected by many aspects, such as main beam direction, antenna polarization and directivity, antenna position on the ground plane, user's grip and many more others. The effects of the phone case on the performance of the antennas has been investigated in [11] and significant changes in the shape of the radiation pattern have been observed. However, by adding the two-tilted layers of coupled metal strips, placed at the borders of the frame, the blockage by the metal frame is reduced significantly as shown in [12]. The investigation of user effects on the phased and switch diversity antenna arrays in [13] has shown that phased arrays cannot always have the best performance. Also the user effects on the switch beam high gain ($G_{max} \geq 7$ dBi) antennas are investigated in [14]. It has also been shown that user effects can be mitigated by using antenna array diversity in [15]. Finally, in [16] the blockage from the user's hand and body is measured with the phased array in the indoor environment. However, in this case only the received power is measured and no spatial distribution has been given. The model proposed in that manuscript only works for the specific handset-base station setup and can not be considered a general model, because user blockage highly

---

This work was supported by the User Shadowing project with Huawei Gothenberg, Sweden.(Corresponding author: Shuai Zhang).

Peiye Liu, Igor Syrytsin, Shuai Zhang, Jesper Ødum Nielsen, and Gert Frølund Pedersen are with the Antennas, Propagation and Millimeter-wave Systems section at the Department of Electronic Systems, Aalborg University, Denmark (email: {igs,sz,gfp}@es.aau.dk).

depends on the such parameters as handset antenna oritation, height, antenna-user distance and so on which are investigated in this paper to have a accuracy model of the user blockage for 5G terminals.

In this paper a user shadowing model based on the measurements with the 18 users with the most critical gestures is presented. In Section II, the measurements are done in the anechoic chamber with the user applying different gestures in order to find out which handset positions have the biggest impact on the user blockage. A new metric of shadowing cumulative distribution function (SCDF) is proposed to characterize the variations inside the user shadowing region. Then in Section III, it has been shown that the user shadowing intensity (USI) can be reliably extracted from the measurements with the user with help of the free space radiation pattern of the DUT. Furthermore, it has been found that the de-embedded user shadowing intensity is not sensitive with the antenna beam width with the same polarization. Next, in Section IV, the measurements with multiple user are conducted. In respect to measurement campaign in [7], 18 subjects have been chosen in consideration of the human height distribution. In this section, the mean radiation patterns and USIs for both data and dual hand modes are presented and a new extended metric of user shadowing intensity ratio USIR is introduced. Finally in Section V, the stochastic model of the USI is proposed. The modeled mean USI (Obtained from multiple random process realizations) is compared with the measured mean USI and shows high similarities. The model is much more closer to the actual measured USP than the 3GPP models and considers both diffractions and creeping waves.

II. CRITICAL GESTURE INVESTIGATION

In this section, multiple common user gestures are investigated. Multiple measurements are performed to find out which user gestures yield the highest blockage. Besides the radiation patterns, two other metrics will be used in the work to assess the user shadowing. First, the SAPR metric is applied to quantify the shadowing power together with the creeping waves and diffractions. The amount of the power in the shadow region in comparison with the total power radiated by the antenna in the free space is called SAPR which is proposed in [7].

The SAPR is defined as:

$$
\begin{aligned}
&SAPR(\delta\theta,\delta\phi)\\
&=\frac{P_{shadow}}{P_{total}}\\
&=\frac{\Delta\phi\Delta\theta\sum_{\theta_{min}}^{\theta_{max}}\sum_{\phi_{min}}^{\phi_{max}}(P_{ant,V}(\theta,\phi)+P_{ant,H}(\theta,\phi))sin(\theta)}{\Delta\phi\Delta\theta\sum_{1^\circ}^{140^\circ}\sum_{-180^\circ}^{180^\circ}(P_{ant,V}(\theta,\phi)+P_{ant,H}(\theta,\phi))sin(\theta)}
\end{aligned}
\tag{1}
$$

In the formula, P_{shadow} describes the power in the shadow (in the chosen area of a radiation pattern) and integrated from the center of the shadow (at 0°) towards both positive and negative axes in angle ϕ and from the start to the end point in angle θ. P_{total} is the TRP with the user. The lower the SAPR level is, the stronger the shadow loss is in the chosen spatial region.

Then, the SCDF is used to show how the power intensity within the user shadowing region is distributed.

The SCDF is defined as:

$$F(x)=P(X\leq x) \tag{2}$$

P is the probability of the power of spatial piont X in the shadowing region takes on a value less than or equal to a certain power level x.

A. Measurement setup

In this paper, all the measurements are performed in the anechoic chamber at the Antennas, Propagation and Millimeter wave Systems laboratory at Aalborg University. The measurement setup is shown in Fig. 1. The styrofoam column with the adjustable height is used to fix the position of the antenna under test (AUT), while the user stands on the platform with its back against the wooden pole, holding the AUT. During the measurement, the platform turns in azimuth angle ϕ, and then the probe on a robot arm scans in inclination angle θ with steps. The wooden pole is added for the user's safety, as in the measurement the platform is raised up to around 3.5 m height to ensure that the AUT is at the center of the measurement system. The system is able to measure in the maximum range of -180° to 180° in ϕ angle, and 1° to 140° in θ angle. The bottom 40° is not considered as the metal platform will totally block that area.

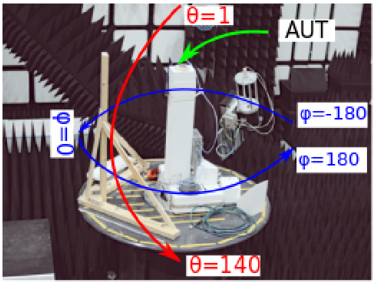

Fig. 1. Measurement setup of the anechoic chamber.

In the measurements a single wideband dipole antenna element, located in the center of the array, is used as a AUT [7]. The chosen antenna operates from 28 GHz to 34 GHz [7]. Fig. 2(a) shows the free space radiation pattern. A shadow seen at $\phi=0^\circ$ is due to the blockage by the wooden pole. However, the size of the shadow from the pole is very small in comparison to the blockage from the person's body. During the measurement, a person is standing in between the AUT and the wooden pole, which means that the wooden pole will be behind the user's back and is not visible from the viewpiont of the AUT in the measurement. Thus, most of the power will be absorbed and blocked by the user, or reflected back in the free space and the effect of the wooden pole can be neglected in user shadowing investigations. SAPRs at the four operating frequencies are shown in Fig. 2(b) with the user for the same gesture. To compare the antenna performance within the frequency range, the miss-match losses and radiation efficiency of the antenna are calibrated out. It can be clearly seen that SAPR does not depend on frequency in the operation range of the AUT, which is why further measurements are only performed a single frequency 28 GHz, which will increase the measurement time considerably .

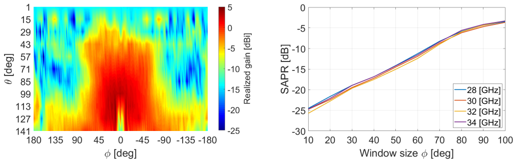

(a) (b)

Fig. 2. (a) Free space radiation pattern of the AUT, (b) SAPRs of four operating frequencies with the user in the same gesture.

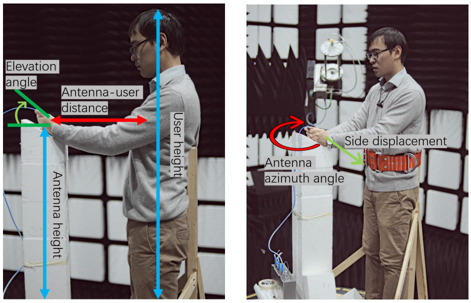

(a) (b)

Fig. 3. Setup of the user with a mobile phone at (a) data (single hand) mode, (b) dual hand mode.

As in optics, the user shadow size and strength are affected by the antenna-user related position. Five different sets of gestures in both data (single hand) and dual-hand modes are concidured: the antenna-user related height, the antenna-user distance, the antenna elevation angle, the antenna azimuth angle and the antenna side displacement are shown in Fig. 3. However, unlike the antenna-user related height and the antenna-user distance, the shadow power is not sensitive to the antenna elevation angle, the antenna azimuth angle, and the antenna side displacement in both data and dual hand modes. Thus, in this section only the height and the distance assessments will be shown.

B. Relative antenna-user height

First, measurements are conducted with the different relative antenna-user heights. The user's height is fixed as only a single person is participating in the measurement. The only variable is the AUT's height which is changed by adding different height styrofoam blocks on top of the column. The AUT is positioned at 100 cm, 115 cm and 130 cm above the platform which correspond to the user's waist, belly and chest height, respectively. In the paper these three heights are named as low, medium and high, respectively. The sampling resolution in θ and ϕ in this setup is 14° and 2° respectively, and chosen to limit the measurement time to around 20 minutes. Shown in Fig. 4, as expected, the higher the AUT is placed the lower is the shadow appears in the plots, and the shadow widths are the same in all heights. The shadow to the right from 0° in the plot for the data mode and at both sides of the user in dual hand mode is due to the blockage of user's hand and arm.

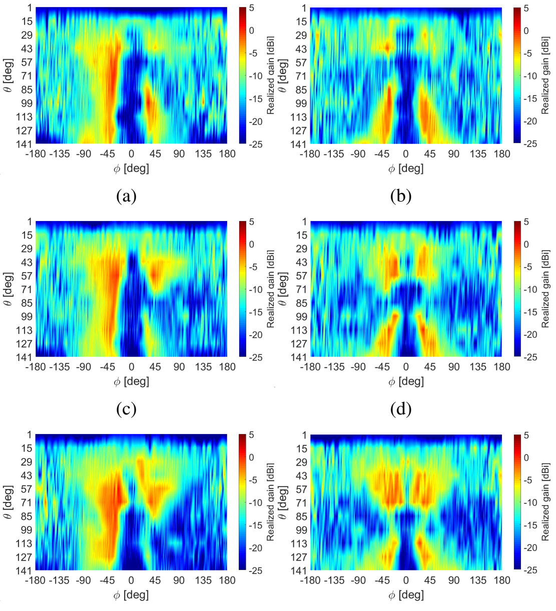

(a) (b) (c) (d) (e) (f)

Fig. 4. USP of (a) low AUT height for data mode, (b) low AUT height for dual hand mode, (c) medium AUT height for data mode, (d) medium AUT height for dual hand mode, (e) high AUT height for data mode, (f) high AUT height for dual hand mode.

The strongest shadowing can be observed within $\phi = 0° \pm 15°$, and the whole body shadow is about 80° wide in ϕ, which can be observed in Fig. 4. Then SAPRs and SCDFs are calculated based on these limits, and shown in Fig. 5. For the dual-hand mode, it is clear that the SAPR increases with the height of the AUT for all ϕ window sizes in Fig. 5(b) and Fig. 5(d). The difference is around 3 dB within the small window sizes, and gets even small when the window size is close to the maximum shadow width 80°. For the small window sizes the main difference between the three patterns is the shadow height which mostly dictates the SAPR value. But as the window size increases, even more creeping wave and diffractions are accumulating in the shadowing region and thus the difference between the curves is small. In data mode, the shadow height difference is not very clear for the low and medium AUT heights, as SAPRs for the two gestures are quite similar in Fig. 5(c). But for high height the shadow is obviously small. The SAPR snd SCDF figures show the same trend and difference as dual hand mode in Fig. 5(d) and Fig. 5(b). In most cases, the user shadow loss in dual hand mode is 1 to 2 dB smaller than that in data mode because of less blockage of hand and arm and more creeping wave in dual hand mode. Finally, it can be concluded that the user shadow is sensitive to the relative antenna-user height and it gets smaller as the relative height increases.

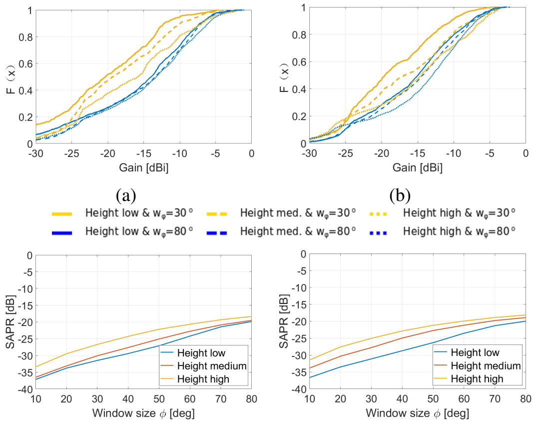

(a) (b)

(c) (d)

Fig. 5. SCDF comparison of different heights for (a) data mode, (b) dual hand mode, and SAPR comparison for (c) data mode, (d) dual hand mode.

C. Antenna-user distance

The second critical gesture parameter is the antenna-user distance. In the original setups, the distance between the AUT and the user is 40 cm. Then, an extra styrofoam block is added between the user and the safety pole to decrease the distance to 30 cm. The relative antenna-user height is kept corresponding to the user's waist (low height). As both shadow height and width will be affected by the antenna-user distance, and the distance difference is small in respect to the user's height, to see the more accurate difference in the radiation patterns, the sampling step in θ is set as 5° instead of 14°. To reduce the measurement time, the probe on the robot arm scans in θ while the platform turns with steps in ϕ in antenna-user distance investigation. And the step in ϕ is set as 5°, the test range is set as $-105°$ to $105°$ in ϕ, and 5° to 130° in θ to keep the measurement time within 20 minites. As expected, shown in Fig. 6, the shadow width is larger when the distance is small for both data and dual hand modes. The same trend can be observed for the height of the shadow.

Finally, SCDFs and SAPRs are calculated for the two different antenna-user distances and shown in Fig. 7. It can be observed, that the SAPR for the setup with the distance of 40 cm is 2 to 3 dB higher than that for the distance of 30 cm for both data and dual hand modes. The SCDF distributions agree well with the SAPR results and show the similar trend. Similarly to the measurements for the height investigation, the user shadow loss in the dual-hand mode is smaller than that in data mode. It can be concluded that the user shadow is sensitive to antenna-user distance and it gets smaller as the distance increases.

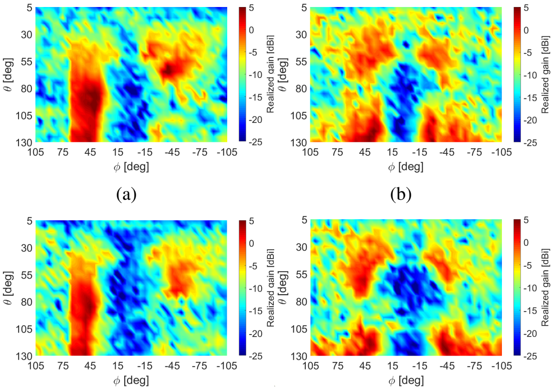

(a) (b)

(c) (d)

Fig. 6. USP of the setup with (a) 40 cm antenna-user distance for data mode, (b) 40 cm antenna-user distance for dual hand mode, (c) 30 cm antenna-user distance for data mode, (d) 30 cm antenna-user distance for dual hand mode.

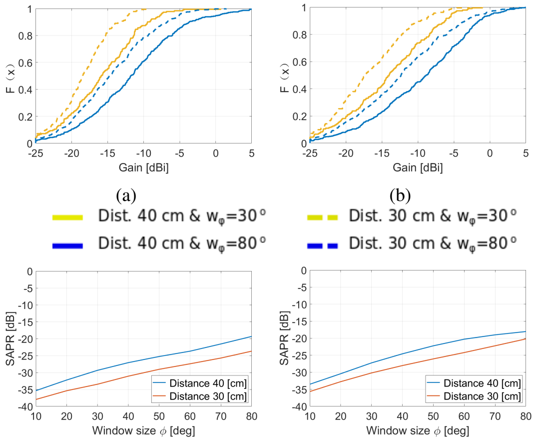

(a) (b)

(c) (d)

Fig. 7. SCDF comparison of different heights for (a) data mode, (b) dual hand mode, and SAPR comparison for (c) data mode, (d) dual hand mode.

In this section it has been shown that two critical gestures are the relative antenna-user height and the antenna-user distance. Thus, when conducting a measurement campaign with the multiple users, these two variables will be taken into consideration.

III. USER SHADOWING INTENSITY

Besides relative antenna-user positions, antenna gain and beam width may also affect the USP. While it is certain that high gain can decrease the user shadowing loss, to further investigate whether the user shadowing shape and loss depends on the antenna beam width, three different horizontally polarized endfire antennas are measured. Sketched radiation patterns of the antennas are shown in Fig. 8. The antennas used for the measurements are the center element in arrays. The AUT 1 is the same one from the former measurements, the AUT 2 is the one proposed in [17] and has the widest beamwidth of the three, and the AUT 3 is the antenna used in [13] which have narrowest beamwidth. In the measurements, exactly the same positions of AUTs and user gestures are applied to minimize measurement error. Antenna efficiency and miss-match losses are calibrated out. Free space radiation patterns are shown in Fig. 9, and the beam width difference is obvious.

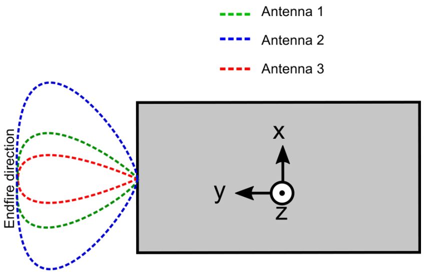

Fig. 8. Sketch of the antenna radiation patterns used in this investigation.

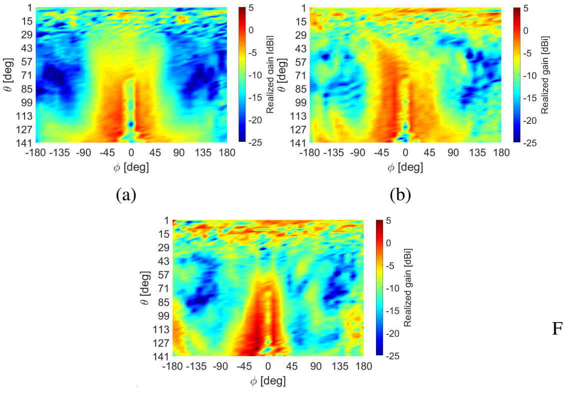

(a)

(b)

(c)

Fig. 9. Free space radiation pattern of (a) AUT 1, (b) AUT 2 and (c) AUT 3.

Then, the antennas are measured in both data and dual hand modes with the antenna height of 115 cm and antenna-user distance of 40 cm. Radiation patterns of three antennas in data mode are shown in Fig. 10. As expected, the widths and heights of the user's shadows are similar, but diffraction around the shadows differs as the illumination region depends on the beamwidth of the antennas. Next, to calibrate out the antennna gain difference and investigate the real shadowing intensity, the user shadowing intensity (USI) is extracted from the free space radiation patterns and the radiation patterns with the user by the method defined in Equation. 3.

$$USI(\theta,\phi) = 10\cdot\log 10(G_{free}(\theta,\phi)/G_{user}(\theta,\phi)) \tag{3}$$

The values of G_{user} and G_{free} are the measured gain with and without the user for the AUT in exactly the same position and orientation. Processed data is shown in Fig. 11. The bigger the value of the shadowing intensity the stronger is the shadowing. It can be noticed, that the shadowing from the head is less severe for the AUT 3 which have the highest realized gain. However visually all three de-embedded USIs look similar. Then, SCDFs of the de-embedded USIs are plotted in Fig. 12. For the window sizes of 30° and 80° in both data and dual hand modes the observed difference is less than 2 dB which is not so significant and can be comparable to the measurement uncertainty of the chamber, equipment and user gesture.

It can be concluded that the de-embedded USI is not too sensitive to the AUT beam width and the antenna type. The de-embedding can be done for different types of the antenna with the accuracy of up to 2 dB. The shown de-embedding procedure will be used in statistical measurements in order to extract the USIs for the multiple users and to make the model.

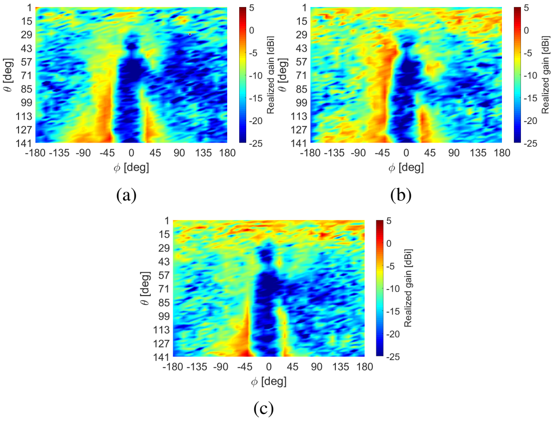

(a)

(b)

(c)

Fig. 10. USI of (a) AUT 1, (b) AUT 2 and (c) AUT 3 for data mode.

IV. STATISTICAL MEASUREMENT

In this section, multiple measurements with different subjects will be performed. Already in the Section II it has been found that both SAPR and SCDF depends mostly, on the relative antenna-user height and also the distance between the person and the mobile device. Thus, here it has been chosen to use the two gestures with different the relative antenna-user height. As shown in Fig. 13, both data and dual hand mode measurements will be performed. The first AUT position is to user's waist in Fig. 13(a) representing the most common gesture when a user is operating the mobile device to access the social networks, watch videos or write text messages (in the case of dual-hand mode in . 13(c)). The second chosen gesture is at height of the user's chest in Fig. 13(b) and Fig. 13(d) and usually applied when user is operating the mobile device in order to take photos or make video calls. Furthermore, the gestures are chosen such so the user is

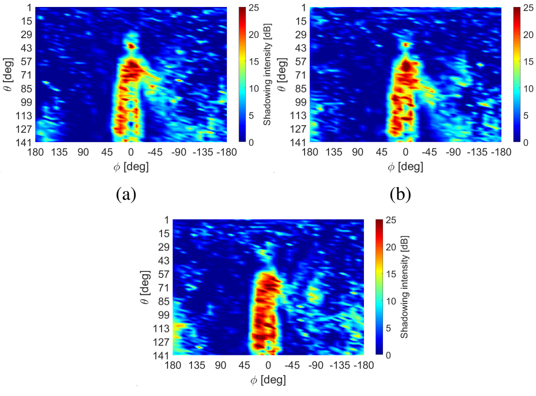

(a) (b) (c)

Fig. 11. De-embedded USI of (a) AUT 1, (b) AUT 2 and (c) AUT 3 for data mode.

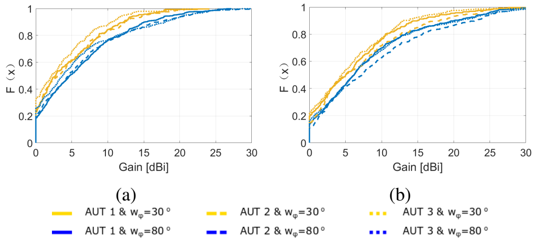

(a) (b)

Fig. 12. SCDF of De-embedded USI comparison of AUT 1, AUT 2 and AUT 3 for (a) data mode, (b) dual hand mode.

holding the AUT comfortably, which means that the AUT height and distance between the user and AUT will be adjusted accordingly to the user's height and most comfortable grip position.

(a) (b) (c) (d)

Fig. 13. Gestures used in the statistical measurement: (a) data mode low position, (b) data mode high position, (c) dual hand mode low position, (d) dual hand mode high position.

A. Sample Analysis

To find the right user sample for the measurement it is important to quantify the difference between male and female subjects in terms of radiation pattern, SAPR and SCDF. As it has been already shown in [7], the height of the user does play a significant role on the SAPR. However, until now, only male subjects have been measured for the frequencies around 28 GHz. First, to compare the user effect of the male to female subjects the radiation patterns are measured for two subjects with the same chosen height of 174 cm. The measurements have been done both in data and dual hand modes for all four gestures shown in Fig. 13. Next, four extra radiation patterns have been generated by mirroring the patterns around $\phi = 0°$ to take into account left and right-handed users and also to compensate for the non-symmetrical grip uncertainties in dual hand mode. In dual hand mode, the gesture will never be exactly symmetrical around the center of the mobile device as the most comfortable grip for the most subjects will never be exactly symmetrical.

Then, the mean USI have been computed for male and female subject and shown in Fig. 14. The the two mean radiation patterns are visually quite similar, but it can be noticed that the radiation pattern for the female subject does indeed have a triangle shaped shadowing around neck area because the subject have a long hair lying on her shoulder. An average women have longer hair than an avarage man, and thus to have better statistical results the female subjects will also be included in the measurement campaign.

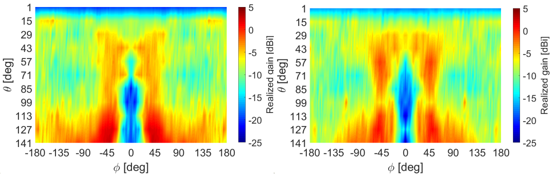

(a) (b)

Fig. 14. Mean radiation pattern of (a) male and (b) female subjects with a height of 174 cm.

However, in the SAPRs and SCDFs, calculated from the two mean radiation patterns, the curves for the male and female subjects are very similar as shown in Fig. 15. Thus, it has been chosen to mix the male and female subjects together in one measurement campaign to reduce the total number of subjects.

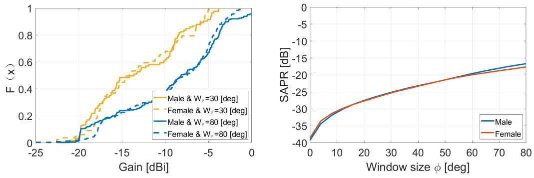

(a) (b)

Fig. 15. Comparison of (a) SCDF and (b) SAPR for the male and female subjects.

The CDF distributions of men and women heights are shown in Fig. 16(a), which are based on measurement done in [18]. It can clearly be seen that men and women have very different mean heights, but the shape of the distribution is similar (The PDF will look like Gaussian bell curve). Thus when the two Gaussian distributions are put together the obtained new distribution will also be Gaussian. Furthermore, it was very difficult to find very short men and women (< 155cm) in Denmark. Hence, the men and women are combined together as samples and the resulting height PDF is shown in Fig. 16(b), which is approximately Gaussian with the mean of 175 cm. The more detailed description of the sample can be seen in Table I.

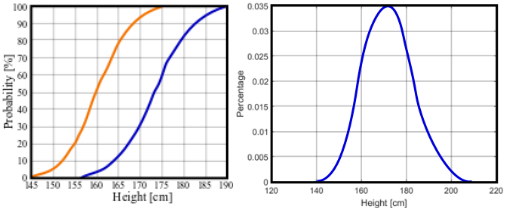

(a) (b)

Fig. 16. (a) CDF functions of the male and female height, (b) distribution of the sample height.

Table I. Number of chosen subjects for each corresponding height range.

Height [cm]	<155	155-162	162-170	170-175	175-180	180-188	> 188
# of subjects	1	2	5	2	5	2	1

B. *Measurement Results*

The measurements have been performed from 1° to 140° in θ and -180° to 180° in ϕ. In all of the measurements only one antenna has been used, which is the same one as in Section II. Only a single frequency of 28 GHz has been considered, as it has been already shown that in order to see any frequency dependency, the frequency range of at least 15 GHz should be chosen, but a mobile 5G antenna with such bandwidth is difficult to realize. However, because in measurements the antennas are pointing towards the user and the user hold angles are from 30° to 60°, the power collected by the probe at the $\theta \leq 42°$ is very low compared with the rest of the measured power. It has been chosen to cut this region in order to speed up the measurement time. Short measurement time facilitates decreasing the probability of the error due to user involuntary movements.

The mean radiation patterns are calculated for the data and dual hand modes from both gestures for all measurements with 18 people and shown in Fig. 17. Furthermore as in Fig. 14 extra radiation patterns are added to the mean by mirroring the existing measured radiation patterns around $\phi = 0°$ which makes the mean radiation pattern exactly symmetrical (accounting for the right and left-handed users). The mean radiation patterns for the data and dual hand mode look very similar, but a little bit more shadowing from the hands can be observed in dual hand mode. This is expected because the user holds the mock-up more tight in dual hand mode than in data mode, also hand and arm blockage in data mode is reduced by mirroring.

Nonetheless, the user shadowing cannot be assessed properly if the radiation pattern is presented in the way in Fig. 17.

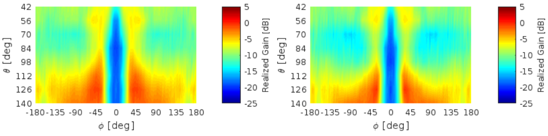

(a) (b)

Fig. 17. Measured mean radiation pattern calculated from 18 subjects for (a) data mode and (b) dual-hand mode.

In order to see the true user shadowing intensity, the antenna pattern need to be de-embedded from the total radiation pattern based on the method shown in Section III. Even if multiple users have been measured it is possible to de-embedded the USIs using two radiation patterns with different pointing angle of antenna in the free space. This can be done because users usually hold the mobile device in a very similar way in respect to each other [19]. One free space radiation pattern has been used for each of the gestures(high and low in Fig. 13) as shown in Fig. 18(a) for the top gesture (elevation angle of 60°) and the bottom gesture (elevation angle of 30°) in Fig. 18(b). it can clearly be noticed that the radiation patterns are very similar, because of the very wide beamwidth of the antenna [20]. The only significant difference between figures is the beam height, which is also happened while user applying different heights gestures.

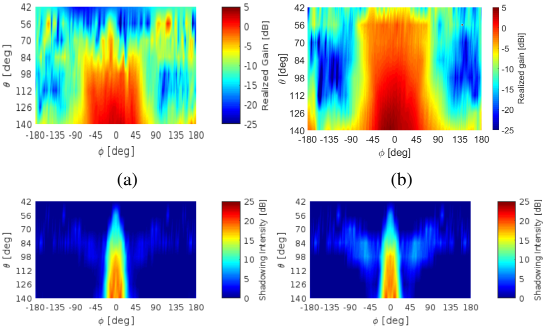

(c) (d)

Fig. 18. Mean plot of (a) Free space radiation pattern in high position, (b) free space radiation pattern in low position, (c) USI for data mode, (d) USI for dual hand mode.

The de-embedded USIs for the data and dual-hand modes are shown in Fig. 18(c) and Fig. 18(d) respectively. No significant difference can be observed between the two. Again, the shadowing from the hands in dual hand mode is about 2 dB higher than that in data mode visually. In order to assess further the difference between the two modes both SAPR and SCDF is computed. The SCDF computed for the window sizes of 30° and 80 ° is shown for data and dual hand modes in Fig. 19(a). It can clearly be seen that the distribution of the shadow power is similar for the data and dual hand modes.

The characterize USI and a metric of shadowing power ratio can be changed slightly to produce user shadowing intensity ratio (USIR). USIR can be also calculated in theta and phi direction. Here phi window is the same as the one chosen in

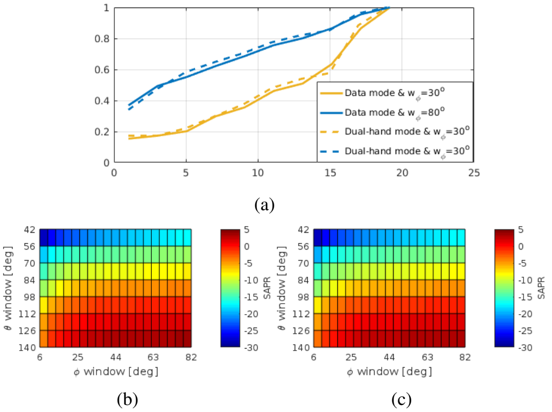

(a)

(b) (c)

Fig. 19. (a) SCDF of the data and dual hand modes and USIR calculated for both theta and phi windows for (b) data mode and (c) dual-hand mode.

Equation 1, but the theta window expands form the top of the plot to the bottom and always begins at the top:

$$\delta\theta = \theta_2 - \theta_{min} \tag{4}$$

where, θ_{min} is a constant minimum measured theta value and θ_2 is variable theta value for a given window size. Furthermore, instead of comparing the power in the window to the total power and isotropic antenna is chosen as a reference. Authors think that this metric provides better overview of the distribution of shadowing intensity in space. Furthermore, if the shadow is to be modeled then this metric can provide a significant insight on different regions inside the shadow (for example total shadowing region, diffraction/creeping wave region). For example, in Fig. 19(b) the θ coordinate of 98° means that the USIR values in this row calculated for the θ window which spans from 42° to 98°. The USIR in ϕ direction is calculated in the same way as in the previous sections of this paper. It can clearly be seen that there is some a very small difference in the USIR between data and dual hand modes. Also because the SCDF for the data and dual hand mode are the same it can be concluded that all results from all measurements could be put together in order to make more robust model of the USI from the bigger sample size.

V. USER SHADOWING PATTERN MODELING

In this section the model of the USI will be presented. The proposed model is based on the statistical measurements with the multiple users, which have been presented in Section IV. The proposed model will be compared to the measured results by using metrics of mean USI, variance and USIR.

As discussed earlier, it has been decided to combine the results from the data and dual-hand modes as they has been shown to be similar in Section IV. This is done in order to obtain more data points and make a base for the model more robust. First, the mean USI is calculated from all of the available measurements is shown in Fig. 20(a). It can be noticed that this USI looks quite similar to the USI for data or dual hand modes in Fig. 18(c) or Fig. 18(d). The approximate size of the user blockage is 40° to -40° in ϕ, while outside this range the shadow is very small. Furthermore, the plot of the variance for each spatial point on the 3D plot is shown in Fig. 20(b). It can be seen big variance appears at around $\phi = \pm 16°$. This phenomenon occurs is due to the difference of user's widths, comfortable distances to the AUT they choose and also diffractions and creeping wave presents at body edge. Finally, the plot for USIR is shown in fig. 20(c) which looks extremely similar to either plot for data or dual hand mode displayed in Fig. 19(b) and Fig. 19(c).

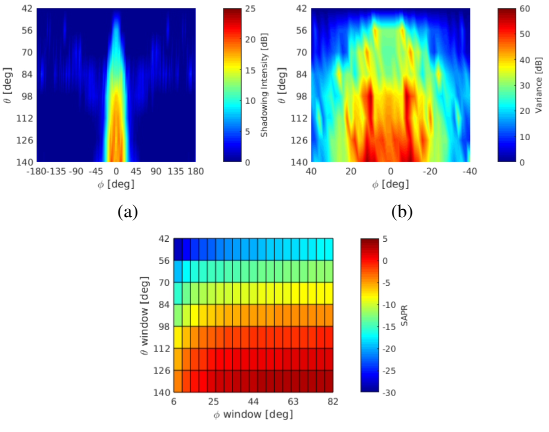

(a) (b)

(c)

Fig. 20. Combined results of the data and talk mode: (a) USI, (b) variance, (c) USIR.

A. USI Modeling Procedure

In this paper, it has been chosen to model the USI as a random process. However, visually it is clear that the distribution in the deep body shadow $\phi = \pm 14°$ is different than the distribution in the transitional regions (from shadow to non-shadow) at approximately 40° to 14° and -14° to -40° in ϕ. However, it is not so straight forward to define those regions. This is why it has been chosen to take a look on USIR calculated in ϕ and θ directions. First, USIR is calculated for the variable window size from 2° to 80° in ϕ, where the size of θ window is all the way from 42° to 140°. The $USIR_\phi$ is shown in Fig. 21(a) and it can be noticed that two tendencies for all of the curves can be observed. From 2° to approximately 30° the curve increases steeply, however after 30° all three curves level. Thus, it has been chosen to use two regions for the model: one region of $\Delta\phi = \pm 14°$ and one where $\Delta\phi =$ 28° to 80°. Furthermore, the USIR calculated in θ direction is shown in Fig. 21(b). Here USIR is calculated differently than in Fig. 20(c). Now it has been chosen to use sliding window of 14 ° and then calculate USIR for each position of the window. Here is quite difficult to identify different regions, such as head, shoulder and body regions. However, it can be noticed that for both maximum and minimum curves the sudden jumps can be observed at 42° to 70°. Thus, it can be proposed that shoulder and body regions first begin at $\theta = 70°$. Finally, all three regions are shown graphically in Fig. 21(c), where the region 1 is the region of the body shadow and regions 2 and 3 are the transitional regions.

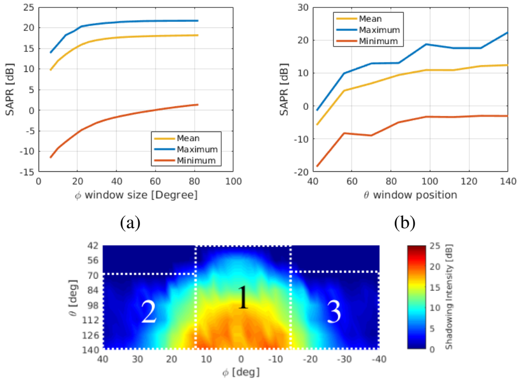

(a)

(b)

(c)

Fig. 21. (a) USIR calculated in the phi window, (b) USIR calculated in the theta window, and (c) regions defined to use in the model for USI.

As it has been discussed earlier, the regions in the USI are based on the mean shadowing pattern from the measurements in both data and dual hand modes. However in order to model the USI as a random process, the radiation intensity in each spatial point within the region should follow a specific distribution. Nonetheless, regions 2 and 3 have similar distributions and only CDFs for the regions 1 and 2 are shown in Fig. 22. Here, in order to make the model more simple, it has been chosen to fit the Gaussian distribution to the empirical curves which is defined as:

$$F(x) = \frac{1}{2}\left[1 + \mathrm{erf}\left(\frac{x-\mu}{\sigma\sqrt{(2)}}\right)\right] \tag{5}$$

The standard deviation, mean and size of the three regions in Fig. 21(c) are given as:

1) region 1: $\mu = 10.5\,\mathrm{dB}$ and $\sigma = 9\,\mathrm{dB}$; size of the region: $\theta = 42°$ to $140°$, $\phi = \pm 14°$. All values are sorted based on big shadow intensities lie on the cener bottom of the plot. Values are sorted in θ direction as the highest values are at the bottom of the plot and the lowest ones are on the top. The values in ϕ plane are sorted so the highest values are in the middle of the plot $\phi = 0°$ and lowest values are at the edges $\phi = \pm 14°$.
2) region 2: $\mu = 8\,\mathrm{dB}$ and $\sigma = 7\,\mathrm{dB}$; size of the region: $\theta = 70°$ to $140°$, $\phi = 40°$ to $14°$. With the same basis in region 1, the values are sorted in ϕ plane so the highest values are closer to the middle of the plot $\phi = 14°$ and the lowest ones are at the edges $\phi = 40°$.
3) region 3: $\mu = 8\,\mathrm{dB}$ and $\sigma = 7\,\mathrm{dB}$; size of the region: $\theta = 70°$ to $140°$, $\phi = -40°$ to $-14°$. Symmetrical to region 2, the values are sorted in ϕ plane so the highest values are closer to the middle of the plot $\phi = -14°$ and the lowest ones are at the edges $\phi = -40°$.

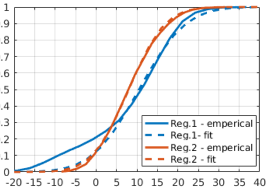

Fig. 22. CDFs of the distributions inside region 1 and 2.

B. Model Accuracy Verification

Then, in order to check if the proposed model is similar to the mean measured model it has been chosen to make a model in the Matlab and run the random process 36 times (corresponds to 18 data mode and 18 dual hand mode measurements) which will yield in the 36 different USIs. Furthermore, it has been chosen to also try to run the simulation for 360 times to see if there is a significant difference between the two calculated mean USIs. The mean USIs and variance corresponding to the 36 and 360 process realizations are shown in Fig. 23. It can be seen that the USIs in two cases look very similar, however variance does converge to the particular shape. It can be seen that highest variance is observed in the total shadow in the middle of the plot and below $\theta = 98°$ which has similar shape to the one observed in Fig. 20(b). Furthermore, it is important to notice that two lines at the edges of the $\phi = \pm 16°$ is where in real life most diffractions will be observed which could also be seen in Fig. 20(b). However, the modeled figure is more clean as it can be explained from the fact that the sample chosen for the measurement is not perfect and in large quantity, in reality the real distribution inside the three regions can only be predicted with certain accuracy based on the chosen sample.

Finally, in order to compare the simulated mean shadow intensity distribution to the measured, the USIR is calculated for the 36 and 360 simulated realizations of the random process and shown in Fig. 24(a) and Fig. 24(b). It can clearly be seen that the simulated USIR is very similar to the one calculated from the measured results in Fig. 20(c).

Here in this section it has been shown that a reliable model of the USI can be proposed, but the model accuracy is still based on the sample chosen for the statistical measurement in Section IV, thus the general mean and variance of the total population is not known.

VI. CONCLUSION

In this work it has been shown that a reliable stochastic user shadowing model can be constructed based on the measurement with multiple users and different gestures. The model is valid for the frequencies around 28 GHz ±6 GHz. The user shadowing model is based on the measurement with 18 subjects of different heights and gender. However, it has been shown that difference between male and female subjects

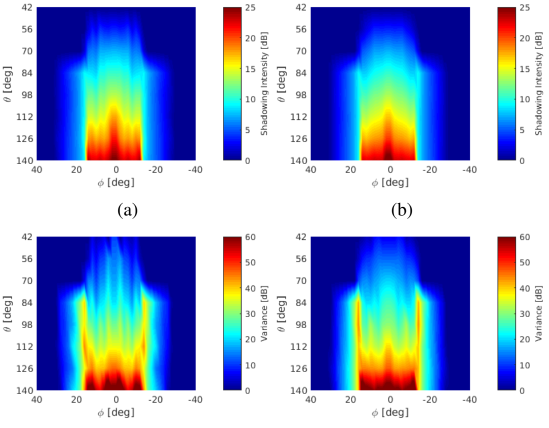

(a) (b)

(c) (d)

Fig. 23. (a) Mean USI calculated from the 36 realizations of the random process, (b) mean USI calculated from the 360 realizations of the random process, (c) variance generated from the 36 realizations of the random process, and (d) variance generated from the 360 realizations of the random process.

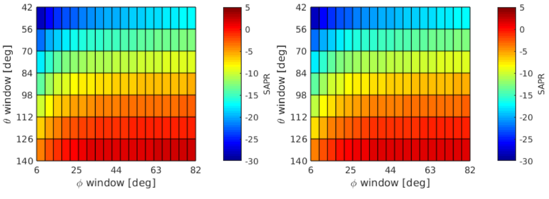

(a) (b)

Fig. 24. USIR for the mean model made from (a) 36 and (b) 360 simulated realizations of the random process.

is not significant. The 3D user shadowing pattern (USP) is modeled as a random Gaussian process within the chosen spatial regions based on the mean user shadowing pattern obtained from the measurements. Furthermore, the measured users applied the gestures which ensured the highest variation in the user blockage. The measured mean user shadowing pattern has been de-embedded from the free radiation pattern of antenna and used as a base for the model. It has been shown that de-embedding can be done with accuracy of 2 dB and do not depend on the antenna type with the same polarization. To characterize the USP two new metrics have been proposed: shadowing CDF and 3DSAPR, where SAPR is calculated both along ϕ and θ directions. Finally, it has been shown that the proposed model have similar SAPR and variance properties to the measured radiation pattern even after 360 realizations of the random process.

REFERENCES

[1] T. S. Rappaport, S. Sun, R. Mayzus, H. Zhao, Y. Azar, K. Wang, G. N. Wong, J. K. Schulz, M. Samimi, and F. Gutierrez, "Millimeter wave mobile communications for 5G cellular: It will work!," *IEEE Access*, vol. 1, pp. 335–349, 2013.

[2] J. Lee, E. Tejedor, K. Ranta-aho, H. Wang, K. T. Lee, E. Semaan, E. Mohyeldin, J. Song, C. Bergljung, and S. Jung, "Spectrum for 5G: Global status, challenges, and enabling technologies," *IEEE Comm. Mag.*, vol. 56, pp. 12–18, Mar. 2018.

[3] W. Roh, J. Y. Seol, J. Park, B. Lee, J. Lee, Y. Kim, J. Cho, K. Cheun, and F. Aryanfar, "Millimeter-wave beamforming as an enabling technology for 5G cellular communications: theoretical feasibility and prototype results," *IEEE Commun. Mag.*, vol. 52, pp. 106–113, February 2014.

[4] M. U. Rehman, X. Chen, C. G. Parini, and Z. Ying, "Evaluation of a statistical model for the characterization of multipath affecting mobile terminal GPS antennas in sub-urban areas," *IEEE Trans. Antennas Propag.*, vol. 60, pp. 1084–1094, Feb. 2012.

[5] J. Helander, K. Zhao, Z. Ying, and D. Sjöberg, "Performance analysis of millimeter-wave phased array antennas in cellular handsets," *IEEE Antenna Wireless Propag. Lett.*, vol. 15, pp. 504–507, 2016.

[6] I. Syrytsin, S. Zhang, G. F. Pedersen, and Z. Ying, "User effects on the circular polarization of 5G mobile terminal antennas," *IEEE Trans. Antennas Propag.*, vol. 66, pp. 4906–4911, Sep. 2018.

[7] I. Syrytsin, S. Zhang, G. F. Pedersen, K. Zhao, T. Bolin, and Z. Ying, "Statistical investigation of the user effects on mobile terminal antennas for 5G applications," *IEEE Trans. Antennas Propag.*, vol. 65, pp. 6596–6605, Dec 2017.

[8] T. Wang, M. Umehira, H. Otsu, S. Takeda, T. Miyajima, and K. Kagoshima, "A twin cylinder model for moving human body shadowing in 60GHz wlan," in *2015 21st Asia-Pacific Conference on Communications (APCC)*, pp. 188–192, Oct 2015.

[9] 3GPP, "Technical specification group radio access network; study on channel model for frequencies from 0.5 to 100 ghz," *document TR 38.901*, Jul. 2017.

[10] K. Zhao, J. Helander, D. Sjöberg, S. He, T. Bolin, and Z. Ying, "User body effect on phased array in user equipment for the 5G mmwave communication system," *IEEE Antenna Wireless Propag. Lett.*, vol. 16, pp. 1847–1850, 2017.

[11] B. Yu, K. Yang, C. Y. D. Sim, and G. Yang, "A novel 28 GHz beam steering array for 5G mobile device with metallic casing application," *IEEE Trans. Antennas Propag.*, vol. 66, pp. 462–466, Jan. 2018.

[12] R. Rodriguez-Cano, S. Zhang, K. Zhao, and G. F. Pedersen, "Reduction of main beam-blockage in an integrated 5g array with a metal-frame antenna," *IEEE Transactions on Antennas and Propagation*, vol. 67, pp. 3161–3170, May 2019.

[13] I. Syrytsin, S. Zhang, and G. F. Pedersen, "User impact on phased and switch diversity arrays in 5G mobile terminals," *IEEE Access*, vol. 6, pp. 1616–1623, 2018.

[14] R. Rodríguez-Cano, S. Zhang, K. Zhao, and G. F. Pedersen, "User body interaction of 5g switchable antenna system for mobile terminals at 28 ghz," in *2019 13th European Conference on Antennas and Propagation (EuCAP)*, pp. 1–4, March 2019.

[15] I. Syrytsin, S. Zhang, G. F. Pedersen, and A. S. Morris, "User-shadowing suppression for 5g mm-wave mobile terminal antennas," *IEEE Transactions on Antennas and Propagation*, vol. 67, pp. 4162–4172, June 2019.

[16] V. Raghavan, L. Akhoondzadeh-Asl, V. Podshivalov, J. Hulten, M. A. Tassoudji, O. H. Koymen, A. Sampath, and J. Li, "Statistical blockage modeling and robustness of beamforming in millimeter-wave systems," *IEEE Transactions on Microwave Theory and Techniques*, pp. 1–15, 2019.

[17] M. M. Samadi Taheri, A. Abdipour, S. Zhang, and G. F. Pedersen, "Integrated millimeter-wave wideband end-fire 5g beam steerable array and low-frequency 4g lte antenna in mobile terminals," *IEEE Transactions on Vehicular Technology*, vol. 68, pp. 4042–4046, April 2019.

[18] J. Panero and M. Zelnik, *Human Dimension and Interior Space: A Source Book of Design Reference Standards*. Watson-Guptill, 1979.

[19] M. Pelosi, O. Franek, G. F. Pedersen, and M. Knudsen, "User's impact on pifa antennas in mobile phones," in *VTC Spring 2009 - IEEE 69th Vehicular Technology Conference*, pp. 1–5, April 2009.

[20] I. Syrytsin, S. Zhang, G. F. Pedersen, and A. Morris, "Compact quad-mode planar phased array with wideband for 5G mobile terminals," *IEEE Trans. Antennas Propag.*, 2018,(in press).

ISSN (online): 2446-1628
ISBN (online): 978-87-7210-486-7

AALBORG UNIVERSITY PRESS